
Spin Dynamics of Polarised Fermi-liquid ^3He

by
Robert Andrew Nyman, MSci MA(Cantab.)

Thesis submitted to The University of Nottingham for
the degree of Doctor of Philosophy, November 20, 2003

ABSTRACT

The spin-dynamics of Fermi-liquid helium-3 in pure form and in its mixtures with helium-4 are considered in this thesis. A linearised model of the spin dynamics is developed from Leggett's equation of motion, including spin-diffusion, the Leggett-Rice spin-rotation effect and cylindrical boundary conditions. The equations are solved using a matrix formalism, allowing simulation of FIDs, NMR spectra and spin-echoes. The boundary conditions are shown to cause deviations of spin-echo amplitude and phase from the predictions of Leggett and Rice, for realistic experiments. The model is extended to include the demagnetising field (dipolar field) due to the magnetisation of the sample itself. Simulations show that, when the demagnetising field is strong, spectral clustering is present and sharp peaks are observed in the NMR spectrum.

Data from NMR experiments on ^3He and ^3He - ^4He mixtures in an 11.3T magnetic field, performed in Nottingham in 1999/2000, are analysed. The analysis of 6.2% ^3He mixture is predominantly by least-squares fitting of the model (excluding demagnetising field) to spin-echo data, yielding the transverse spin-diffusion coefficient and spin-rotation parameter as functions of temperature down to 3.4mK. Parameters are seen to deviate from the $1/T^2$ characteristic of Fermi-liquid transport parameters, with a $1/(T^2 + T_a^2)$ form, indicative of spin-transport anisotropy. The anisotropy temperature scale T_a is found to be $6 \pm 1\text{mK}$. Analysis of pure ^3He experiments is by qualitative comparison of spectroscopic data with the model (including demagnetising field): many observed features are reproduced by the simulation.

CONTENTS

Thanks	v
Glossary of Terms	vi
1 Background Physics	1
1.1 Microscopic Theory of a Fermi liquid	1
1.1.1 Fermi Gas	2
1.1.2 Fermi Liquid	4
1.1.3 Transport Coefficients	5
1.1.4 Spin Diffusion	7
1.1.5 The Leggett-Rice Spin-Rotation Effect	11
1.2 NMR	13
1.2.1 Basic Ideas	13
1.2.2 Free Induction Decays	14
1.2.3 Spin Relaxation and Diffusion	16
1.2.4 Spin Echoes	16
1.2.5 Inversion-Recovery Experiments	17
1.3 Low-Temperature NMR experiments on ^3He	19
1.3.1 Long-lived FID signals: Magnetic Modes	19
1.3.2 Leggett-Rice effect: Spin Waves	20
1.3.3 Leggett-Rice effect: Spin Echoes	21
1.3.4 Experiments in Nottingham, 1999–2000	23
1.4 Remaining Questions	24

1.4.1	Scope and Structure of the Thesis	25
2	Leggett-Rice Effect in a Finite Geometry	27
2.1	Linearised Leggett-Rice Equation of Motion	27
2.2	Matrix Representation in a Cylinder	30
2.2.1	Equation of motion in Cylindrical Coordinates	31
2.2.2	Cylindrical Basis Set and Matrix Elements	32
2.2.3	Eigenfunction or Operator Method	34
2.2.4	Testing the Computing	35
2.2.5	Some Eigenfunctions	37
2.2.6	Some Eigenvalues	37
2.3	FIDs and Spectra	38
2.3.1	Mathematical Formalism	38
2.3.2	Some FIDs	41
2.3.3	Some Spectra: Observing Eigenmodes	41
2.4	Spin-Echoes	45
2.4.1	Formalism	45
2.4.2	Results in Time and Space	47
2.4.3	Analysis of Results	51
2.4.4	Numerical Problems	56
2.5	Solution for a Sphere	57
2.5.1	Equation of Motion	57
2.5.2	Basis Set	58
2.5.3	Matrix Elements	58
2.5.4	Results	59
3	Comparing the Model to 6.2% ^3He-^4He Mixture Data	61
3.1	Background	61
3.2	Experiments	63
3.2.1	The Experimental Cell	64
3.2.2	NMR Details	66
3.3	Assumptions of the Model	68
3.3.1	Mean Free Path	68
3.3.2	Magnetic Relaxation and the Boundary Condition	69
3.3.3	Filling Channel	69
3.3.4	Demagnetising Field	70
3.3.5	Static Magnetic Field Variation	71

3.3.6	Thermal Equilibrium and Temperature Changes	71
3.4	Improvements to the Model	71
3.4.1	Finite Pulses	72
3.4.2	Non-linearities	75
3.5	Fitting NMR Data	79
3.5.1	Spectra	79
3.5.2	Spin Echoes	80
3.6	Results: D_{\perp} and μM_0 vs T	83
3.6.1	Transport parameters	83
3.6.2	Uncertainties in Results	85
3.6.3	Discussion	87
4	The Demagnetising Field and Transverse Spin-Transport	89
4.1	Equation of Motion	89
4.1.1	Demagnetising Field Due to Equilibrium Magnetisation	91
4.1.2	Demagnetising Field Due to Non-Equilibrium Magnetisation	92
4.1.3	Linearised equation of motion	93
4.1.4	Frequency Scales	93
4.1.5	Matrix Formulation	94
4.1.6	Spatial Variation of Demagnetising Field	95
4.2	FIDs	96
4.3	Spectra	97
4.3.1	Varying ω_M	97
4.3.2	Varying ω_{G_1}	98
4.3.3	Shift and Split: an interesting observation	98
4.3.4	The Demagnetising Field and Shimming	101
4.4	Eigenmodes	102
4.4.1	Damping and Shifts	102
4.4.2	Spatial Variations	104
4.5	Spin-Echoes	104
4.5.1	Violation of Orthogonality of Eigenfunctions	106
4.5.2	Echo Signals	106
4.5.3	Echo Analysis	108
5	Analysis of Pure ^3He Data, including Demagnetising Field	110
5.1	Introduction	110
5.1.1	Experimental Details	111

5.1.2	Large-Angle Data	111
5.1.3	Small-Angle Data	113
5.1.4	Comparison with the Linear Model	113
5.2	Non-equilibrium Spectra	115
5.2.1	Recovery Experiments	115
5.2.2	Low Magnetisation Spectra	116
5.2.3	Recovery Experiments: Simulation	117
5.3	Equilibrium Spectra	119
5.3.1	Varying the Temperature	119
5.3.2	Varying the Field Gradient	121
5.4	Discussion	123
6	Concluding Remarks	124
A	Properties of the Linear Equation of Motion	128
B	NMR Signal Analysis	131
C	Matrix Representation of Demagnetising Field Operators	134

Thanks

I would principally like to thank the three senior members of the Quantum Fluids group during my PhD: John Owers-Bradley (supervisor, experimental), Roger Bowley (supervisor, theoretical) and Olivier Buu (post-doc). I have also had enlightening discussions with Hikota Akimoto, Don Candela, Vladimir Dmitriev, Gírl Eska and Gerard Vermeulen.

Glossary of Terms

absorption spectrum: Part of the complex Fourier-transform of FID signal, with phase chosen so the spectrum is positive-definite.

anisotropy temperature: T_a , Temperature scale of saturation of *transverse spin-transport lifetime*. Expected to be proportional to polarisation.

broaden: To multiply a real-time FID signal by an exponential decay, before performing a Fourier transform. Equivalent to convolving a spectrum with a Lorentzian of the same half-width as the exponential decay constant.

cell: In an experiment: the volume from which NMR signals are obtained. In a simulation: the volume of interest, bounded by a surface with boundary conditions as in Eqn. (2.9).

complex symmetry: The property of an operator or matrix as defined in Eqn. (A.7). The matrix is equal to its own transpose. In contrast to Hermiticity, which is common in the mathematics of quantum mechanics.

dead-time: Time at the beginning of an NMR experiment when ringing of transmitted pulses dominates received signal, rather than the induction signal from magnetised sample. See Appendix B.

demagnetising field: Also known as the dipolar field. The magnetic field due to the magnetisation of the sample itself.

effective spin-diffusion coefficient: A complex number representing both spin-diffusion and spin-rotation, for transverse components of magnetisation, defined by $D_{\text{eff}} = D_{\perp}/(1 + i\mu M_0)$.

eigenfrequency: The scalar part of the solution of Eqn. (2.30), in real time (see Eqn. (2.15))

eigenfunction: The function part of solution of Eqn. (2.30)

eigenfunction method: Calculating the evolution of the magnetisation density as sum over the *eigenmodes* of the relevant *pseudo-hamiltonian*.

eigenmode: The complete solution to Eqn. (2.30), scalar and function parts combined. The eigenvalues and eigenfunctions are properties of the real, physical quantity, the eigenmode.

eigenvalue: The scalar part of the solution of Eqn. (2.30)

eigenvector: See *eigenfunction*

elementary excitations: The simplest excitations of a quantum fluid. When the elementary excitations are near the Fermi surface (of a Fermi fluid), they are called *quasiparticles*.

filling channel: Link between *cell* and *reservoir* in experiment, allowing fluid to

flow, maintaining thermal contact, but effectively isolating the two chambers during an NMR experiment.

least-squares fitting: Method of comparing a model to data, varying parameters of the model to minimise the sum-of-squares of the differences between the model and the data.

Leggett-Rice effect: Precession of the magnetisation around the spin-current. Also known as the *spin-rotation effect*.

longitudinal spin-diffusion: Motion (in any spatial direction) of components of magnetisation which are parallel to the equilibrium direction of magnetisation.

magneto-dynamic mode: An eigenmode of the equation of motion (Eqn. (4.20)) which includes spin-transport and the demagnetising field. Corresponds to a peak in a spectrum where Leggett-Rice and demagnetising field effects are not separable.

operator exponentiation: Mathematically, finding the exponential of a operator represented by a matrix, using a power series. Can be applied to solving the linear equation of motion for transverse-magnetisation density in a Fermi liquid, Eqn. (2.8).

overlap matrix: The matrix whose elements are the integrals of the eigenfunctions before and after the π -pulse, defined by Eqn. (2.49b).

π -pulse: A pulse which rotates the magnetisation by 180° : the second pulse in a spin-echo experiment. Also can be the initial pulse in a recovery experiment.

point-and-shoot: A method for solving linear ordinary differential equations by finite differencing. Start from one boundary, iterate forwards to the other boundary. See section 2.2.4.

pseudo-hamiltonian: An operator or matrix representing the linearised-equation of motion Eqn. (2.8) or Eqn. (4.20). Does not represent an energy, but its eigenvalues correspond to exponential time-variation. See also Appendix A.

quasiparticle: An *elementary excitation* near to a Fermi surface.

recovery experiment: The magnetisation is first tipped through a large angle (usually 90° or 180°), then the longitudinal magnetisation is allowed to relax. At suitable intervals, small-angle FID experiments are performed, so allowing behaviour to be studied for magnetisation lower than equilibrium value. Also known as an inversion-recovery experiment.

reservoir: Large volume of helium mixture connected to the *cell* by a *filling channel*; contains thermometers, and acts as a thermal contact to the fridge via a heat exchanger.

spectral clustering: An effect due to the *demagnetising field*, where the inhomoge-

neous broadening component of the spectrum is replaced by one or more sharp peaks when the demagnetising field is strong.

spin-diffusion coefficient: Diffusive coefficient in equation of motion for magnetisation.

spin-rotation effect: See *Leggett-Rice effect*

spin-wave mode: Discrete solution of the equations of motion, satisfying the boundary condition. Appear in the NMR spectrum as a clear peak. Almost synonymous with an *eigenmode*.

tipping angle: The angle through which the magnetisation is rotated in a *tipping pulse*. In this thesis, takes the mathematical symbol θ .

tipping pulse: A pulse which excites magnetisation transverse to the equilibrium direction: the only pulse is an FID experiment, the first pulse in a spin-echo experiment.

transverse spin-diffusion: Motion (in any spatial direction) of components of magnetisation which are perpendicular to the equilibrium direction of magnetisation.

transverse spin-transport lifetime: τ_{\perp} . Time between collisions of *elementary excitations* which carry magnetisation transverse to the applied magnetic field. expected to have functional form $C/(T^2 + T_a^2)$.

vibrating-wire: A loop of wire, with an electromechanical resonance, allowing measurement of viscosity of a fluid. Implicitly a sensitive thermometer for pure ^3He and ^3He - ^4He mixtures

CHAPTER 1

BACKGROUND PHYSICS

Helium has two stable isotopes: ^4He has two protons, two neutrons and two electrons, making it a composite spin-0 boson; ^3He has just a single neutron, and so is a spin- $\frac{1}{2}$ fermion. One neutron causes a profound difference in the behaviour at low temperature, where quantum statistics are important.

Helium-4 forms a superfluid Bose-Einstein condensate (macroscopic occupation of the quantum-mechanical ground state) below 2K, with no viscous resistance to flow and an enormous thermal conductivity. In contrast, helium-3 becomes a Fermi-liquid below about 1K, with viscosity increasing as temperature decreases, due to the Pauli exclusion principle. If a few percent of ^3He is dissolved in superfluid ^4He (up to 6.4% solution is possible at saturated vapour pressure), the ^4He acts as a background, leaving the ^3He to act almost as if it were less a dense fluid, with each atom having a larger effective mass. It is the macroscopic-scale quantum effects of these systems that are of interest to the scientific community.

1.1 Microscopic Theory of a Fermi liquid

When the temperature is very low, atoms try to occupy the states with the lowest energy available. For a system of fermions (obeying the Pauli exclusion principle), this condition means just one atom in each state of momentum, spin, etc. Even at zero temperature, atoms have finite energy and momentum.

1.1.1 Fermi Gas

The result of applying the Paul exclusion principle to a non-interacting, dilute gas of particles is Fermi-Dirac statistics (see for example Dobbs[1], p17–21, or Bowley and Sanchez[2], p213). In such a system of fermions, the distribution function of the number of fermions n_i in each energy state E_i of degeneracy g_i is:

$$n_i/g_i = \frac{1}{e^{(E_i-\mu)/k_B T} + 1} \quad (1.1)$$

where $\mu(T)$ is the chemical potential which conserves the number of fermions ($N = \sum_i n_i$). The consequence is that, at zero temperature, all the states up to an energy $E_F = k_B T_F$ are occupied, all those above E_F are unoccupied; E_F is known as the Fermi energy, T_F the Fermi temperature. At finite temperature some states above E_F are filled, some below are empty: see Fig. 1.1.

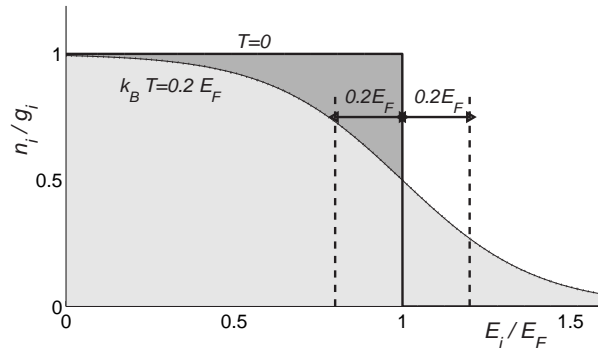


Figure 1.1: Fermi-Dirac distribution function: shaded regions are occupied. The curved line is at temperature $k_B T = 0.2 E_F$.

The Fermi energy depends on the density of states D as a function of energy, and energy depends on momentum p . The density of states in three-dimensions, for states in a range p to $p + dp$ is:

$$D(p) = \frac{dN(p)}{dp} = 2 \times \left(\frac{4\pi V}{h^3}\right) p^2 \quad (1.2)$$

where the factor of two accounts for degeneracy of a spin- $\frac{1}{2}$ particle, V is the volume and h is the Planck constant. Integrating at zero temperature to give the correct number of particles produces the Fermi temperature, Fermi momentum and the density of states at the Fermi surface. The Fermi surface is the locus of the discontinuity of the distribution function Eqn. (1.1) in momentum space at absolute zero; the surface dividing occupied states from unoccupied states. For reasons of symmetry, the Fermi surface of ^3He is a sphere, which has radius $p_F = \hbar(3\pi^2 N/V)^{1/3}$.

The number of particles per unit energy can be found by substituting the energy $E = p^2/2m$ into the density of states Eqn. (1.2) and multiplying by the distribution function Eqn. (1.1):

$$\frac{dN(E)}{dE} = \left(\frac{n_i}{g_i}\right) \times D(E) = \frac{V}{2\pi^2} \left(\frac{2m}{\hbar^2}\right)^{3/2} \frac{E^{1/2}}{e^{(E_i-\mu)/k_B T} + 1} \quad (1.3)$$

At zero temperature the number of particles goes as $E^{1/2}$ up to the Fermi energy, then zero for greater energy.

From the number of particles per unit energy, equilibrium thermodynamic quantities can be derived, such as specific heat capacity C . For instance, at a small, finite temperature T , about $k_B T D(E_F)$ particles are excited near the Fermi surface, by an energy about $k_B T$. Therefore the thermal energy is $U = D(E_F) k_B^2 T^2$, and the heat capacity is $C = \partial U / \partial T = 2 D(E_F) k_B^2 T$: the heat capacity of a Fermi gas is proportional to temperature.

Polarised Fermi Gas

Another derivable, equilibrium quantity is magnetic susceptibility χ . In a Fermi gas, Pauli paramagnetism is a consequence of the exclusion principle combined with the change in energy of a spin in a magnetic field: for a spin-half particle of magnetic moment μ in a field B , the energy is $\pm\mu B$. The number of spins parallel to the field increases, the number anti-parallel decreases, as illustrated in Fig. 1.2. The

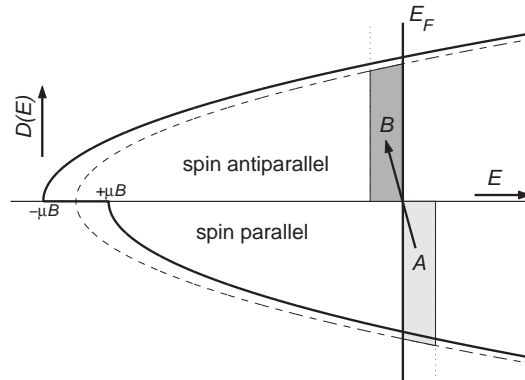


Figure 1.2: Pauli Paramagnetism at zero temperature: the number of particles per unit energy goes as $(E \pm \mu B)^{1/2}$, a shift along the energy-axis. To minimise energy, the particles in box A have transferred to box B; the boxes are of width μB .

number of particles per unit energy is proportional to $(E \pm \mu B)^{1/2}$; the numbers of particles in the parallel and antiparallel states adjust to equalise the Fermi energies (minimising total energy, maximising entropy). The parallel-spin particles in box A

have transferred to box B and now have antiparallel-spin; the number of these particles is about $D(E_F) \times \mu B$. The magnetisation M is the difference in populations of parallel and antiparallel spins (the number transferred) times the magnetic moment μ of each spin:

$$M = \mu^2 B D(E_F) \implies \chi = \frac{M}{H} = \mu_0 \mu^2 D(E_F) \quad (1.4)$$

The susceptibility χ is independent of temperature if $T \ll T_F$, and the polarisation is small ($\mu B \ll E_F$). While the Fermi energies for parallel and antiparallel spins are equal, the momenta are different, since $p_F = \sqrt{2m^*(E_F \pm \mu B)}$ (where m^* is the effective mass, see below), which depends on the sign of the spin energy.

1.1.2 Fermi Liquid

The treatment of an interacting system of fermions (Fermi liquid) is more complicated than that of a non-interacting system (Fermi gas): the theory is known as Landau Fermi-liquid theory[3]. The extensions Landau made to the theory were that the simplest excitations of the system are not simple particles but *quasiparticles* which are like particles with properties altered by the presence of other particles; and that there is an effective interaction between the quasiparticles (Ref. [1], p38). Importantly, a Fermi surface is present in the liquid as well as the gas. There is assumed to be a one-to-one correspondence between eigenstates of the gas and the liquid, as if the interactions has been turned on adiabatically, and eigenstates changed smoothly (see Landau[3] or Pines and Nozières[4], p11 or Baym and Pethick[5], p3).

Quasiparticles are the *elementary excitations* of the system. They have definite momentum, energy and spin just like real particles, but have a different mass (the effective mass m^*) due to the interactions of one particle with those around it. Quasiparticles have energy and momenta outside the Fermi surface, and their creation is accompanied by the creation of a quasihole (an empty state inside the Fermi surface).

The effective interaction between quasiparticles comes about because the energy of a quasiparticle is dependent on the configuration of all the other quasiparticles. A quasiparticle is considered to be a small perturbation to the equilibrium state[†] (near to the Fermi surface), and interacts only with other states close to the Fermi surface. Since only quasiparticles of similar energy and momentum (say \mathbf{p} and \mathbf{p}') interact, the interaction depends on the angle between the momenta. The interaction energy

[†]Landau Fermi-liquid theory assumes a linear response, so only elementary excitations with momenta near the Fermi surface are considered.

$f(\mathbf{p}, \mathbf{p}')$ can be characterised by a sum over Legendre polynomials $P_l(\cos \theta)$ (where θ is the angle between \mathbf{p} and \mathbf{p}'), weighted by coefficients:

$$f(\mathbf{p}, \mathbf{p}') = \sum_l F_l^s P_l(\cos \theta) \quad (1.5)$$

Landau[6][7] introduced a similar notation. A further spin-dependent interaction is present, dependent on the inner product of the spins of the quasiparticles (as well as the momenta); the coefficients F_l^a are used. F_l^s and F_l^a are the spin-symmetric and -antisymmetric Landau parameters.

From the Landau parameters and the Fermi-distribution function, the equilibrium and transport properties can be calculated. For example, the effective mass (derived by imposing Galilean relativity on the fluid) depends on the second spin-symmetric parameter: $m^*/m = 1 + \frac{1}{3}F_1^s$ (Dobbs[1], p42). The magnetic susceptibility depends on the first anti-symmetric parameter as well as the mass: $\chi = \chi_g(m^*/m)(1 + F_0^a)^{-1}$ (Ref. [1], p45) where χ_g is the susceptibility of a Fermi gas, Eqn. (1.4).

1.1.3 Transport Coefficients

Transport in the classical kinetic theory of a gas is thought of as particles carrying a non-equilibrium physical quantity (such as excess kinetic energy or momentum or magnetism) over a distance equal to the mean free path, before scattering and reaching the local equilibrium. The transport properties are proportional to the mean free path, as well as the amount of the property carried by each particle. The mean free path in turn depends inversely on the probability of scattering (or the scattering cross-section). The transport properties generally increase with root mean-square velocity $\langle v^2 \rangle^{1/2} \propto T^{1/2}$.

It is well known that in a Fermi fluid, well below T_F , the mean free path varies as $1/T^2$ [†]. The rate of scattering of elementary excitations is proportional to both the strength of interactions (the scattering cross-section), and the number of excitations available to scatter, and the number of other states available for the excitations to scatter into. Both the number of excitations (quasiparticles) and the number of empty states (quasiholes) are proportional to the temperature; therefore the scattering rate is proportional to the square of temperature (see Landau[3]), and so the mean free path varies inversely with the square of temperature. The inverse of the

[†]In common with other well known phenomena, it is difficult to find a clear, concise, precise, mathematical argument explaining the temperature variation of a Fermi fluid. What follows is a hand-waving description of the physical arguments used in a full derivation of a transport coefficient.

scattering rate is approximately the lifetime of non-equilibrium phenomena, the time to reach local thermal equilibrium.

Thus, in a Fermi gas below the Fermi temperature, the transport properties should have temperature dependence associated with the $1/T^2$ mean free path: viscosity $\eta T^2 = \text{constant}$; diffusion $DT^2 = \text{constant}$; thermal conductivity $\kappa T = \text{constant}$ (there is a factor T for heat capacity, see page 3). In general, there may be a different lifetime (and mean free path) for each transport process.

In a Fermi liquid, the derivation of transport properties is very involved. The number of particles per unit momentum is allowed to be a slowly varying function of space and time[†], and the conservation laws of number, momentum and energy are applied. The transport coefficients can only be calculated by considering the details of the interactions of particles, through either a model of the effective interaction (involving calculation of the collision integral) or substituting values of the Landau parameters. Full calculations of transport parameters sometimes yield deviations from the Fermi-gas $1/T^2$ laws (see for instance Baym and Pethick[5] or Lhuillier and Laloë [8, 9]). The results are often in broad agreement with experiments, although there are some deviations: for example Abel *et al*[10] measured thermal conductivity; Carless *et al*[11] measured viscosity in pure ^3He , König and Pobell measured viscosity in ^3He - ^4He mixtures: see Fig. 1.3.

Spin-polarised Fermi fluids are even more complicated. Typically, the interactions between two populations parallel and anti-parallel to the applied magnetic field are considered. The rate of collisions can be increased or decreased, depending on the details of the property being transported. For example, viscosity can be enhanced by polarisation, as measured by Owers-Bradley *et al*[15]: some collisions are excluded by identical particle symmetries. Spin diffusion is treated in more detail below.

A further complication lies in the idea of collective modes, some of which are adiabatic distortions of the Fermi surface. No quasiparticles are excited, but the energy and momenta of the eigenstates vary. The phenomenon of zero sound is one of the collective modes.

[†]The Heisenberg Uncertainty principle means that a function of momentum is only a sensible concept if the spatial variation is much smaller than the equivalent required resolution in momentum space. The uncertainty principle means that Landau Fermi-liquid theory may only be applied to macroscopic quantities.

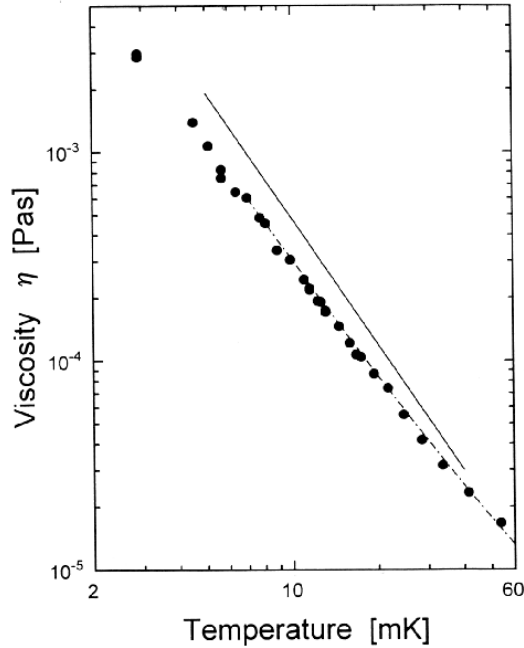


Figure 1.3: Viscosity of 6.8% ${}^3\text{He}$ - ${}^4\text{He}$ mixture, Fermi liquid $1/T^2$ behaviour: taken from König and Pobell[12], Fig. 9. Circles are results of König and Pobell, dash-dotted line is from Zeegers *et al*[13], solid line is from Bradley and Oswald[14]. The viscosity is proportional to the transport lifetime, which goes as $1/T^2$ in a Fermi liquid.

1.1.4 Spin Diffusion

Spin transport (or transport of magnetisation density) is unique among transport properties: spin-transport occurs only when a magnetic field is applied to the sample, and the field makes the dynamics anisotropic. Motion of magnetisation is detected by NMR (see section 1.2). Spin transport occurs when the magnetisation varies with position; the gradient of magnetisation can be split into two parts, gradients of magnitude and gradients of direction:

$$\nabla \mathbf{M} = \nabla(M\hat{\mathbf{e}}) = \hat{\mathbf{e}}\nabla M + M\nabla\hat{\mathbf{e}} \quad (1.6)$$

where M is the magnitude and $\hat{\mathbf{e}}$ the direction of magnetisation. A gradient of magnitude corresponds to *longitudinal spin-diffusion*, and a gradient of direction corresponds to *transverse spin-diffusion* (see Fig. 1.4).

Both spin current \mathbf{J} and diffusion coefficient are mathematically described by tensors of rank two. The applied magnetic field gives a symmetry axis; the tensors

reduce to two vector components parallel and perpendicular to the field:

$$\mathbf{J} = \mathbf{J}_{\parallel} + \mathbf{J}_{\perp} \quad (1.7)$$

$$\mathbf{J}_{\parallel} = -D_{\parallel} \hat{\mathbf{e}} \nabla M \quad (1.8)$$

$$\mathbf{J}_{\perp} = -D_{\perp} M \nabla \hat{\mathbf{e}} \quad (1.9)$$

We shall see later that the transverse term of Eqn. (1.9) is modified for Fermi fluids by the presence of the Leggett-Rice spin-rotation effect (section 1.1.5).

Conservation of magnetisation in the presence of diffusion, leads to:

$$\frac{\partial \mathbf{M}}{\partial t} = -\nabla \cdot \mathbf{J} \quad (1.10)$$

The above equation neglects Larmor precession (see section 1.2.3) and spin-rotation. The microscopic picture of spin transport is always anisotropic, but the macroscopic results may be isotropic: D_{\parallel} may be equal to D_{\perp} . A good explanation of spin transport anisotropy was published by Mullin and Jeon[16]; see Fig. 1.4.

When the diffusion is isotropic ($D_{\parallel} = D_{\perp} = D_0$), the equation reduces to simple diffusion of each component of magnetisation:

$$\frac{\partial \mathbf{M}}{\partial t} = D_0 \nabla^2 \mathbf{M} \quad (1.11)$$

The spin-diffusion coefficient should be the same as the diffusion coefficient for self-diffusion of atoms[17], given by $D_0 = \frac{1}{3} v_F^2 (1 + F_0^a) \tau_D$, where τ_D is the excitation lifetime associated with diffusion. Therefore the diffusion coefficient should be proportional to T^{-2} , as was first measured by Anderson *et al*[18].

Theoretical study of a polarised Fermi-liquid is considerably more complicated than study of either a polarised Fermi-gas or an unpolarised Fermi-liquid. The most important consideration is that the populations with spin parallel and antiparallel to the field have the same Fermi energy but different Fermi momenta. Therefore the Fermi surfaces are concentric spheres of different radii in momentum space.

Longitudinal Spin-Diffusion

When the magnetisation (polarisation) is everywhere parallel to the applied field, but the magnetisation is of variable magnitude, longitudinal spin-diffusion occurs (see Fig. 1.4). Quasiparticles (from position x) carry polarisation, to a position where they are out of equilibrium ($x + dx$), where the Fermi surfaces are of slightly different size, i.e. the polarisation is different. Here they can scatter (satisfying the conservation laws), reaching local equilibrium, having moved magnetisation; quasiparticle motion is the microscopic cause of spin current.

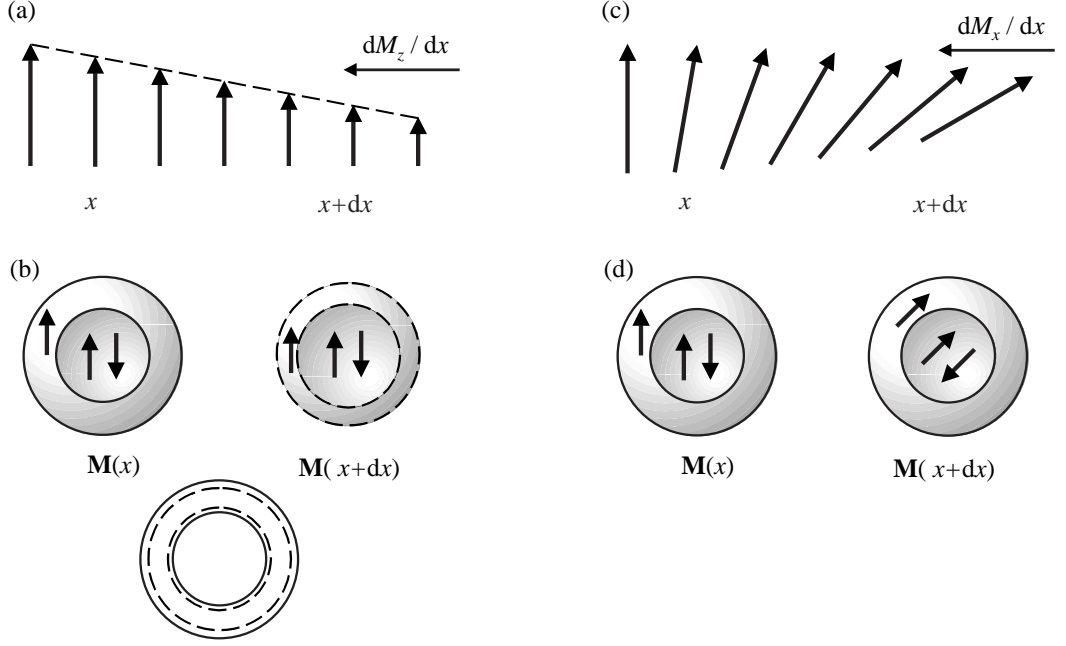


Figure 1.4: *Longitudinal Spin-Diffusion:* (a)The length of the vector magnetisation (polarisation) is changing so longitudinal-spin current $\mathbf{J}_z \propto \nabla M_z$ is in the x -direction. (b)The smaller Fermi sphere is populated parallel and antiparallel to the applied field, but between the Fermi spheres only spin-parallel states are occupied; therefore net polarisation comes from the shell between the Fermi surfaces. Longitudinal-spin transport originates in differences of the sizes of Fermi spheres; non-equilibrium polarisation (quasiparticles) scatters near the Fermi surfaces (see superimposed Fermi surfaces).

Transverse Spin-Diffusion: (c)Direction of polarisation changes, so spin-current $\mathbf{J}_x \propto \nabla M_x$ is in the x -direction. (d)Direction of quantisation changes (parallel/antiparallel are taken with respect to magnetisation not applied field), but Fermi spheres do not change size. Therefore, all spins between Fermi surfaces must scatter for quasiparticles to equilibrate. After Mullin[16], Fig.1 and Fig.2.

The key point is that the scattering occurs between excitations with momenta near Fermi surfaces. At finite temperature, the Fermi surfaces are blurred by the presence of excitations (quasiparticles and quasiholes). The scattering rate depends on the local number of excitations, which in turn depends on the temperature; the lifetime for longitudinal spin-carrying quasiparticles in a Fermi gas τ_{\parallel} inversely proportional to temperature-squared[19]:

$$\tau_{\parallel} \propto \frac{1}{T^2} \quad D_{\parallel} = \tau_{\parallel} \times \frac{(n^+ + n^-)}{n^+ \langle v^{-2} \rangle^+ + n^- \langle v^{-2} \rangle^-} \quad (1.12)$$

where n^+ is the number density of spin-parallel quasiparticles, n^- is the number density spin-antiparallel; $\langle v^{-2} \rangle^{\pm}$ the mean inverse-square velocity of parallel/antiparallel quasiparticles. The longitudinal spin-diffusion coefficient depends

on the polarisation.

Transverse Spin-Diffusion

Transverse spin-diffusion (motion of components of magnetisation perpendicular to the applied magnetic field) occurs when the direction of the magnetisation changes from its equilibrium direction. The polarisation is to be considered with respect to an axis not parallel to the applied magnetic field, but instead parallel to the local direction of magnetisation. The polarisation is the total of the contribution due to the states inside the smaller of the two Fermi surfaces (doubly occupied, zero total contribution) and the states between the Fermi surfaces (singly occupied). When the total polarisation changes, the doubly occupied states are largely irrelevant, but the direction of the singly occupied states is crucial.

If a transverse-spin-carrying excitation moves to a position where it is out of equilibrium, then it can scatter (satisfying conservation laws) from the states between the Fermi surfaces[†], which have a non-zero net polarisation. The polarisation dependent scattering rate is proportional to the square of the space between the Fermi surfaces, i.e. proportional to the square of the polarisation.

The thermally excited states are also available for scattering to and from, so the total scattering rate is a sum of the two contributions (temperature dependent and polarisation dependent). The inverse of the *transverse spin excitation lifetime* is:

$$\tau_{\perp}^{-1} = \tau_{\perp 0}^{-1}(M) + \tau_{\perp T}^{-1}(T) \quad (1.13)$$

$$\text{where:} \quad \tau_{\perp 0}^{-1}(M) \propto M^2 \quad \tau_{\perp T}^{-1}(T) = \tau_{\parallel}^{-1} \propto T^2$$

The resulting transverse spin excitation lifetime, and the accompanying spin-diffusion coefficient therefore do not diverge as the temperature approaches absolute zero, but saturate at a finite value depending on the polarisation. The functional form is usually written as:

$$\tau_{\perp} = \frac{\tau_{\perp 0} T_a^2}{T^2 + T_a^2} \quad D_{\perp} = \frac{D_{\perp 0} T_a^2}{T^2 + T_a^2} \quad (1.14)$$

where $T_a \propto M$ [20] (M is the magnetisation, proportional to the polarisation) is known as the *anisotropy temperature* and is proportional to the magnitude of the equilibrium magnetisation. For example, in a dilute Fermi gas, if the polarisation is 0.1%, equivalent to a magnetic field a little less than one tesla, then $T_a \sim 1\text{mK}$ [21].

[†]States far from the Fermi surfaces are strictly not quasiparticles: quasiparticles correspond to small perturbations. A more proper name is elementary excitations.

The anisotropy temperature takes its name from the fact that while at high temperature the longitudinal and transverse lifetime are predicted to be equal, at low temperatures they are predicted to diverge. The consequence is unusual: transverse spin-diffusion is a loss-mechanism (associated with increasing disorder) which does not vanish as the temperature approaches absolute zero.

Calculations of τ_{\perp} , D_{\perp} and T_a from first-principles are highly involved (e.g. Refs. [19][21] and [22]), and require approximations, for example solving in the limit of low polarisation, or assuming a specific interaction potential, or taking only low energy collisions (s-wave approximation). The spin-transport coefficients (both longitudinal and transverse) depend on the polarisation as well as the lifetime. Extension of the theory to Fermi liquids (not in the extreme dilute limit) was calculated by Meyerovich and Musaelian, first at zero temperature[23], then at finite temperature [20]. The expected temperature variation of D_{\perp} is as above, saturating below the anisotropy temperature.

A Dissenting Voice

More recently, Fomin[24] has suggested another possibility: at zero temperature, the excitations move always at local equilibrium (adiabatically), so scattering is not required for spin-transport processes, and spin transport is undamped. Contrast this view with the conventional view of excitations moving out of equilibrium, then scattering, which leads to finite damping even at absolute zero.

However, Fomin's calculations have not been extended to finite temperature. It is possible damping does not diverge as the temperature decreases, so at all finite temperatures Eqn. (1.14) remains valid. The finite temperature implications of Fomin's work are not yet well developed and it is not clear how to distinguish, experimentally at finite temperature, between the adiabatic and non-adiabatic (more conventional) microscopic theories.

In addition, Meyerovich and Musaelian have argued that Leggett's hydrodynamic equations may break down at high polarisation in concentrated solutions, because states between Fermi surfaces are not well-defined, long-lived quasiparticle excitations. Perhaps, depending on how Fomin's theory is interpreted, whatever carries magnetisation may not even be an excitation, and it may not have a finite lifetime.

1.1.5 The Leggett-Rice Spin-Rotation Effect

Spin-diffusion is not the only possible spin-transport mechanism: in a Fermi fluid, there is also the *spin-rotation* effect, sometimes known as the Leggett-Rice effect,

predicted by Leggett and Rice[25][26]. To quote Leggett[26]:

...in a strongly interacting Fermi liquid any polarization of the spins will give rise to a *molecular field*, and any given spin will then see (and precess around) a total local field which is the sum of the molecular field and the external one. Clearly this molecular field cannot affect the precession of the total spin density $\mathbf{M}(\mathbf{r}, t)$, since it is automatically parallel to it; however it *can* cause additional precession of the *spin current*...

The longitudinal-spin current is unaffected by the molecular field, but the equation of motion for transverse-spin current Eqn. (1.9) is incremented by the precession of spin-current around the local magnetisation density:

$$\mathbf{J}_\perp = -D_\perp M \nabla \hat{\mathbf{e}} - \mathbf{J}_\perp \times \mu M \hat{\mathbf{e}} \quad (1.15)$$

where μ represents the strength of the molecular field, and μM is called the *spin-rotation parameter*. The value of the spin-rotation parameter depends on the interactions between elementary excitations.

The spin-rotation effect is negligible unless the precession frequency due to the molecular field $\gamma \mu M$ (γ is the gyromagnetic ratio) is at least comparable to the inverse excitation lifetime τ_\perp^{-1} . Also, gradients of magnetisation must be present which are perpendicular to the magnetisation density itself. If:

$$\mu M_0 = \lambda \Omega_0 \tau_\perp \gtrsim 1 \quad \text{where} \quad \lambda = \frac{1}{1 + F_0^a} - \frac{1}{1 + \frac{1}{3} F_1^a} \quad (1.16)$$

then spin-rotation can occur. Here $\Omega_0 = \gamma B_0$ is the Larmor frequency (B_0 is the applied magnetic field), and μM_0 is the spin-rotation parameter corresponding to the static magnetisation. λ , and therefore μM_0 , depends on the pressure and concentration through the Landau parameters. For certain conditions, λ can be zero, so there is no spin-rotation: at saturated vapour pressure, 3.8% ${}^3\text{He}$ - ${}^4\text{He}$ mixture shows no spin-rotation effect[27][28]. The derivation of the full equation of motion draws heavily on the work of Silin[29], and starts from a kinetic equation for quasiparticle spins. An important prediction is that the spin-rotation parameter is proportional to the transverse-spin excitation lifetime τ_\perp , the same lifetime that is used to calculate the transverse spin-diffusion coefficient. Therefore μM_0 and D_\perp should have the same temperature variation.

Excluding Larmor precession (see below), the final equation of motion for magnetisation derived by Leggett[26] is:

$$\begin{aligned} & \frac{\partial \mathbf{M}(\mathbf{r}, t)}{\partial t} \\ &= D_0 \sum_{i=1}^3 \frac{\partial}{\partial x_i} \left[\frac{1}{1 + \mu^2 M_0^2} \left\{ \frac{\partial \mathbf{M}}{\partial x_i} + \mu \left(\mathbf{M} \times \frac{\partial \mathbf{M}}{\partial x_i} \right) + \mu^2 \left(\mathbf{M} \cdot \frac{\partial \mathbf{M}}{\partial x_i} \right) \mathbf{M} \right\} \right] \end{aligned} \quad (1.17)$$

where x_i denotes one of the three cartesian co-ordinates. Because the interactions and the molecular field are local, the equation is local, i.e. all the positions and times in the equation have a single value (a hydrodynamic equation). The equation is non-linear, having terms up to third order in magnetisation. In addition to the diffusive term (first term on the right-hand side of Eqn. (1.17)) there is a reactive term (second term) which causes weakly damped spin-waves if μM_0 is greater than unity. The observable consequences of the equation of motion will be explained in section 1.3.3.

1.2 NMR

Nuclear Magnetic Resonance is one of the most widely applied of all techniques in modern physics. It is the technique of choice for studying nuclear spin dynamics (the only real alternative being neutron scattering). There are many good books explaining NMR, e.g. Goldman[30], or Abragam[31]. In this section, some of the basics of NMR are explained, and then applied to spin transport.

1.2.1 Basic Ideas

The most fundamental idea of NMR is Larmor precession. Many nuclei have nuclear spin angular momentum $\hbar \mathbf{I}$, with a parallel magnetic dipole $\mathbf{m} = \gamma \hbar \mathbf{I}$. A magnetic dipole in a magnetic field \mathbf{B}_0 experiences a torque perpendicular to the dipole $\mathbf{G} = \mathbf{m} \times \mathbf{B}_0$; torque is rate of change of angular momentum: $\frac{d\hbar \mathbf{I}}{dt} = \mathbf{G}$. Therefore the rate of change of magnetic dipole[†] is:

$$\frac{d\mathbf{m}}{dt} = \gamma \mathbf{m} \times \mathbf{B}_0 = \mathbf{m} \times \boldsymbol{\Omega}_0 \quad (1.18)$$

The process is known as Larmor precession, and occurs at a frequency $\Omega_0 = \gamma B_0$, the Larmor frequency. The quantity γ is known as the gyromagnetic ratio, and is

[†]Of course the angular momentum is quantised, implying that the magnetic dipole moment is also quantised. The quantum mechanical picture requires calculation of the time-dependent expectation value of the angular momentum. Since the three Cartesian components of angular momentum operator do not commute, there is always precession if a magnetic field is applied (the component of angular momentum along the field is known).

different for different nuclei: for ${}^3\text{He}$, $2\pi\gamma = -32.4 \text{ MHz T}^{-1}$ (${}^4\text{He}$ has no nuclear spin, so does not undergo Larmor precession). Typical NMR experiments place the Larmor frequency in the radio-frequency (RF) range, 100kHz to 1000MHz.

A bulk sample can be described as an average over many single, independent spins, each behaving as above. The resulting magnetisation density \mathbf{M} obeys the same equation of precession as a single dipole \mathbf{m} , Eqn. (1.18). There is a static (non-precessing) solution to the precession equation, which has the magnetisation along the magnetic field direction: the equilibrium magnetisation.

Subsequent derivations are easier if we make use of the frame of reference S' , rotating about the z axis (the rotating frame has Cartesian co-ordinates x', y' and z): we subtract the Larmor precession $\gamma\mathbf{M} \times \mathbf{B}_0$.

1.2.2 Free Induction Decays

If an RF electromagnetic pulse in the xy -plane rotating at the Larmor frequency is applied to a sample, then in the rotating frame it looks like a static magnetic field; the magnetisation will precess around the RF field (see Fig. 1.5). If the initial

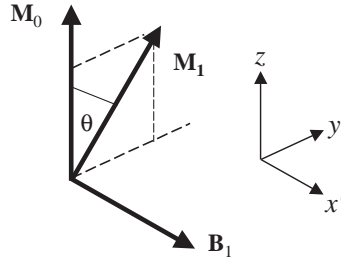


Figure 1.5: Larmor Precession and RF-Pulses: In the rotating frame, an RF-pulse acts like a magnetic field in the x' -direction, causing precession of the magnetisation away from equilibrium \mathbf{M}_0 into the $y'z$ -plane by an angle $\theta = \gamma B_1 t_{\text{pls}}$. \mathbf{M}_1 is the magnetisation after the pulse.

magnetisation is $M_0\hat{\mathbf{z}}$, the field in the rotating frame is $B_1\hat{\mathbf{x}}'$, and the pulse lasts time t_{pls} , then the magnetisation in the rotating frame immediately after the pulse will be $\mathbf{M}_1 = M_0(\hat{\mathbf{y}}' \sin \gamma B_1 t_{\text{pls}} + \hat{\mathbf{z}} \cos \gamma B_1 t_{\text{pls}})$. Some magnetisation along the field has been tipped into the xy -plane (the plane where precession occurs), in the y' direction[‡]. The angle $\theta = \gamma B_1 t_{\text{pls}}$ is known as the *tipping angle*.

Larmor precession can be observed through electromagnetic induction: the magnetisation generates a magnetic field, which rotates at the Larmor frequency; a time-varying magnetic field generates an electric field; the electric field can be detected

[‡]Magnetisation can also be tipped into the xy -plane by a continuous wave (CW) technique, which is not discussed here.

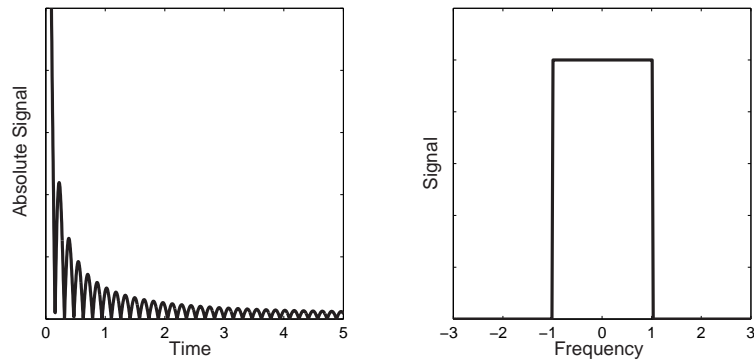


Figure 1.6: Free Induction Decay: Left panel shows the magnitude of the observed signal as a function of time, when a gradient G is present, for a sample extending from $-L$ to $+L$. Right panel shows the spectrum obtained by Fourier transform. Time (or frequency) in units of $1/\gamma GL$ (or γGL). Frequency is taken relative to Larmor frequency at centre of co-ordinates.

using a suitable antenna and electric circuit with a resonance near the Larmor frequency. Often the same antenna and circuit are used for transmission of RF-pulses as well as detection of induction signals. Only if there is magnetisation in the xy -plane (i.e if an RF-field has been applied) is any signal observed. The signal observed is proportional to the precession frequency (through the time derivative), and the integral of the magnetisation over the volume of sample as viewed by the antenna.

When the static magnetic field B_0 varies with position, the precession rates also vary with position, so there will be phase differences in the precession, increasing with time. Viewed in the rotating frame, the direction of magnetisation depends on position, so the integral of magnetisation over the sample will decrease. The signal will decay (see Fig. 1.6), so an experiment involving a single pulse is called a Free Induction Decay (FID).

A Fourier transform of the FID signal shows the frequency variation due to magnetic field inhomogeneity. For example: a field gradient $\partial B_0/\partial z = G$ is present along the direction of the field; the sample extends from $z = -L$ to $z = +L$; therefore the maximum and minimum Larmor frequencies are $\pm\gamma GL$. The spectrum will be non-zero between these two frequencies, with a amplitude at each frequency depending on the size of the sample in the xy -plane at the corresponding position. In other words, the spectrum is an image of the cell when a field gradient is applied. The spectral width due to the field gradient is known as inhomogeneous broadening; the decay time of the free induction signal is often known as T_2^* (see below).

1.2.3 Spin Relaxation and Diffusion

The spins in a real sample are not independent of one another. Their interactions mean that the magnetisation can decay towards equilibrium ($M_x = 0$, $M_y = 0$, and $M_z = M_0$). The decay time-constant for the component of magnetisation parallel the magnetic field (the z -direction) is T_1 ; for components perpendicular is T_2 . By including the decay terms, Eqn. (1.18) becomes the Bloch equation (Eqn. (38a) to (38c) of Ref. [32] cast into vector form):

$$\frac{d\mathbf{M}}{dt} - \mathbf{M} \times \boldsymbol{\Omega}_0 = \frac{(M_0 - M_z)\hat{\mathbf{z}}}{T_1} - \frac{M_x\hat{\mathbf{x}} + M_y\hat{\mathbf{y}}}{T_2} \quad (1.19)$$

The relaxation of transverse components T_2 can be observed in the decay of an FID experiment. The FID signal also decays when the magnetic field is inhomogeneous (Fig. 1.6), although the loss of signal is not due to relaxation of magnetisation, but due to loss of coherence. The time-scale for inhomogeneous broadening is sometimes called T_2^* and is approximately $1/\gamma GL$.

The relaxation time-scales depend on the material properties of the sample being studied. The coupling of an individual spin to the rest of the sample is known as spin-lattice interaction, and is the primary cause of relaxation. It may be that the spin-lattice interaction is in the bulk of the sample, or that it occurs at interfaces, and is propagated by spin diffusion.

Another source of loss in NMR is spin diffusion within the bulk, which is very small in many solids, but can be large in fluid NMR. If the magnetisation varies with position (as in an FID when the magnetic field is inhomogeneous), then spin diffusion is possible (see section 1.1.4). When diffusion is present, the Bloch equation must be modified to agree with Eqn. (1.10). The resulting equation is the Torrey equation[33]:

$$\frac{d\mathbf{M}}{dt} - \mathbf{M} \times \boldsymbol{\Omega}_0 = \frac{(M_0 - M_z)\hat{\mathbf{z}}}{T_1} - \frac{M_x\hat{\mathbf{x}} + M_y\hat{\mathbf{y}}}{T_2} + D\nabla^2\mathbf{M} \quad (1.20)$$

where it assumed (for simplicity) that the diffusion coefficient D is both isotropic and homogeneous. In the limit of no spin-lattice relaxation (T_1 and T_2 going to infinity), the above equation agrees with Eqn. (1.11), with the addition of the Larmor precession.

1.2.4 Spin Echoes

It is difficult to separate the true relaxation processes (spin-lattice interaction, diffusion) from inhomogeneous broadening using an FID experiment: the spin-echo experiment is required. The spin-echo experiment involves two pulses separated by

a suitable waiting time. The angles of the pulses depend on the exact technique required; all the experiments described in this thesis involve a small, initial, tipping pulse (θ) and an inverting second pulse (180°), known as the π -pulse.

The initial pulse excites some transverse magnetisation, which we will assume to be uniform: Fig. 1.7(a). Precession occurs, with the rate depending on position, when there is a magnetic field gradient. The magnetisation winds-up into a helix (b) (a process also called de-phasing): parts of the magnetisation gain phase relative to other parts. The π -pulse causes the longitudinal magnetisation M_z to be inverted (not shown in figure) and the transverse magnetisation also to be inverted (c): the helix is reversed. Precession continues, and the parts of magnetisation which were behind in phase are now in front and vice versa. Those parts which now have advanced phase are precessing slower, so the effects of de-phasing are reversed (re-phasing) and the helix is unwound (d).

The initial signal (a) decays as de-phasing occurs. At (b) and (c) very little signal is observed, but then re-phasing means that the signal returns at (d): hence the name spin echo. The time between second pulse and echo will be the same as the time between pulses. The phase of the echo will be 180° different from the initial phase, due to the inverting effect of the π -pulse. The amplitude of the echo will be lower than the initial signal because of irreversible processes (spin-lattice interaction and diffusion), but the effect of the inhomogeneous broadening T_2^* has been avoided.

Diffusion will occur because the magnetisation is not uniform (varying in direction). Torrey[33] showed that the amplitude of the echo signal (as a proportion of the initial signal) will decay exponentially with the cube of the waiting time between pulses:

$$\ln |h| = -\frac{2}{3}D\gamma^2G^2t_w^3 \quad (1.21)$$

where t_w is the inter-pulse waiting time and $h = S(2t_w)/S(0)$. The spin-lattice relaxation times T_1 and T_2 are taken to be much longer than the duration of the experiment.

1.2.5 Inversion-Recovery Experiments

To measure the intrinsic longitudinal spin-lattice interaction decay constant, T_1 , we can use an inversion-recovery experiment. First the magnetisation is tipped away from equilibrium, usually by 90° or 180° . The sample is allowed to relax for a time comparable to T_1 , then a small-angle tipping pulse is applied, and the FID observed.

If we assume that there is no transverse magnetisation present just before the pulse, then the transverse magnetisation after the pulse should be proportional to

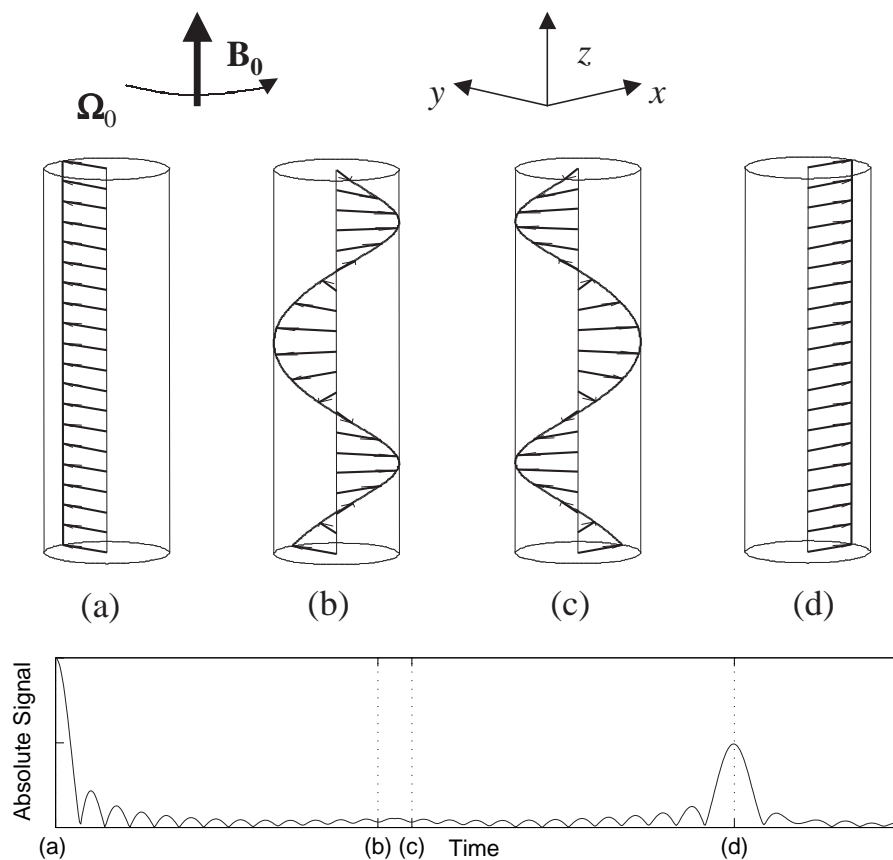


Figure 1.7: Spin Echo: (a) Initial tipping and signal is the same as an FID experiment. (b) The magnetisation de-phases due to magnetic field inhomogeneity, some magnetisation races ahead of others. The signal is therefore reduced. (c) The π -pulse inverts the magnetisation; parts which were ahead are now behind. (d) The magnetisation re-phases as precession continues. Signal returns, reduced due to irreversible relaxation and diffusion processes.

the longitudinal magnetisation, for a given tipping angle. Since the signal is proportional to the (integral of) transverse magnetisation, the signal should be proportional to the longitudinal magnetisation. It is sometimes easier to measure the integral of induction signal over time (or integral of spectrum over frequency), depending on the details of the experiment. A series of such pulses and observations are performed, with suitable waiting periods, and the results compared with an exponential decay towards equilibrium. The longitudinal relaxation time can be measured from the decay constant of the magnetisation with time, and the magnetisation (as a proportion of the equilibrium magnetisation) can be retrospectively determined for each of the experiments.

1.3 Low-Temperature NMR experiments on ^3He

There have been many NMR experiments on ^3He and ^3He - ^4He mixtures at low temperature, using variety of pulse-sequences to study the spin-dynamics in solid and liquid phases. Some of the FIDs, when turned into spectra, show complex behaviour, with long-lived signals (sharp peaks in the spectrum). Spin-echoes show changes in amplitude and phase due to the Leggett-Rice spin-rotation effect.

1.3.1 Long-lived FID signals: Magnetic Modes

There are several phenomena capable of producing long-lived NMR signals in ^3He at low temperatures. In the superfluid- B phase of ^3He , there are Homogeneous Precessing Domains[34] which are strictly non-linear, with lifetimes sometimes over 100ms, even in aerogel[35]. In solid ^3He , persistent magneto-static modes have been observed[36] at millikelvin temperatures (see Fig. 1.8). The Leggett-Rice effect produces magneto-dynamic modes with lifetimes up to 50ms at similar temperatures (for example, Candela *et al*, 1986[37]). Spectral clustering has been seen in hyperpolarised ^3He films by Nacher *et al*[38]. Previously published data from the Nottingham group show the existence of an unexplained, long-lifetime, linear phenomenon in normal liquid ^3He [39][40].

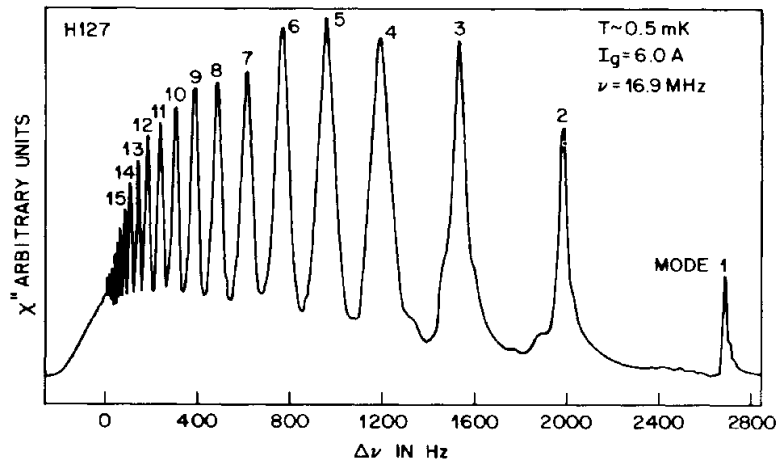


Figure 1.8: Spectrum showing sharp peaks in highly polarised solid ^3He : taken from Osheroff and Cross[36]. A small magnetic field gradient has been applied. The sharp peaks correspond to magneto-static modes, due to the self-consistent magnetic field (known as the demagnetising field or dipolar field) generated by the magnetisation of the ^3He . Note that solid ^3He is ferromagnetic.

Some of these phenomena cannot be understood without reference to the demagnetising field: the field produced by the magnetisation of the ^3He itself. The

demagnetising field is treated in some depth in chapter 4 of this thesis.

1.3.2 Leggett-Rice effect: Spin Waves

Spectroscopic experiments can show the presence of weakly-damped magneto-dynamic modes associated with the Leggett-Rice spin-rotation effect (or Silin spin-waves[29]). The damping of such modes should increase with D_{\perp} and decrease with μM_0 . The first observation of spin-waves was by Owers-Bradley *et al*[41] in concentrated ^3He - ^4He mixtures, using a continuous-wave technique. See Table 3.1 for references to further spin-wave experiments in ^3He - ^4He mixtures.

Some of the most interesting results are due to Vermeulen and Roni, published 2000[42] and 2001[43], in saturated ^3He - ^4He solution at 7 bar pressure (9.3% ^3He). They used a non-equilibrium, enhanced-polarisation technique to increase both spin-rotation and the anisotropy temperature by a factor of up to five over their equilibrium values. As shown in Fig. 1.9, the damping was seen to decrease as the temperature decreased, showing no sign of the saturation associated with spin-transport anisotropy. They placed an upper limit on the equilibrium anisotropy temperature of 2.7mK in a 10.5T field. Their result does not contradict either theory (saturation or no saturation) because the concentration is too great for the dilute-limit approximations to be strictly valid, and the limit does not rule out the quantitative predictions of Jeon and Mullin[21]

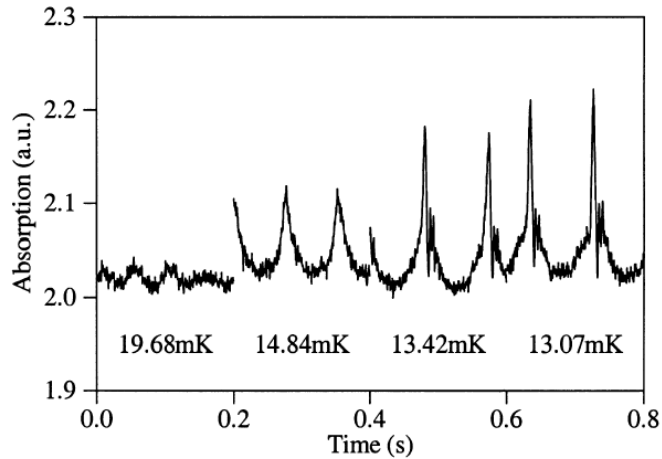


Figure 1.9: Spin-Wave Spectrum: Damping of spin-wave modes decreases with temperature, showing no saturation, even at lowest temperatures. Line-widths can be less than 100Hz. Figure from Roni and Vermeulen[42].

1.3.3 Leggett-Rice effect: Spin Echoes

The Torrey equations Eqn. (1.20) and Eqn. (1.21) are modified by the presence of the Leggett-Rice spin-rotation effect[25][26]. When T_1 and T_2 are taken to be infinity, the equation of motion in the rotating frame is (from Eqn. (1.17)):

$$\begin{aligned} \frac{\partial \mathbf{M}(\mathbf{r}, t)}{\partial t} - \mathbf{M} \times \boldsymbol{\Omega}_0(\mathbf{r}) \\ = D_0 \sum_{i=1}^3 \frac{\partial}{\partial x_i} \left[\frac{1}{1 + \mu^2 M_0^2} \left\{ \frac{\partial \mathbf{M}}{\partial x_i} + \mu \left(\mathbf{M} \times \frac{\partial \mathbf{M}}{\partial x_i} \right) + \mu^2 \left(\mathbf{M} \cdot \frac{\partial \mathbf{M}}{\partial x_i} \right) \mathbf{M} \right\} \right] \end{aligned} \quad (1.22)$$

Results of a spin-echo experiment can be derived: as the magnitude of the magnetisation should be constant, the last term in Eqn. (1.22) vanishes. The transverse components of magnetisation can be combined into a single complex quantity: $M_+ = M_x + iM_y$; then the solution can be written in the form:

$$M_+(\mathbf{r}, t) = A(t) e^{i\phi(t)} e^{-i\zeta(\mathbf{r}, t)} \quad (1.23)$$

The longitudinal magnetisation is $M_z = M_0 \cos \theta$. The phase factor obeying $\frac{\partial \zeta}{\partial t} = \boldsymbol{\Omega}_0(\mathbf{r})$ is due to Larmor precession; ϕ is due to the spin-dynamics. The effect of a π -pulse is to invert the magnetisation: $M_z \rightarrow -M_z$, $\phi \rightarrow -\phi$, and $\zeta \rightarrow -\zeta$. Thus differential equations governing the amplitude and phase of an echo can be derived, and integrated. When the initial tipping angle θ is small, the equations reduce to:

$$\Delta \phi = -\mu M_0 \ln |h| \quad (1.24a)$$

$$\ln |h| = -\frac{2}{3} \frac{D_0 \gamma^2 G^2}{1 + (\mu M_0)^2} t_w^3 \quad (1.24b)$$

Corrections for large angles are made by Leggett[26]. The above equations require that the gradient is constant through space, and the boundaries are taken to be at infinity (an unbounded region is being studied). If spin diffusion is anisotropic D_\perp is to be substituted for D_0 . The equations reduce to the Torrey equation for echo-amplitude Eqn. (1.21) when μM_0 is zero.

When μM_0 is finite, the phase of the echo $\Delta \phi$ varies due to the influence of the molecular field (the spin-rotation effect). Also, the decay of spin-echoes is modified by spin rotation, i.e. the effective spin-diffusion coefficient is $\frac{D_0}{1 + (\mu M_0)^2}$. This coefficient should show a maximum[25] when $|\mu M_0| = 1$, and increase as T^2 at low temperature (in contrast with the simple diffusion-coefficient which is proportional to $1/T^2$)[†].

[†]The temperature variation assumes that $\tau_\perp \propto T^{-2}$, and that μM_0 and D_\perp are proportional to τ_\perp , i.e. the two spin-transport coefficients have the same temperature variation. μM_0 is also proportional to the applied magnetic field.

Spin-Echo Experimental Results

There have been a number of spin-echo experiments measuring the spin-transport coefficients, in pure ^3He and in mixtures; the theories (section 1.1.4, pages 7 to 11) are only valid for a Fermi gas, i.e. very dilute mixtures.

The first experiments in pure ^3He by Corruccini *et al*(1971)[44] showed the expected maximum in the effective, transverse spin-diffusion coefficient $\frac{D_0}{1+(\mu M_0)^2}$, at around 9mK ($B_0 = 0.73\text{T}$) or 13mK (1.13T): the scaling is consistent with $\mu M_0 \propto B_0$. Further experiments in higher field have shown that the transverse spin-diffusion coefficient and the spin-rotation parameter saturate below about 15mK: Wei *et al*[45] measured 16.4mK in 8T (see Fig. 1.10) and Candela *et al*[39] measured 12mK in 11.3T (see below, and also chapter 3). The spin-rotation parameter has also been determined, using the equation of Leggett, Eqn. (1.24).

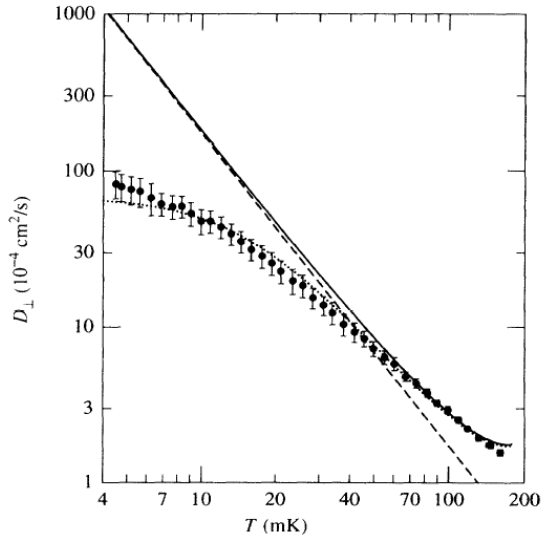


Figure 1.10: Transverse Spin-Diffusion coefficient, pure ^3He at saturated vapour pressure: taken with 8 tesla field. Dashed curve shows T^{-2} dependence, solid curve includes spin-fluctuation term. Dotted curve is a fit to Eqn. (1.14), with a correction for spin-fluctuations. Data (points) derived from spin-echo experiments. The anisotropy temperature is $T_a = 16.4 \pm 2.2\text{mK}$. Figure from Wei *et al*[45], Fig. 1.

There have been more spin-echo experiments in ^3He - ^4He mixtures: most notably Ager *et al*[28] in various concentrations (see Fig. 1.11 for saturated-solution measurements); and Akimoto *et al*[46][47]. A more detailed comparison is given in Table 3.1 and section 3.1. Ager *et al* observed a difference between the longitudinal and transverse spin-diffusion coefficients (an explicit observation of anisotropy), although the experimental technique for measuring longitudinal spin-diffusion was not exactly the same as for transverse spin-transport.

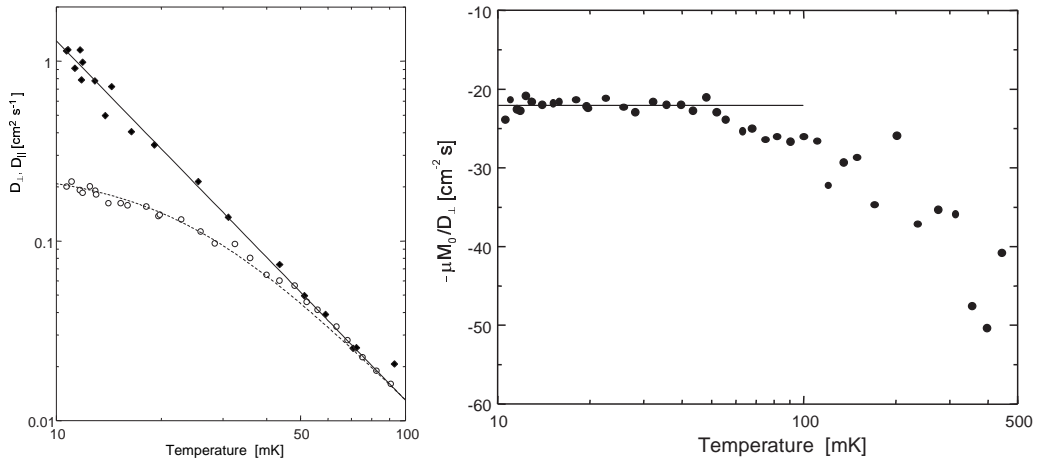


Figure 1.11: Spin-Diffusion anisotropy, 6.2% ${}^3\text{He}$ - ${}^4\text{He}$: after Ager *et al*[28], Fig. 6 and Fig. 11. Longitudinal spin-diffusion D_{\parallel} (black diamonds, left figure) goes like $1/T^2$ as for a simple Fermi-liquid transport parameter. Transverse spin-transport D_{\perp} saturates as $1/(T^2 + T_a^2)$, with $T_a = 19 \pm 3\text{mK}$. Below $\sim 50\text{mK}$, the spin-rotation parameter μM_0 is proportional to D_{\perp} (right figure). The Fermi temperature for this system is about 400mK.

The predictions of theory are clearer at very low temperatures for ${}^3\text{He}$ - ${}^4\text{He}$ mixtures than for pure ${}^3\text{He}$, but the Fermi temperature increases with the cube-root of concentration. In the saturated mixture, the Fermi temperature is around 420mK; in 0.5% ${}^3\text{He}$, just 70mK. High-temperature deviations are observed above roughly $T_F/10$, meaning the $1/(T^2 + T_a^2)$ behaviour is only expected at the very lowest temperatures.

It is notable that the results of all spin-echo experiments are in disagreement with the spin-wave measurements of Vermeulen and Roni, with the exception of the most recent, high-field work of Akimoto *et al*[47] (which was performed in 3.8% ${}^3\text{He}$ - ${}^4\text{He}$ where the Landau parameters cancel such that spin-rotation disappears).

1.3.4 Experiments in Nottingham, 1999–2000

High-field, low-temperature NMR experiments were performed in Nottingham from Autumn 1999 to Summer 2000, on ${}^3\text{He}$ and ${}^3\text{He}$ - ${}^4\text{He}$ mixtures at saturated vapour pressure. The experimental cell was a cylinder with axis parallel to the magnetic field; the field was 11.3T corresponding to a Larmor frequency of about 370MHz. The group leader was John Owers-Bradley, and the other experimentalists were (in alphabetical order): O. Buu, D. Candela, D. Clubb, R. König, G. Vermeulen. Theoretical support was provided by R.M. Bowley. The preliminary results of these experiments were published: pure ${}^3\text{He}$ by Candela *et al*[39] and 6.2% ${}^3\text{He}$ (nearly

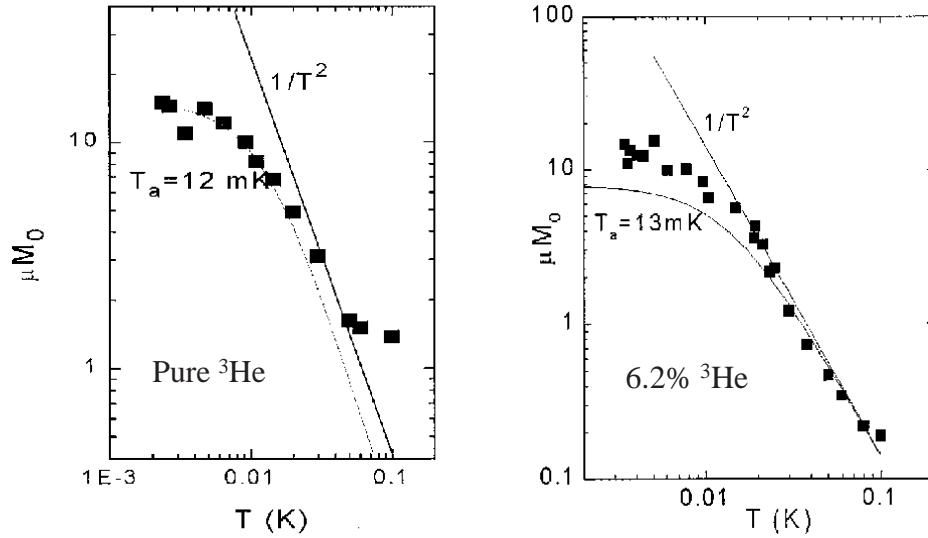


Figure 1.12: Results of Nottingham NMR Experiments on ${}^3\text{He}$, 1999/2000, in 11.3T magnetic field: Saturation typical of spin-transport anisotropy is seen in both pure ${}^3\text{He}$ and saturated ${}^3\text{He}$ - ${}^4\text{He}$ solution, with different temperature scales. Left panel after Candela *et al*[39], right panel after Owers-Bradley *et al*[48]

saturated mixture) by Owers-Bradley *et al*[48]. Work on 0.5% ${}^3\text{He}$ - ${}^4\text{He}$ remains unpublished.

Both spectroscopic and spin-echo data were acquired, and the same experimental apparatus was used for all three concentrations. The anisotropy temperature was derived from in a field of 11.3T, from spin-echo experiments, using Eqn. (1.24)(a and b): in pure ${}^3\text{He}$ the result was $T_a = 12 \pm 2\text{mK}$; and 13mK in 6.2% ${}^3\text{He}$ - ${}^4\text{He}$. The spin-rotation parameters derived are shown in Fig. 1.12.

Discrete peaks were seen in the FID spectrum, which is characteristic of the Leggett-Rice effect when spin-transport is confined by the walls of the experimental cell. Even longer-lived modes were observed in pure ${}^3\text{He}$ [39], which are believed to have been a consequence of the demagnetising field (the magnetic field due to the magnetisation of the sample).

1.4 Remaining Questions

The results of low-temperature NMR experiments on liquid helium-3 yield inconsistent results for saturation of transport parameters (τ_{\perp} , D_{\perp} and μM_0), therefore also inconsistent results for T_a . Furthermore, there is no consensus on the theoretical picture of spin-dynamics. How can these disagreements be resolved?

First, the experiments are not testing exactly the same systems. Boundary effects

are often important, but the experimental geometries are not identical: cylinders parallel and perpendicular to the field, spheres, hemispheres and more complicated cells are used. The concentrations vary from 0.09% to 100% ^3He , and not all experiments are at zero pressure, i.e. the Landau parameters are not expected to be the same for all systems studied. The only spin-wave damping experiment[43] detects no saturation of τ_{\perp} using continuous-wave measurements; the spin-echo experiments all detect finite T_a or some saturation of τ_{\perp} , using two-pulse measurements.

Second, none of the experiments is ideal. (1.) Spectroscopic experiments are very sensitive to unwanted, poorly-known, magnetic field variations. The analysis from Leggett[26], or something similar, is used for all the spin-echo experiments. Moreover (2.) the NMR pulses do not cause perfect inversion of the magnetisation when a field inhomogeneity is present. (3.) An assumption of the Leggett analysis is that the boundaries of the experimental cell are negligible, which is not valid for all the experiments. For experiments in pure ^3He at high field, the macroscopic magnetic field due to the sample, the demagnetising field, affects the spin-dynamics. (4.) In very dilute ^3He - ^4He mixtures the mean free path is very long, so Leggett's hydrodynamic equations may not be valid, since they are based on Landau Fermi-liquid theory. (5.) Any form of NMR introduces heat (through Joule heating), which may cause unwanted and undetected temperature rises, mimicking the predicted saturation of transverse spin-transport parameters.

Third, the only experiment with a sufficiently dilute sample[46] to be compared directly to numerical theoretical predictions has very long mean free path, and so may suffer from mean free path effects. Saturation is detected at much lower μM_0 than expected, indicating something is amiss. Also, the Fermi temperature is so low that high temperature effects may be apparent even near to the saturation temperature, making it impossible to distinguish one effect from another. Further theoretical work is needed if such effects are to be understood, and predictions of transport properties for concentrated solutions and pure ^3He are also desirable.

To sum up: the published results of experiments disagree over the anisotropy temperature; there are problems with analysis of every experiment; and the theories do not accurately describe all of the experiments.

1.4.1 Scope and Structure of the Thesis

The idea behind this thesis is that we can eliminate the problems of some of the experiments by means of a simulation, a model of the spin-dynamics. Specifically, we want to model the experiments at Nottingham in 1999/2000, because we have

access to the raw data, and we know the details of the experimental apparatus and method.

Chapter 2 shows how to construct a linear model of the spin-dynamics, based on Eqn. (1.22) with suitable (cylindrical) boundary conditions. The equation of motion is cast into matrix form, and solution is either by a sum over eigenmodes, or by an operator-exponentiation method. The solutions are investigated, and converted into simulations of FIDs and spectra. The model is extended to include simulation of spin-echo experiments with ideal pulses. Some results of the simulations are presented, and indicate that an understanding of the effects of boundaries is essential to understand the results of the Nottingham experiments.

In chapter 3, the details of the experiments are presented. The assumptions of the model are checked, and found to be acceptable for the 6.2% ^3He - ^4He mixture, except for the ideal pulse assumption. Non-ideal pulses are then included in the linear model. The data is then fitted in a least-squares way in comparison with the model, varying the parameters of the model. The spin-transport coefficients are determined for 6.2% ^3He as functions of temperature.

Chapter 4 is an extension to the model of chapter 2, to include the demagnetising field. The linearised equation of motion including demagnetising field is shown to be non-local (non-hydrodynamic), but can be cast into matrix form. Having found the matrix, simulated FIDs, spectra, magnetodynamic modes and spin-echoes are presented, for various values of spin-transport parameters and demagnetising field strength.

The pure ^3He data is presented in chapter 5, and the pathology of long-lived FID signals is studied. Non-equilibrium recovery experiments permit understanding of the effect of magnetisation on the spectrum. The NMR spectroscopic data is compared with results of the extended-model: parameters are adjusted to obtain acceptable fits.

CHAPTER 2

LEGGETT-RICE EFFECT IN A FINITE GEOMETRY

This chapter includes the mathematical formalism for converting the Leggett-Rice equation of motion to a simulation of the common NMR experiments, the FID (one pulse) and the spin-echo (two pulse). The details are for the benefit of anyone who would wish to re-create this work. The appendix [A](#) contains some useful theorems about the mathematical properties of the linearised form of the equation of motion.

2.1 Linearised Leggett-Rice Equation of Motion

In the introduction (section [1.1.5](#), Eqn. [\(1.22\)](#) and also Eqn. [\(1.17\)](#)) the Leggett-Rice equation of motion for the magnetisation in a polarised Fermi-liquid[[26](#)] was shown:

$$\begin{aligned} \frac{\partial \mathbf{M}(\mathbf{r}, t)}{\partial t} - \mathbf{M} \times \boldsymbol{\Omega}_0(\mathbf{r}) \\ = D_0 \sum_{i=1}^3 \frac{\partial}{\partial x_i} \left[\frac{1}{1 + \mu^2 M_0^2} \left\{ \frac{\partial \mathbf{M}}{\partial x_i} + \mu \left(\mathbf{M} \times \frac{\partial \mathbf{M}}{\partial x_i} \right) + \mu^2 \left(\mathbf{M} \cdot \frac{\partial \mathbf{M}}{\partial x_i} \right) \mathbf{M} \right\} \right] \end{aligned} \quad (2.1)$$

The above equation describes the motion of the three-component vector \mathbf{M} , and has terms up to to third order in \mathbf{M} . Generally, it requires a lot of computing power to solve for all vector components using finite elements, which is in practice only possible in one spatial dimension, and time. The simplification we make is

to take only first order variations in magnetisation, transverse to the equilibrium magnetisation direction. The two transverse components of magnetisation can then be combined into a complex scalar quantity, described by a single, linear equation.

Take the magnetisation to be perturbed from equilibrium, \mathbf{M}_0 , by a small quantity \mathbf{m} . Note that \mathbf{M}_0 is taken to be in the z -direction, parallel to the applied field, and \mathbf{m} is perpendicular to the z -direction.

$$\mathbf{M} = \mathbf{M}_0 + \mathbf{m} \quad (2.2a)$$

$$|\mathbf{m}| \ll |\mathbf{M}_0| \quad (2.2b)$$

$$\mathbf{M}_0 \cdot \mathbf{m} = \hat{\mathbf{z}} \cdot \mathbf{m} = 0 \quad (2.2c)$$

$$\mathbf{M}_0 = M_0 \hat{\mathbf{z}} \quad (2.2d)$$

The applied magnetic field is not required to be spatially invariant, but it is in the z -direction: $\boldsymbol{\Omega}_0 = \hat{\mathbf{z}}[\Omega_C + \gamma G(\mathbf{r})]$.

Substituting Eqn. (2.2) into Eqn. (2.1) and ignoring all terms of order $|m|^2$ and $|m|^3$, we find:

$$\begin{aligned} \frac{\partial \mathbf{m}}{\partial t} - (\mathbf{m} \times \boldsymbol{\Omega}_0) = & \quad (2.3) \\ & \sum_{i=1}^3 \left[\frac{D_0}{1 + \mu^2 M_0^2} \left\{ \frac{\partial^2 \mathbf{m}}{\partial x_i^2} + \left(\mu \mathbf{M}_0 \times \frac{\partial^2 \mathbf{m}}{\partial x_i^2} \right) + \mu^2 \left(\mathbf{M}_0 \cdot \frac{\partial^2 \mathbf{m}}{\partial x_i^2} \right) \mathbf{M}_0 \right\} \right] \end{aligned}$$

Noting that \mathbf{M}_0 and \mathbf{m} are perpendicular (as are \mathbf{M}_0 and $\frac{\partial^2 \mathbf{m}}{\partial x_i^2}$), and writing $\sum_i \frac{\partial^2 \mathbf{m}}{\partial x_i^2} = \nabla^2 \mathbf{m}$ and $\frac{\partial \mathbf{m}}{\partial t} = \dot{\mathbf{m}}$, we obtain the linear equation of motion for \mathbf{m} :

$$\dot{\mathbf{m}} - (\mathbf{m} \times \boldsymbol{\Omega}_0) = \frac{D_0}{1 + \mu^2 M_0^2} (1 + \mu \mathbf{M}_0 \times) \nabla^2 \mathbf{m} \quad (2.4)$$

There are only two components of the vector, $\mathbf{m} = m_x \hat{\mathbf{x}} + m_y \hat{\mathbf{y}}$. We write a pair of coupled equations in the $\hat{\mathbf{x}}$ and $\hat{\mathbf{y}}$ directions[†]:

$$\dot{m}_x = +\Omega_0 m_y + \frac{D_0}{1 + \mu^2 M_0^2} (\nabla^2 m_x - \mu M_0 \nabla^2 m_y) \quad (2.5a)$$

$$\dot{m}_y = -\Omega_0 m_x + \frac{D_0}{1 + \mu^2 M_0^2} (\nabla^2 m_y + \mu M_0 \nabla^2 m_x) \quad (2.5b)$$

The second simplification made is to write \mathbf{m} as a single complex number:

$$m_{\pm} = m_x \pm i m_y \quad (2.6)$$

[†]The diffusion coefficient for a vector quantity is strictly a rank-two tensor. For motion of magnetisation in a magnetic field, there are only two distinguishable elements - which we shall call D_{\parallel} and D_{\perp} , corresponding to motion of M_z , and (M_x, M_y) , respectively. Therefore we can replace D_0 with D_{\perp} in all further studies of the motion of the transverse magnetisation.

We combine Eqn. (2.5a) and Eqn. (2.5b):

$$\dot{m}_{\pm} = \mp i\Omega_0 m_{\pm} + \frac{D_0(1 \pm i\mu M_0)}{1 + \mu^2 M_0^2} \nabla^2 m_{\pm} \quad (2.7)$$

We note that $\frac{1 \pm i\mu M_0}{1 + \mu^2 M_0^2} = \frac{1}{1 \mp i\mu M_0}$. Also, we can subtract Ω_C from the Larmor frequency, putting us into the reference frame rotating at the Larmor frequency at the centre of co-ordinates, if we use only the m_- component. The choice will be common throughout this thesis, but it is equally valid to add Ω_C and take m_+ .

Our final form of the linearised Leggett-Rice equation of motion is[†] :

$$\boxed{\frac{\partial m_-(\mathbf{r}, t)}{\partial t} = \left\{ i\gamma G(\mathbf{r}) + \frac{D_{\perp}}{1 + i\mu M_0} \nabla^2 \right\} m_-} \quad (2.8)$$

It is worth noting the similarity between Eqn. (2.8) and the Schrödinger equation. The role of potential is played by the variation in the Larmor frequency, $\gamma G(\mathbf{r})$, and the mass is equivalent to $iD_{\perp}(1 + i\mu M_0)$. The key differences are that the mass can be complex, which leads to decaying ‘stationary states’; and the equation is *complex symmetric*, not Hermitian (see, for example, Rae[49], p64–68, or Appendix A).

We also need to know the boundary conditions: for all the problems dealt with in this thesis, the boundary condition is that there is no spin-current through the surface of the experimental cell:

$$(\hat{\mathbf{n}} \cdot \nabla) m_- = 0 \quad (2.9)$$

where $\hat{\mathbf{n}}$ is the unit vector normal to the surface. The boundary condition comes from the requirement that there is no spin-current going into the wall of the experimental cell, which is not absolutely correct, but accurate enough for our purposes. We can neglect spin-relaxation at the walls: see Candela *et al*(1986)[37] for a more thorough analysis. There will be an initial condition which depends upon the exact experiment being studied.

There are some comments on the properties of Eqn. (2.8) in Appendix A. Without such understanding of the properties of the equation of motion, it would be almost impossible to simulate spin-echoes using the matrix method.

[†]There is a sign convention choice here; it is physically reasonable to take m_- . Imagine setting the transport coefficients in Eqn. (2.7) to zero, and note that $\Omega_0 = \gamma G(\mathbf{r})$. If the field is homogeneous ($G = \text{constant}$) then the solution is a homogeneous magnetisation precessing at $+i\gamma G$ if we take m_- . It is important to note that γ is a negative quantity for ^3He . Therefore increasing magnetic field corresponds to decreasing frequency.

The Magnetic Field

It is important to realise that the spatial variation of the magnetic field, $G(\mathbf{r})$, must be a solution of Maxwell's equations. Within the cell there are no free electrical currents or free electric charges, and the electric and magnetic fields are independent of time. Therefore $\nabla \times \mathbf{B} = 0$, so the magnetic field \mathbf{B} can be written as the gradient of a scalar potential: $\mathbf{B} = \nabla \phi_M$. There is no divergence of the magnetic field, so the scalar potential satisfies Laplace's equation: $\nabla^2 \phi_M = 0$ (see for example Bleaney and Bleaney[50], 3rd Ed. (Vol. 1): p111–112, equation (4.36) and p34–37 Table 2.1).

In spherical polar co-ordinates, we can write the potential as a sum over Legendre polynomials multiplied by positive powers of radial co-ordinate (negative powers would lead to the existence of a magnetic monopole at the origin of co-ordinates)[†]:

$$\phi_M = \sum_{l=0} H_l r^l P_l^0(\cos \theta) \quad (2.10)$$

It easiest to expand ϕ_M in Cartesian co-ordinates, and differentiate, then take only the z component ($B_z = \frac{\partial \phi_M}{\partial z}$), since the effect of off-axis components is at least second order in the equation of motion Eqn. (2.4). It turns out that the z -component of the field can be written as a sum of Legendre polynomials, exactly as ϕ_M , but with coefficients $G_l = lH_l$.

$$B_z = G(\mathbf{r}) = G_0 + G_1 r P_1^0(\cos \theta) + G_2 r^2 P_2^0(\cos \theta) + \dots \quad (2.11)$$

The constant term G_0 is of course the magnetic field at the origin of co-ordinates, Ω_C/γ .

2.2 Matrix Representation in a Cylinder

There are at least two ways to solve a linear, partial-differential equation: considered here are finite-differencing or finite element[51]; and matrix representation[‡]. The former method is conceptually the easiest, but can be computationally hard work. Matrix representation is a route often chosen for solving Eqn. (2.8). The geometry of a cylinder, axis aligned with polarising field, is the most relevant: Chapter 3 is an attempt understand experiments performed in just such a cell, using ³He-⁴He mixtures [53][54][48]. The matrix representation method is based around a

[†]The first three Legendre polynomials are $P_0^0(u) = 1$; $P_1^0(u) = u$; $P_2^0(u) = \frac{1}{2}(3u^2 - 1)$

[‡]Ragan(1995)[52] has a different approach, involving algebraic substitutions, changes of variable, perturbation theory and approximations.

pseudo-hamiltonian operator equal to $\frac{\partial}{\partial t}$: see Eqn. (2.8). Note the factor of i , the imaginary number, times the definition of Appendix A, which is acceptable because the equations are linear.

In real, dimensioned units, the action of the pseudo-hamiltonian is:

$$\hat{H}m_-(\mathbf{r}, t) = \frac{\partial m_-(\mathbf{r}, t)}{\partial t} = \left\{ i\gamma G(\mathbf{r}) + \frac{D_\perp}{1 + i\mu M_0} \nabla^2 \right\} m_- \quad (2.12)$$

Eqn. (2.12) will be used to derive a matrix to describe motion in the two physically relevant dimensions (axial and radial).

2.2.1 Equation of motion in Cylindrical Coordinates

There are natural co-ordinates for a cylinder, with axis aligned to static field: z axial, r radial and φ angular coordinates. We take the region of interest (the *cell*), to extend from $z = -L \rightarrow +L$ and $r = 0 \rightarrow \alpha L$, where α is the aspect ratio of the cell.

In cylindrical polar co-ordinates, the equation of motion Eqn. (2.8) is separable, if we take field variations up to second order[†]:

$$G(\mathbf{r}) = G_1 z + G_2 (z^2 - \frac{1}{2} r^2) \quad (2.13a)$$

$$m_-(\mathbf{r}, t) = \Psi(z, t) \Phi(r, t) \Upsilon(\varphi, t) \quad (2.13b)$$

$$\frac{\partial \Psi(z, t)}{\partial t} = i\gamma (G_1 z + G_2 z^2) \Psi + D_{\text{eff}} \frac{\partial^2 \Psi}{\partial z^2} \quad (2.13c)$$

$$\frac{\partial \Phi(r, t)}{\partial t} = -\frac{i\gamma G_2 r^2}{2} \Phi + D_{\text{eff}} \frac{1}{r} \frac{\partial}{\partial r} \left(r \frac{\partial \Phi}{\partial r} \right) \quad (2.13d)$$

$$\frac{\partial \Upsilon(\varphi, t)}{\partial t} = D_{\text{eff}} \frac{1}{r^2} \frac{\partial^2 \Upsilon}{\partial \varphi^2} \quad (2.13e)$$

The boundary condition Eqn. (2.9) is also separable:

$$\left. \frac{\partial \Psi}{\partial z} \right|_{z=\pm L} = 0 \quad \left. \frac{\partial \Phi}{\partial r} \right|_{r=0, \alpha L} = 0 \quad (2.14)$$

The only relevant solution to Eqn. (2.13e) is the trivial solution: $\Upsilon(\varphi, t) = 1$, i.e. there is complete angular symmetry in the physics, so we can drop the angular factor from all our subsequent analysis.

It is convenient to define the dimensionless coordinates

$$\zeta = z/L \quad -1 \leq \zeta \leq +1 \quad (2.15a)$$

$$\rho = r/\alpha L \quad 0 < \rho \leq +1 \quad (2.15b)$$

$$\tau = t D_{\text{eff}} / L^2 \quad (2.15c)$$

[†]for clarity, $D_{\text{eff}} = D_\perp / (1 + i\mu M_0)$ is defined to be the complex, effective spin-diffusion coefficient.

and quantities (dimensionless gradient parameters):

$$b_1 = \gamma G_1 L^3 / D_{\text{eff}} \quad b_2 = \gamma G_2 L^4 / D_{\text{eff}} \quad (2.15d)$$

In these units, the equations of motion are

$$\frac{\partial \Psi(\zeta, \tau)}{\partial \tau} = i(b_1 \zeta + b_2 \zeta^2) \Psi + \frac{\partial^2 \Psi}{\partial \zeta^2} \quad (2.16a)$$

$$\frac{\partial \Phi(\rho, \tau)}{\partial \tau} = -\frac{i b_2 \alpha^2 \rho^2}{2} \Phi + \frac{1}{\rho} \frac{\partial}{\partial \rho} \left(\rho \frac{\partial \Phi}{\partial \rho} \right) \quad (2.16b)$$

with boundary conditions

$$\left. \frac{\partial \Psi(\zeta, \tau)}{\partial \zeta} \right|_{\zeta=\pm 1} = 0 \quad \left. \frac{\partial \Phi(\rho, \tau)}{\partial \rho} \right|_{\rho=0,1} = 0 \quad (2.17)$$

Therefore, the dimensionless pseudo-hamiltonian operators for each dimension are defined to be equal to $\frac{\partial}{\partial \tau}$:

$$\hat{H}^{(z)} = i(b_1 \zeta + b_2 \zeta^2) + \frac{\partial^2}{\partial \zeta^2} \quad (2.18a)$$

$$\hat{H}^{(z)} = -\frac{i b_2 \alpha^2 \rho^2}{2} + \frac{1}{\rho} \frac{\partial}{\partial \rho} \left(\rho \frac{\partial}{\partial \rho} \right) \quad (2.18b)$$

From Eqn. (2.18a) and Eqn. (2.18b) matrix equations can be formed, to be solved numerically.

2.2.2 Cylindrical Basis Set and Matrix Elements

First we define a representation: a basis set which satisfies the boundary conditions Eqn. (2.17); one set for each of the separated equations of motion: A_n for Eqn. (2.16a) and B_l for Eqn. (2.16b).

$$A_n = \Theta_n \cos(k_n(\zeta + 1)) \quad B_l = \Xi_l J_0(\kappa_l \rho) \quad (2.19)$$

$$\Theta_0 = 2^{-\frac{1}{2}} \quad \Theta_{n>0} = 1 \quad \Xi_l = \frac{\sqrt{2}}{|J_0(\kappa_l)|} \quad (2.20)$$

where the J_0 is a cylindrical Bessel function, and Θ_n and Ξ_n are normalisation factors such that:

$$\int_{-1}^{+1} d\zeta A_n^2(\zeta) = \int_0^{+1} \rho d\rho B_l^2(\rho) = 1 \quad (2.21)$$

The wave-numbers k_n and κ_l are chosen to satisfy Eqn. (2.17):

$$k_n = n\pi/2 \quad J'_0(\kappa_l) = -J_1(\kappa_l) = 0 \quad (2.22)$$

The wave-numbers must be found numerically, achieved using MATLAB, with help from Abramowitz and Stegun [55], chapter 9, 'Bessel Functions of Integer Order'.

We use the definition of matrix elements from Eqn. (A.7) to produce separate pseudo-hamiltonian matrices for each dimension:

$$H_{nn'}^{(z)} = \int_{-1}^{+1} d\zeta A_n \hat{H}^{(z)} A_{n'} \quad (2.23a)$$

$$H_{ll'}^{(r)} = \int_0^{+1} \rho d\rho B_l \hat{H}^{(r)} B_{l'} \quad (2.23b)$$

Note that, since the basis functions are purely real, we could have used the text-book definition (see Rae[49], p65), with the complex conjugates: see Appendix A. The pseudo-hamiltonian operators are taken from Eqn. (2.16a) and Eqn. (2.16b), and can be divided further into kinetic, \hat{T} , and potential, \hat{V} , terms, as in Eqn. (2.24):

$$\hat{T}^{(z)} = \frac{\partial^2}{\partial \zeta^2} \quad \hat{V}^{(z)} = i(b_1 \zeta + b_2 \zeta^2) \quad (2.24a)$$

$$\hat{T}^{(r)} = \alpha^{-2} \frac{1}{\rho} \frac{\partial}{\partial \rho} \left(\rho \frac{\partial}{\partial \rho} \right) \quad \hat{V}^{(r)} = -i \frac{b_2}{2} \alpha^2 \rho^2 \quad (2.24b)$$

Some elements can be found analytically, some need to be integrated numerically, for which we use MATLAB. The axial, potential matrix elements (with exceptions for n or $n' = 0$) are given by:

$$V_{nn'}^{(z)} = i \frac{\Theta_n \Theta_{n'}}{\pi} \left\{ b_1 \left[\frac{I^{(1)}}{\pi} - I^{(0)} \right] + b_2 \left[\frac{I^{(2)}}{\pi^2} - \frac{2I^{(1)}}{\pi} + I^{(0)} \right] \right\} \quad (2.25)$$

$$I_{nn'}^{(0)} = \int_{x=0}^{2\pi} dx \cos \frac{nx}{2} \cos \frac{n'x}{2} = \pi \delta_{nn'}$$

$$I_{nn'}^{(1)} = \int_{x=0}^{2\pi} dx x \cos \frac{nx}{2} \cos \frac{n'x}{2} = -2 \left\{ \frac{(-1)^{(n+n')} - 1}{(n+n')^2} + \frac{(-1)^{(n-n')} - 1}{(n-n')^2} \right\}$$

$$I_{nn'}^{(2)} = \int_{x=0}^{2\pi} dx x^2 \cos \frac{nx}{2} \cos \frac{n'x}{2} = 8\pi \left\{ \frac{(-1)^{(n+n')}}{(n+n')^2} + \frac{(-1)^{(n-n')}}{(n-n')^2} \right\}$$

The axial, kinetic matrix elements are given by:

$$T_{nn'}^{(z)} = -\Theta_n \Theta_{n'} \left(\frac{\pi n}{2} \right)^2 \delta_{nn'} \quad (2.26)$$

The radial, potential matrix elements are given by:

$$V_{ll'}^{(r)} = -i \frac{b_2}{2} \alpha^2 \Xi_l \Xi_{l'} \int_{\rho=0}^1 \rho d\rho \rho^2 J_0(\kappa_l \rho) J_0(\kappa_{l'} \rho) \quad (2.27)$$

The radial integral is to be calculated numerically. The radial, kinetic matrix elements are given by (the normalisation factors cancel with the integral after differentiation):

$$\begin{aligned} T_{ll'}^{(r)} &= \Xi_l \Xi_{l'} \alpha^{-2} \int_{\rho=0}^1 \rho d\rho J_0(\kappa_l \rho) \frac{1}{\rho} \frac{\partial}{\partial \rho} \left(\rho \frac{\partial}{\partial \rho} \right) J_0(\kappa_{l'} \rho) \\ &= -\alpha^{-2} \kappa_l^2 \delta_{ll'} \end{aligned} \quad (2.28)$$

2.2.3 Eigenfunction or Operator Method

Two matrix-based methods for solving the equations of motion Eqn. (2.16a) and Eqn. (2.16b) have been employed, in the representation of Eqn. (2.19): the *eigenfunction* method, and *operator exponentiation*. Solving for eigenfunctions takes something like N^3 computational operations (see *Numerical Recipes*[56], p74–76 and p335–342), but thereafter calculating signals or spectra is very rapid; for certain parameters this method has serious numerical errors (see section 2.4.4). Exponentiating the operator takes of order N^2 operations, which must be calculated for each point in time; this method is robust for all parameters. Therefore there is a computational-efficiency trade-off, which usually results in using the eigenfunction method (as in all calculations in the current chapter).

For both methods, we have chosen to use internal MATLAB routines[†]. The matrices produced are sparse, often with dominant diagonal elements, and are complex symmetric (see Appendix A).

Eigenfunction Method

The eigenvalue equation for the combination of pseudo-hamiltonians produces stationary states, Ψ_{nl} , with exponential time-dependence:

$$\Psi_{nl}(\zeta, \rho, \tau) = \psi_n(\zeta) \phi_l(\rho) e^{+(\omega_n^{(z)} + \omega_l^{(r)})\tau} \quad (2.29)$$

$$\hat{H}^{(z)}\psi_n = \omega_n^{(z)}\psi_n \quad \hat{H}^{(r)}\phi_l = \omega_l^{(r)}\phi_l \quad (2.30)$$

The normalisation of eigenfunctions is such that $\int_V \Psi_{nl}^2 d^3\mathbf{r} = 1$, as in Appendix A. The eigenfunction method requires that the eigenfunctions form a complete, orthogonal basis set, which can be shown to be true from the properties of the equation of motion: see Appendix A.

Therefore, the time-evolution of magnetisation can be described as a separable sum over eigenfunctions:

$$m_-(\zeta, \rho, \tau) = \left(\sum_{\text{all } n} a_n^{(z)} \psi_n(\zeta) e^{\omega_n^{(z)}\tau} \right) \left(\sum_{\text{all } l} a_l^{(r)} \phi_l(\rho) e^{\omega_l^{(r)}\tau} \right) \quad (2.31)$$

The amplitudes, a_n depend on the initial condition for the total magnetisation, $m_-(\zeta, \rho, 0)$ (see Eqn. (A.11) and Eqn. (A.12)). We choose to use the MATLAB routine `eig`[57] to find all the eigenvectors and eigenvalues of the pseudo-hamiltonian matrices.

[†]For notes on the general eigenvalue problem, see *Numerical Recipes*[56]. The routine `eig` is the preferred routine for finding all the eigenfunctions of a matrix in MATLAB[57]. For a general matrix (non-Hermitian, non-tridiagonal), it uses a LAPACK algorithm based on singular value decomposition, called ZGGEV. See <http://www.netlib.org/lapack/lug/node36.html#1939>

Operator Method

There is a second method for solution of Eqn. (2.16a) and Eqn. (2.16b), which again can be found by analogy with the Schrödinger equation. We state that if the pseudo-hamiltonian operator is \hat{H} , then the time-evolution operator is $e^{\hat{H}\tau}$ (the phase is not zero). Then:

$$m_-(\zeta, \rho, \tau) = e^{(\hat{H}^{(z)} + \hat{H}^{(r)})\tau} m_-(\zeta, \rho, 0) \quad (2.32)$$

All that remains is to find the appropriate initial conditions, and then, the signal at any given time can be calculated. The operator method is numerically very efficient for finding a few points in time, when compared to the eigenfunction method. However, the computational load increases with the number of discrete times for which the magnetisation must be known.

In practice we exponentiate the matrices using a MATLAB in-built routine called `expm`. We can still separate the axial and radial variations, and combine after solving. The computational load is proportional to the number of time points required. Each matrix exponentiation itself uses of order N^2 operations. Creating spectra using operator-exponentiation is particularly time-consuming, since the FID must be calculated at many points (then Fourier transformed).

2.2.4 Testing the Computing

There are several tests that must be passed, to be certain the solutions are correct. Most importantly, we have compared the eigenvalues and eigenfunctions which result from the matrix method, with another method based on finite differencing: the *point-and-shoot* method.

More simply, we have checked that the solutions of the matrix eigenvalue equation are true eigenvectors, by straightforward evaluation. Also, the eigenvectors of the matrix have been seen to be orthogonal, as defined by Eqn. (A.9). There are cases where the eigenvalues are not numerically orthogonal, as dealt with in section 2.4.4. In such cases, one resorts to using the operator-exponentiation method.

Point and Shoot

The point-and-shoot method begins by converting Eqn. (2.16a) to a pair of coupled difference equations, to be evaluated at points separated by $\delta\zeta$. The time variation is assumed to be exponential with some constant ω_n . Here, we make use of the implicit Euler method for finite-differencing. The symbol ψ'_j represents the numerical first

derivative of ψ , evaluated at ζ_j .

$$j = 1..N; \quad \zeta_j = \frac{2j-2}{N-1} - 1; \quad \psi_j = \psi(\zeta_j)$$

$$\psi_{j+1} = \psi_j + \psi'_j \delta\zeta \tag{2.33a}$$

$$\psi'_{j+1} = \psi'_j + \left(\frac{\partial^2 \psi}{\partial \zeta^2} \right)_{j+1} \delta\zeta \tag{2.33b}$$

$$\left(\frac{\partial^2 \psi}{\partial \zeta^2} \right)_{j+1} = [\omega_n^{(z)} - i(b_1 \zeta_{j+1} + b_2 \zeta_{j+1}^2)] \psi_{j+1}$$

One boundary condition is imposed by setting $\psi'_1 = 0$. Without loss of generality, set $\psi_1 = 1$. The equation pair are solved for increasing j , i.e. from $\zeta = -1$. If the quantity $\omega_n^{(z)}$ is an eigenvalue of Eqn. (2.16a), then the other boundary condition will be satisfied: the final derivative will be zero, $\psi'_N = 0$.

The point-and-shoot method involves first choosing a trial eigenvalue (pointing) and then propagating from one boundary to the other (shooting). We then see how by much we have missed the target, change our aim accordingly, then re-iterate with an improved eigenvalue.

Suppose $\omega_n^{(z)}$ is not a true eigenvalue, merely an estimate. It is a complex quantity. The final boundary derivative is a complex function of $\omega_n^{(z)}$.

$$\omega_n^{(z)} = p + iq \qquad \psi'_N = f(p, q) + ig(p, q) \tag{2.34}$$

We find local partial derivatives of f and g with respect to p and q , by making small variations in $\omega_n^{(z)}$ in positive and negative directions. Then we make use of the Newton-Raphson method: our guess for the true eigenvalue is to be found by extrapolating using the first-order derivatives, so that the we move closer to where the functions f and g are zero:

$$\Lambda = \begin{pmatrix} \frac{\partial f}{\partial p} & \frac{\partial f}{\partial q} \\ \frac{\partial g}{\partial p} & \frac{\partial g}{\partial q} \end{pmatrix} \qquad \begin{pmatrix} \delta p \\ \delta q \end{pmatrix} = -\Lambda^{-1} \begin{pmatrix} f \\ g \end{pmatrix} \tag{2.35}$$

We increment our previous eigenvalue estimate by $\delta p + i\delta q$. We iterate the process until an acceptable approximation to an eigenvalue is found.

The radial eigenmodes can be found in a similar manner. The coupled equations

are:

$$j = 1..N; \quad \rho_j = \frac{j-1}{N-1}; \quad \phi_j = \phi(\rho_j)$$

$$\phi_{j+1} = \phi_j + \phi'_j \delta\rho \quad (2.36a)$$

$$\phi'_{j+1} = \phi'_j + \alpha^{-2} \left(\frac{1}{\rho} \frac{\partial}{\partial \rho} \left(\rho \frac{\partial \phi}{\partial \rho} \right) \right)_{j+1} \delta\rho \quad (2.36b)$$

$$\alpha^{-2} \left(\frac{1}{\rho} \frac{\partial}{\partial \rho} \left(\rho \frac{\partial \phi}{\partial \rho} \right) \right)_{j+1} = [\omega_n^{(r)} + i\alpha^2 \frac{b_2}{2} \rho_{j+1}^2] \psi_{j+1}$$

Iteration is from zero to unity. Again, the true eigenvalues are found by an iterative, Newton-Raphson method.

We compared the eigenvalues found using the point-and-shoot method with those from the matrix method. Agreement was to about 0.3% for eigenvalues, 1% for integrals of eigenfunctions; however, the point-and-shoot method is computationally much more demanding than the matrix method. Much user intervention is required, to find good starting estimates for eigenvalues, due to the difficulty of the complex-root finding problem.

Also, we should check that we have all the important eigenfunctions: we can be sure of reproducing spectra well, by ensuring that our set of eigenfunction is complete, in the mathematical sense of Appendix A, Eqn. (A.13). Mathematically, we require the sum of squares of the eigenfunction weights to be a good approximation to unity.

2.2.5 Some Eigenfunctions

Fig. 2.1(a) and (b) are facsimiles of figures 6a and 6c of Stoller, Happer and Dyson (1991)[58]. The field gradient is purely linear, transport purely diffusive: $b_1 = 400$; $b_2 = 0$; $\mu M_0 = 0$. The real parts of the eigenvalues correspond to the damping, the imaginary parts to frequency shifts. The low frequency eigenmode 2.1(a), is confined by both the wall and the field (equivalent to potential in the Schrödinger equation). The typical higher frequency eigenmode 2.1(b) is confined only by the walls, and has many more twists. Physically, more twists means greater $\nabla^2 m$, so more spin transport and more rapid decay. When only a linear gradient is present, the eigenfunctions can be described by Airy functions of suitable wave-number[59].

2.2.6 Some Eigenvalues

It is interesting to plot the eigenfrequencies of axial equation of motion in the Argand plane. Dividing the dimensionless eigenvalues, ω_n by the dimensionless gradient, b_1 ,

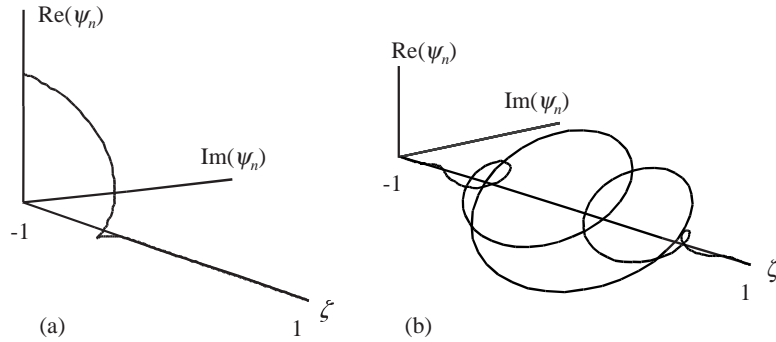


Figure 2.1: Two eigenfunctions of Eqn. (2.16a), with $b_1 = 400$ and $b_2 = 0$. (a) corresponds to the lowest eigenvalue $\omega_1 = 27.6 + 352i$. (b) corresponds to the 12th eigenvalue $\omega_{12} = 321$.

means that the real parts correspond to damping, the imaginary parts to frequency shifts. Also, $\pm i$ corresponds to the Larmor frequency at either boundary. Eigenmodes with frequency shifts outside the range ± 1 have very small amplitudes Eqn. (2.38), and so do not contribute to the spectrum (see next section, 2.3). They are localised only by the walls, not the field gradient. The forms of the eigenfunctions and eigenvalues are discussed further in Buu *et al* (2002, *Phys. Rev. B*) [59].

The presence of ‘branch points’[58], and the accompanying nearly degenerate eigenvalues and nearly linearly-dependent (non-orthogonal) eigenvectors may be related to some of the numerical problems discussed in Section 2.4.4. The examples (as in Ref. [59], Fig. 1) here have $|b_1| = 10^4$, $b_2 = 0$, with $\mu M_0 = 0, 1$ and 15 ((a), (b) and (c) respectively). The solutions are numerically more stable when the branch points are fewer in number, or pushed to the ends of the spectrum.

2.3 FIDs and Spectra

In this section, we turn our mathematical formalism into a simulation of the simplest NMR experiment one can perform: the Free Induction Decay (FID). We watch how the magnetisation evolves with time, and see what NMR signal is observed. We also look at the spectrum, the Fourier transform of the FID, which gives us more physical information.

2.3.1 Mathematical Formalism

We will idealise the FID experiment, by assuming that the both radio-frequency transmitter and receiver have uniform response over the cell, and the tipping angle is small, satisfying condition (2.2b): $m \ll M_0$. The magnetisation is therefore

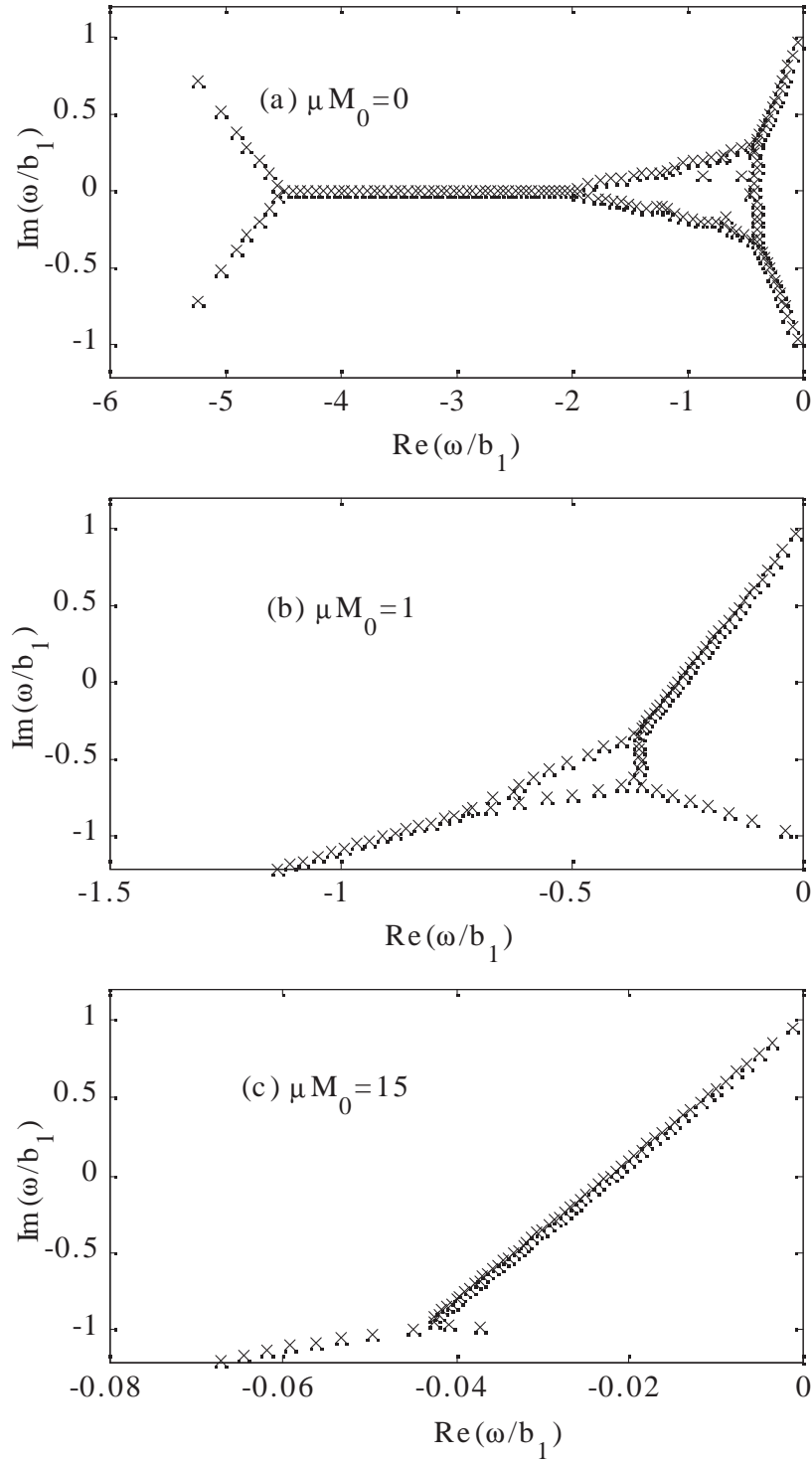


Figure 2.2: Eigenvalues of Eqn. (2.16a), with $|b_1| = 10^4$; $b_2 = 0$, solved with 150 basis functions. (a) with $\mu M_0 = 0$, (b) $\mu M_0 = 1$, (c) $\mu M_0 = 15$. ω_n/b_1 is the eigenfrequency. The real parts correspond to damping, the imaginary parts to frequency shifts.

uniform over the cell at a time chosen to be zero

$$m_-(\zeta, \rho, \tau = 0) = 1 \quad (2.37)$$

The amplitudes of the eigenfunctions would therefore be given by

$$a_n^{(z)} a_l^{(r)} = \iint \rho d\rho d\zeta \psi_n(\zeta) \phi_l(\rho) \times 1 \quad (2.38)$$

The signal received is the integral over the cell of m_- times a response function which we take to be uniform. Each eigenmode therefore has a weight, $c_n^{(z)}$ or $c_n^{(r)}$, which is equal to the corresponding amplitude when the excitation and response functions are equal. In the formalism of the previous section, using Eqn. (2.38), Eqn. (2.31) and Eqn. (A.12)[†]:

$$S_-(\tau) = \iint \rho d\rho d\zeta m_-(\zeta, \rho, \tau) \quad (2.39a)$$

$$= \left(\int_{-1}^1 d\zeta \sum_{\text{all } n} a_n^{(z)} \psi_n(\zeta) e^{\omega_n^{(z)} \tau} \right) \left(\int_0^1 \rho d\rho \sum_{\text{all } l} a_l^{(r)} \phi_l(\rho) e^{\omega_l^{(r)} \tau} \right) \quad (2.39b)$$

$$= \left(\sum_{\text{all } n} a_n^{(z)2} e^{\omega_n^{(z)} \tau} \right) \left(\sum_{\text{all } l} a_l^{(r)2} e^{\omega_l^{(r)} \tau} \right) \quad (2.39c)$$

The FID is often difficult to interpret, so instead we consider the spectrum, $\tilde{S}(\omega)$; the spectrum is the Fourier transform of $S(t)$, remembering that τ and t have different phases, as in Eqn. (2.15). Also the real-time eigenvalues (*eigenfrequencies*) are

$$\Omega_n = \omega_n \frac{D_\perp}{(1 + i\mu M_0)L^2} \quad (2.40)$$

The Fourier transform does not follow the text-book definition, as the integral is necessarily from $t = 0$, not $-\infty$.

$$\tilde{S}_-(\omega) = \int_0^\infty dt e^{-i\omega t} \left(\sum_{\text{all } n} a_n^{(z)2} e^{\omega_n^{(z)} \tau} \right) \left(\sum_{\text{all } l} a_l^{(r)2} e^{\omega_l^{(r)} \tau} \right) \quad (2.41a)$$

$$= - \sum_{\text{all } n, l} \frac{a_n^{(z)2} a_l^{(r)2}}{\Omega_n + \Omega_l - i\omega} \quad (2.41b)$$

More rigourously, the integral is a Laplace transform, with imaginary frequencies, instead of real decay rates.

[†]Please note the distinction between eigenfunction amplitudes, a_m , and weights, c_m . Each weight is defined by the integral over the cell of that eigenfunction multiplied by the response function of the receiver, which we take to be uniform. The amplitudes depend on the initial conditions, and are equal to the weights only for a free induction decay where the transmitter and receiver have identical response functions.

Therefore, to calculate the the signal, we need all the eigenvalues and all the eigenfunctions. We have taken the slightly risky step of trusting the eigenvalue problem to a black-box function: an inbuilt MATLAB routine, `eig`. We shall see later that perhaps our trust was mistaken. The axial and radial eigenvalue equations are solved separately, then the product of the results is taken. Solving two 1-D equations is computationally more efficient than solving one 2-D equation.

For each eigenvalue equation, a matrix is defined whose elements are calculated in the previous section, Eqn. (2.25) to Eqn. (2.28). The result of the calculation is a matrix, whose columns are the eigenvectors (eigenfunctions), and a vector whose elements are the corresponding eigenvalues. In the representation we have used, the integrals Eqn. (2.38) are given by the first elements of the eigenvectors. It is then a simple matter to calculate the spectrum or signal for range of frequencies or times. As we shall see later, it is possible to estimate the number of eigenmodes, and therefore how many basis functions will be required: Eqn. (2.44) and Eqn. (2.46).

2.3.2 Some FIDs

Some simulated Free Induction Decay signals are shown in figures Fig. 2.3 and Fig. 2.4. Time is in units of $|b_1|^{-2/3}$, for reasons which will become clearer later (section 2.4, Eqn. (2.53)).

Where there is no spin-rotation effect ($\mu M_0 = 0$), it is clear that increasing the field inhomogeneity (increasing b_1) shortens the time for which there is significant signal. Equivalently, increasing the spin-diffusion (decreasing b_1) also shortens the time, when we account for scaling the time axis by $D_{\perp}^{2/3}$. Where the spin-rotation effect is present, as in Fig. 2.4 ($\mu M_0 = 10$), the same overall scaling with gradient (b_1) is present. However, it is altered by long-lived signal and beats, pointing to the existence of Leggett-Rice spin-wave modes.

2.3.3 Some Spectra: Observing Eigenmodes

Some spectra are shown in Fig. 2.5 and Fig. 2.6. The first figure is for pure linear gradient ($b_2 = 0$). Start from $\mu M_0 = 0$: the spectrum is an image of the cell, with bumps at either end due to the restricted diffusion effect[60] (modes localised at the wall are less damped or have greater amplitude due to the asymmetry the wall imposes). As μM_0 is increased, peaks appear at the low-field (high frequency) end of the cell. The peaks correspond to standing-wave solutions of the Leggett-Rice equation, for minimum-field seeking magnetisation. Note that if μM_0 were negative, the spectrum would be reversed, i.e. peaks characteristic of high-field seeking modes

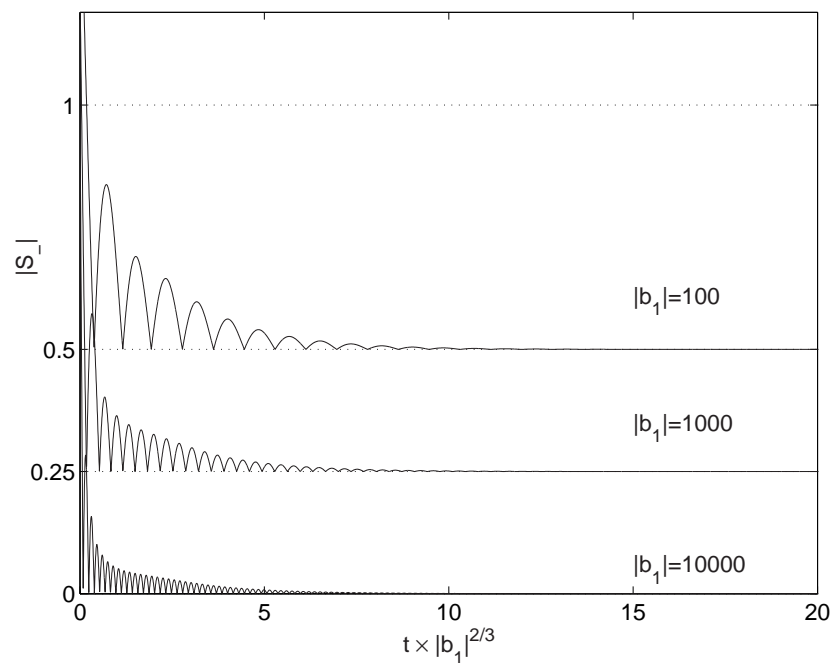


Figure 2.3: Example of Simulated FID: Absolute value of the signal, $S_-(t)$ is shown. Parameters in the simulation are: $\mu M_0 = 0, b_2 = 0$; b_1 is shown next to each signal; 150 axial basis functions were used. Signals are offset for vertically for clarity.

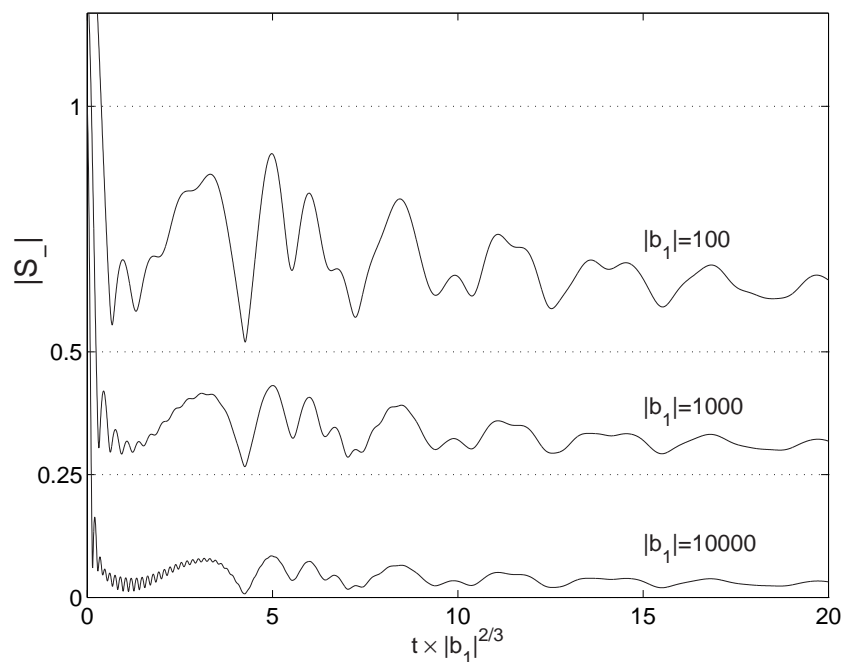


Figure 2.4: Example of Simulated FID: Absolute value of the signal, $S_-(t)$ is shown. Parameters in the simulation are: $\mu M_0 = 10, b_2 = 0$; b_1 is shown next to each signal; 150 axial basis functions were used. Signals are offset for vertically for clarity.

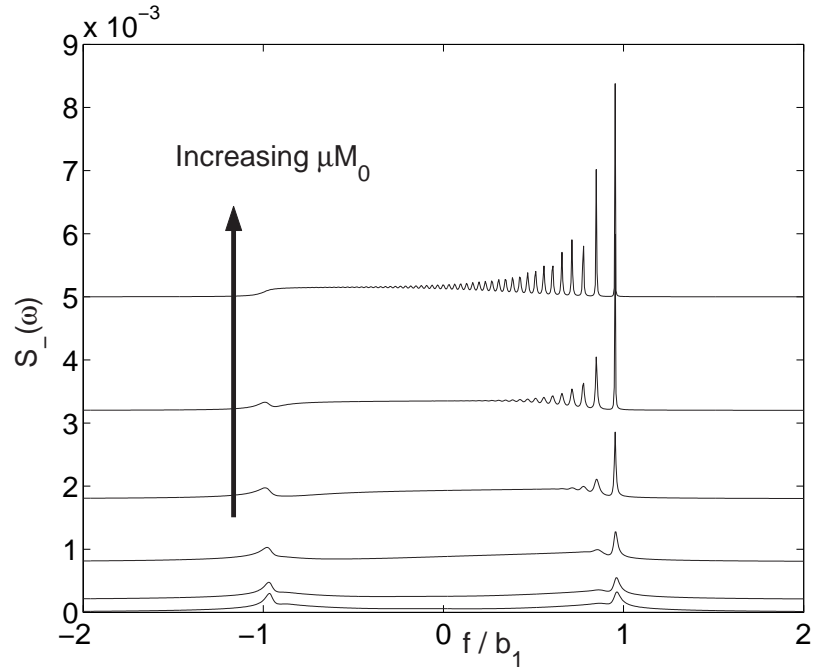


Figure 2.5: $\text{Re}(\tilde{S}(\omega))$ Absorption spectrum: $\alpha = 1; |b_1| = 10^4; b_2 = 0; \mu M_0 = 0.1, 0.3, 1, 3, 10, 30$. See the peaks appearing as μM_0 increases, with a characteristic inter-peak frequency split.

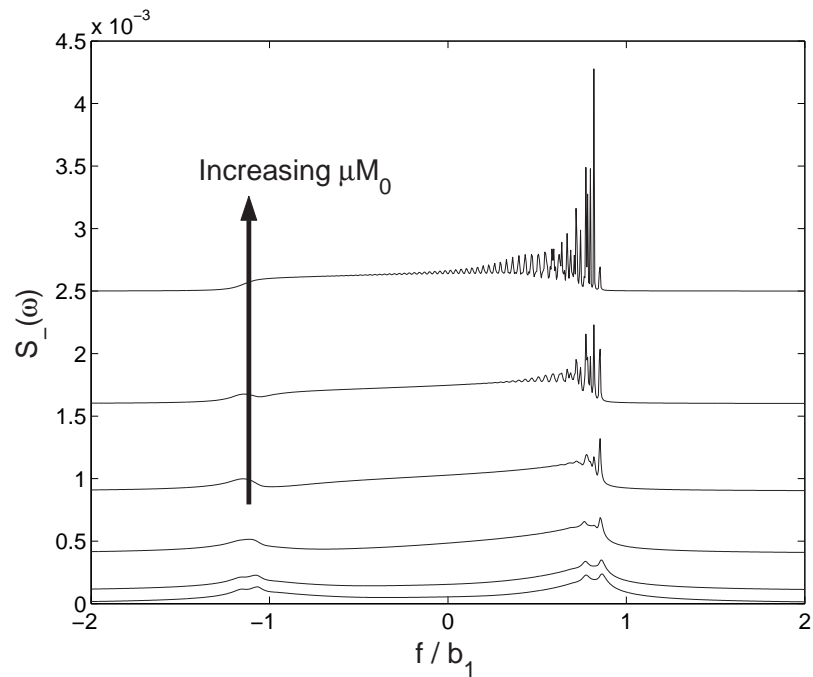


Figure 2.6: $\text{Re}(\tilde{S}(\omega))$ Absorption spectrum: $\alpha = 1; |b_1| = 10^4; b_2 = 0.2b_1; \mu M_0 = 0.1, 0.3, 1, 3, 10, 30$. The radial field inhomogeneity breaks a degeneracy, so there are many more peaks than in Fig. 2.5.

would appear on the left of the spectrum (low-frequency). As μM_0 increases, so the widths of the peaks (damping of the eigenmodes) decrease.

It is useful to define the following frequency scales:

$$\omega_{G_1} = \gamma G_1 L \quad \omega_D = D_{\text{eff}}/L^2 \quad (2.42)$$

Note that the spin-transport frequency, ω_D , is complex. The first order gradient frequency, ω_{G_1} , corresponds to half the field-inhomogeneity (when there is no second order gradient). The ratio of the two is equal to the dimensionless first order gradient: $\omega_{G_1}/\omega_D = b_1$.

The peaks in the spectrum are separated by a characteristic frequency shift from one peak to the next. We can find the separation by taking the only cell-length independent combination of the two frequencies:

$$\Delta\omega = \omega_{G_1}^{2/3} |\omega_D|^{1/3} \quad (2.43)$$

Take note of the normalisation of the frequency axis in figures Fig. 2.5 and Fig. 2.6, and the separation of the peaks.

If we divide the total field inhomogeneity, $2\omega_{G_1}$, by $\Delta\omega$ we find that there are approximately

$$N_z \simeq 2\omega_{G_1}/\Delta\omega = 2|b_1|^{1/3} \quad (\text{Spin-wave modes}) \quad (2.44)$$

spin-wave modes confined by the end walls of the cell. Eqn. (2.44) does not take account of the second order gradient, especially the radial field variation. We need at least as many axial basis functions as there are spin-wave modes to accurately calculate the spin-dynamics, and preferably three times as many

$$N_z \geq 6|b_1|^{1/3} \quad (\text{Basis Set}) \quad (2.45)$$

The requirement can be confirmed by increasing the number of basis functions used until the eigenvalues converge (pre-factor ~ 6), or until the spectrum for μM_0 looks smooth (pre-factor ~ 3). The value $b_1 = 10^4$ is experimentally achievable (see Buu *et al*(2002, *Phys. Rev. B*)[53]). It should be noted that spectra very much like these have been calculated for spheres[61] and cubes[37]. The spectra for a cube and a cylinder, in a purely linear gradient, along symmetry axis, are identical.

The second order gradient b_2 breaks a symmetry, therefore it breaks a degeneracy. Each axial eigenmode has a family of radial sub-modes; each peak in Fig. 2.5 is convolved with a radial spectrum. When μM_0 is large, the spectrum can have a great number of overlapping peaks. When μM_0 is zero (classical spin-diffusion)

the lineshape is distorted; it is still an image of the cell, but in the presence of a non-uniform frequency distribution. End effects due to restricted diffusion are also present. The current work represents an advancement over previous calculations because the theory has been extended to include radial variations, i.e. second order gradients.

We can repeat the analysis of the number of basis functions required, now for the radial basis set. The second order gradient frequency scale is: $\omega_{G_2} = \gamma G_2 L^2$, so the radial field-inhomogeneity is $\frac{1}{2}\alpha^2\omega_{G_2}$. The combination of frequencies which is independent of length is $\Delta\omega_2 = \omega_{G_2}^{1/2}|\omega_D|^{1/2}$. Therefore the number of radial modes is expected to be:

$$N_r \simeq \frac{1}{2}\alpha^2\omega_{G_2}/\Delta\omega_2 = \frac{1}{2}\alpha^2|b_2|^{1/2} \quad (\text{Spin-wave modes}) \quad (2.46)$$

We would like to have a basis set larger than the number of modes by a factor of about three.

2.4 Spin-Echoes

The major contribution we have made to the understanding of the Leggett-Rice equation Eqn. (2.1) is the calculation of spin-echoes in the linear approximation, Eqn. (2.2) and Eqn. (2.8). The non-linear equation has been solved for linear-field gradients in 1D by V.V. Dmitriev *et al*[51] (see also later, non-linear effects, 3.4.2), but the simulation uses a lot of computational power. Applying the matrix representation of the linearised equation Eqn. (2.8) to spin-echoes requires a detailed knowledge of the properties of the equation of motion (Appendix A).

2.4.1 Formalism

A spin echo is formed by applying two RF-pulses parallel to the x -axis, separated by time t_w . The first pulse at (time zero) is the tipping pulse (causing the magnetisation to rotate through a small angle θ); the second pulse is the π -pulse (causing a 180° inversion of the magnetisation). Classically, the magnetisation precesses at a rate depending on the local field, causing the signal to decay (de-phasing); the pulse reverses the de-phasing, and then the magnetisation continues to precess, reversing the inverted de-phasing (re-phasing). Thus an echo is formed time t_w after the π -pulse.

From the point of view of the linearised equation of motion, Eqn. (2.8), the π -pulse changes the sign of μM_0 , complex conjugates the magnetisation m_- , and

alters the gradient coefficients in the equations of motion, Eqn. (2.16a) and Eqn. (2.16b):

$$m_-(\mathbf{r}, \tau_w^<) \rightarrow m_-(\mathbf{r}, \tau_w^>) = m_-^*(\mathbf{r}, \tau_w^<) \quad (2.47a)$$

$$\mu M_0 \rightarrow -\mu M_0 \quad b_1 \rightarrow b_1^* \quad b_2 \rightarrow b_2^* \quad (2.47b)$$

Of course, the eigenfunctions after the pulse are different from those before, unless $\mu M_0=0$.

We calculate the motion up to $\tau_w^<$ in terms of eigenfunctions before the π -pulse, as in Eqn. (2.31), perform the π -pulse operation, then convert to a sum over post- π -pulse eigenfunctions. For simplicity of notation, combine axial and radial eigenfunctions.

$$\begin{aligned} m_-(\zeta, \rho, \tau_w^>) &= \sum_{\text{all } m} a_m^{*<} \Psi_m^{*<}(\zeta, \rho) e^{\omega_m^{*<} \tau_w} \\ &= \sum_{\text{all } m} a_m^> \Psi_m^>(\zeta, \rho) e^{\omega_m^> \tau_w} \end{aligned} \quad (2.48)$$

Here, the $>$ and $<$ superscripts refer to ‘before’ and ‘after’ the π -pulse.

The initial amplitudes $a_m^<$ are calculated as in Eqn. (2.38). However, the amplitudes after the pulse, $a_m^>$ are different. They are found by pre-multiplying the n^{th} term by $\Psi_m^>$ and integrating:

$$a_m^> = \sum_n c_n^{*<} U_{nm} e^{\omega_n^{*<} \tau_w} \quad (2.49a)$$

$$U_{nm} = \iint \rho d\rho d\zeta \Psi_m^>(\zeta, \rho) \Psi_n^{*<}(\zeta, \rho) \quad (2.49b)$$

The matrix whose elements are U_{mn} is called the *overlap matrix*.

The observed signal after the second pulse is:

$$S(\tau > \tau_w) = \sum_{\text{all } m} a_m^> c_m^> e^{\omega_m^> (\tau - \tau_w)} \quad (2.50)$$

In classical NMR one expects an echo where $\tau = 2\tau_w$. Substituting Eqn. (2.49a) into Eqn. (2.50) at the expected echo-time gives:

$$S(2\tau_w) = \sum_{\text{all } m} \sum_{\text{all } n} c_n^{*<} U_{nm} c_m^> e^{(\omega_m^> + \omega_n^{*<}) \tau_w} \quad (2.51)$$

When there is a linear field gradient, $\Psi_n(\zeta, \rho) = \psi(\zeta)$ has symmetry about $\zeta = 0$. As a consequence, the pre- and post- π -pulse eigenmodes are related through:

$$\psi_m^>(\zeta) = \psi_m^{*<}(-\zeta) \quad c_m^> = c_m^{*<} \quad \omega_m^> = \omega_m^{*<} \quad (2.52)$$

One can see why the signal will refocus at $2\tau_w$: the various phase factors (imaginary parts of the eigenvalues) in Eqn. (2.50) will cancel; the eigenmodes are in phase at the echo. The amplitude will have decreased due to diffusive decay (described by the real parts of the eigenvalues). The phase of $S(2\tau_w)$ will not in general be π as predicted classically, but will depend upon spin-rotation and the overlap matrix, U_{nm} .

The symmetry, Eqn. (2.52), is broken if $b_2 \neq 0$. For small b_2 the effect is perturbative: small changes in phase and amplitude of echo. Also, we might expect the echo to refocus at a different time, because the frequency separations between the eigenmodes depend on the second order gradient, and whether it represents a maximum or minimum in the potential part of the pseudo-hamiltonian. Thus, there is a mismatch in timing of defocussing and refocussing, which would not occur if there were no spin-rotation.

2.4.2 Results in Time and Space

A few example results are presented, showing the amplitude of the signal as a function of time. Also, two plots of the magnetisation as a function of both space and time are shown for spin-echo simulations.

There is a characteristic timescale for attenuation of the echo signal, which is found using the Leggett-type analysis[26] of 1.3.3, Eqn. (1.24)(a and b). In the dimensionless units of Eqn. (2.15), the equation becomes

$$\ln |S(2\tau_w)| = -\frac{2}{3} \frac{|b_1|^2}{(1 + \mu M_0)^{1/2}} |\tau_w|^3 \quad (2.53)$$

We therefore take our natural units of time to be $|b_1|^{-2/3}$.

Time

In both Fig. 2.7 and Fig. 2.8 the π -pulse is at $\tau|b_1|^{2/3} = 2$ after the initial pulse. For numerical reasons (see 2.4.4) $\mu M_0 = 0$ is not shown in Fig. 2.8, but the operator method could have been used for that calculation.

When $b_2 = 0$ (Fig. 2.7, middle curve) the echo is at the expected time, $\tau|b_1|^{2/3} = 4$. When the product $\mu M_0 \times (b_2/b_1)$ is positive (Fig. 2.7 and Fig. 2.8, lower curves), the echo is delayed, attenuated and distorted. The opposite is true when $\mu M_0 \times (b_2/b_1) < 0$: the echo is advanced and enhanced. The shift in the time of echo formation is very unusual in NMR spin-echo experiments.

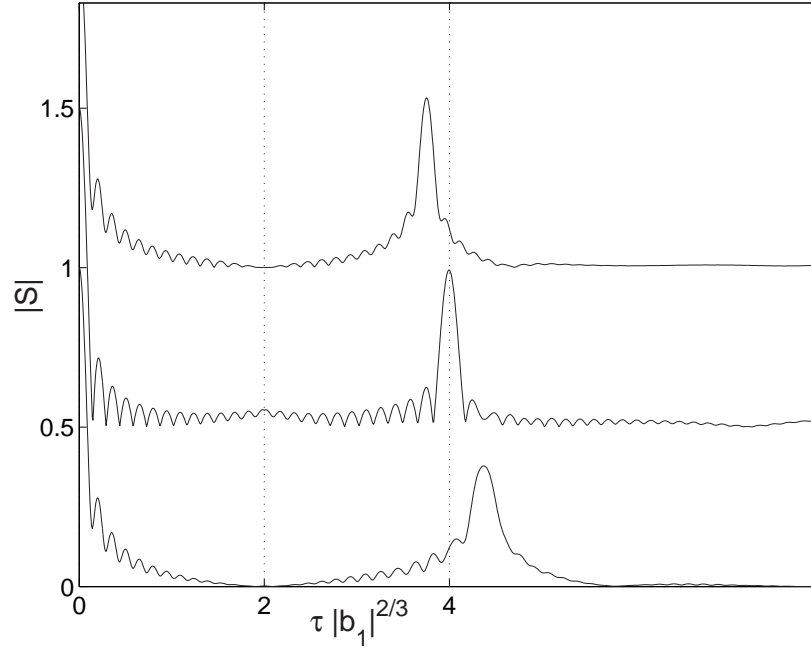


Figure 2.7: Magnitude of the signal in simulated echo experiments, for: $\alpha = 1$; $|b_1| = 10^4$; $\mu M_0 = 10$; $N_z = 150$; $N_r = 30$. From top down, $b_2/b_1 = -0.3, 0, +0.3$. Signals are shifted by $+1$ and $+0.5$ for clarity. Relative delay or advancement of the echo depends on the relative signs of second order gradient and spin-rotation parameter.

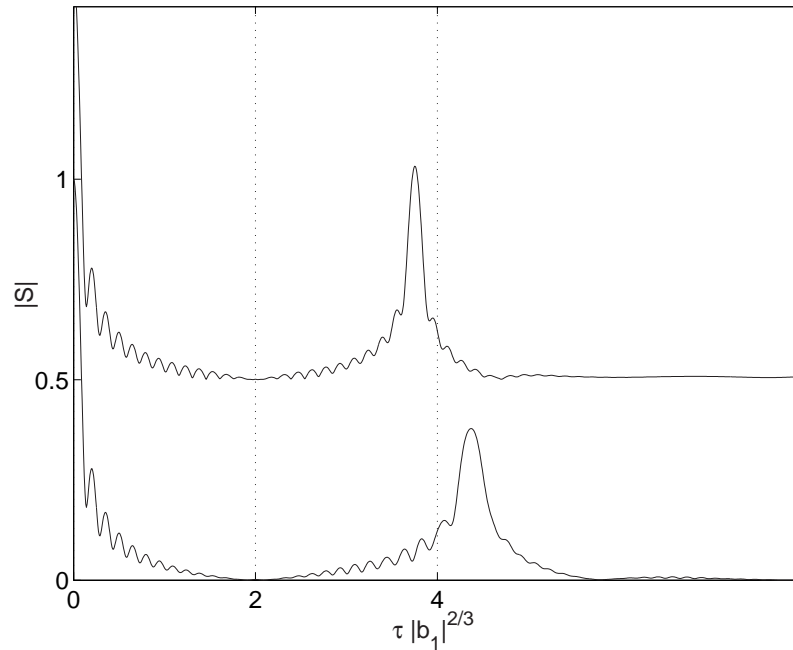


Figure 2.8: Magnitude of the signal in simulated echo experiments, for: $\alpha = 1$; $|b_1| = 10^4$; $b_2/b_1 = 0.3$; $N_z = 150$; $N_r = 30$. Lower curve: $\mu M_0 = 10$. Upper Curve: $\mu M_0 = -10$, shifted up by 0.5 for clarity.

Space and Time

Some physical intuition about spin-transport can be gained by plotting the variation of magnetisation in space as well as time. First, look at Fig. 2.9, calculated with the same parameters as Fig. 2.7, middle curve. The initial magnetisation is uniform, then the signal decays rapidly, because the phase is changing non-uniformly. There is clearly significant spin-transport towards $\zeta = -1$ before the π -pulse. The magnetisation is minimum-field seeking. Magnetisation is reflected from the wall, resulting in an interference pattern with local variations in magnitude of m_- : the phase is also varying rapidly.

The π -pulse is after 2 units of time. There is a reversal of motion, since μM_0 has been reversed, the magnetisation is now maximum-field seeking. Much stronger interference is observed, originating from the $\zeta = -1$ wall. When the echo occurs it is attenuated by the diffusive losses of transverse magnetisation, driven by field gradients; the loss is strongly influenced by the presence of the lower wall, but not by the upper wall.

The second colour plot, Fig. 2.10 is for a smaller cell (by a factor of $10^{1/3}$) and greater spin-rotation effect ($\mu M_0 = 100$). The boundaries have a greater influence, so the echo more is distorted. Also, the wave-like character of the spin-motion is more dominant. Between 6 and 8 time units, the waves can be seen to reflect from the top wall.

Characteristics of Free Space Motion

In Fig. 2.10 there appears to be a characteristic spin-wave velocity:

$$\frac{1}{|b_1|^{2/3}} \frac{d\zeta}{d\tau} \simeq 0.5 \quad (2.54)$$

For Fig. 2.9, the velocity would seem to be a little lower, perhaps 0.25 in the same units.

As an aside, we can derive an approximate expression for the characteristic velocity. We assume that the velocity depends only on γG_1 and $D_{\text{eff}} = D_{\perp}/(1 + i\mu M_0)$, i.e the waves are travelling in free space. Excluding pre-factors, dimensional analysis tells us:

$$v_C = \frac{dz}{dt} \sim (\gamma G_1)^{1/3} D_{\text{eff}}^{2/3} \quad (2.55a)$$

$$\nu_C = \frac{d\zeta}{d\tau} \sim |b_1|^{1/3} \Rightarrow \frac{1}{|b_1|^{2/3}} \frac{d\zeta}{d\tau} \sim |b_1|^{-1/3} \quad (2.55b)$$

We can now see why the velocity in Fig. 2.10 is about twice that of Fig. 2.9: a factor of about $10^{1/3}$.

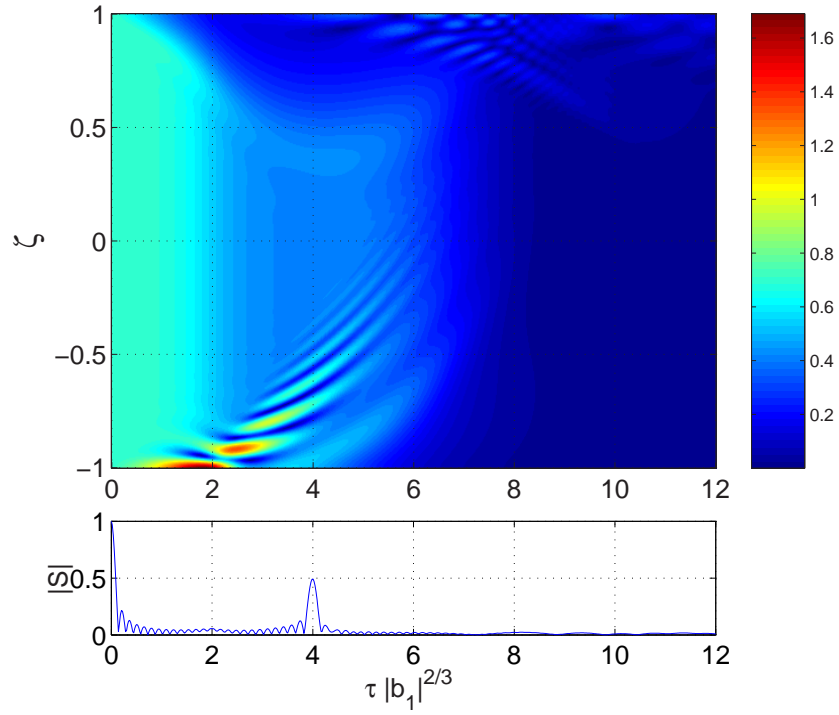


Figure 2.9: Magnitude of magnetisation as a function of axial position, ζ and time, in characteristic units, $\tau|b_1|^{2/3}$: $b_2 = 0$; $|b_1| = 10^4$; $\mu M_0 = 10$; $N_z = 150$. Axial variations only.

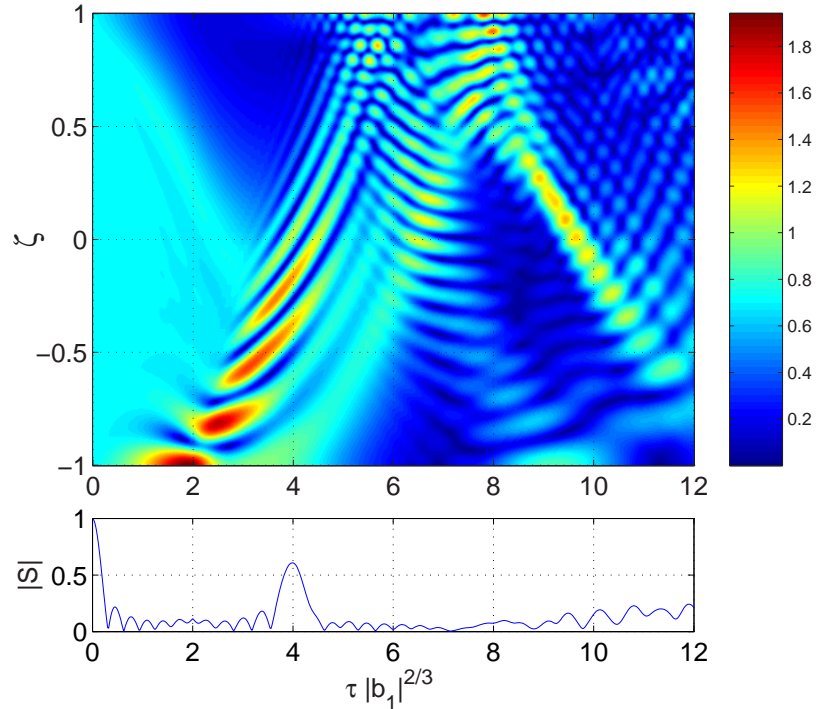


Figure 2.10: Magnitude of magnetisation as a function of axial position, ζ and time, in characteristic units, $\tau|b_1|^{2/3}$: $b_2 = 0$; $|b_1| = 10^3$; $\mu M_0 = 100$; $N_z = 150$. Axial variations only. Note the interference patterns produced by reflections from the walls.

Furthermore we can derive characteristic free space wavenumber and frequency:

$$k_C \sim (\gamma G_1)^{1/3} D_{\text{eff}}^{-1/3} \Rightarrow \kappa_C = k_C/L \sim |b_1|^{1/3} \quad (2.56a)$$

$$\Omega_C \sim (\gamma G_1)^{2/3} D_{\text{eff}}^{1/3} \Rightarrow \omega_C = \Omega_C L^2/D_{\text{eff}} \sim |b_1|^{2/3} \quad (2.56b)$$

Of course $v_C = \Omega_C/k_C$ and $\nu_C = \omega_C/\kappa_C = |b_1|^{1/3}$, as expected. Ω_C turns out to be the same as the spin-wave mode separation, $\Delta\omega$, Eqn. (2.43).

2.4.3 Analysis of Results

In free space, Torrey[33] showed that the magnetisation decays exponentially with the cube of the waiting time, Eqn. (1.21). The result derived by Leggett[26] is the same, with the diffusion coefficient altered by the presence of spin-rotation. Furthermore, Leggett predicted that spin-rotation would lead to variation in the phase of the echo. Amplitude and phase are experimentally measurable quantities.

For comparison with real experimental results (Chapter 3, section 3.5.2, page 80 and after) it is convenient to define the parameter

$$b_L = \frac{\gamma G_1 L^3 \mu M_0}{D_{\perp}} \quad b_L = \lim_{\tau_{\perp} \rightarrow \infty} b_1(\tau_{\perp}) \quad (2.57)$$

We use the quantity b_L assuming D_{\perp} and μM_0 are proportional to τ_{\perp} , and that b_L is the extreme low-temperature, extrapolated value of the dimensionless first order gradient b_1 (2.15d). Where μM_0 varies, it is interesting to keep b_L constant. For example, when $\mu M_0 = 10$; $|b_1|/b_L = 1.005$. Let us see what our theory predicts.

Varying b_L

One of the approximations Leggett made was that the experimental region was unbounded, which is equivalent to our dimensionless gradient, b_L , being infinite. In Fig. 2.11 we can see the effect of finite cell size (finite b_L). The two plots are log of amplitude at the echo (local signal maximum) as a function of the cube of time (in characteristic units); and phase as a function of log amplitude. The phase can be greater than 2π ; the trick is to know when to add extra 2π s to the phase, so that phase is a continuous, monotonically increasing function. When μM_0 is very large and the points spaced far apart, more than one complete cycle may need to be added. For the results presented in this chapter, there are no phase increments greater than 2π , but there may be some such increments in the experimental results, in the next chapter.

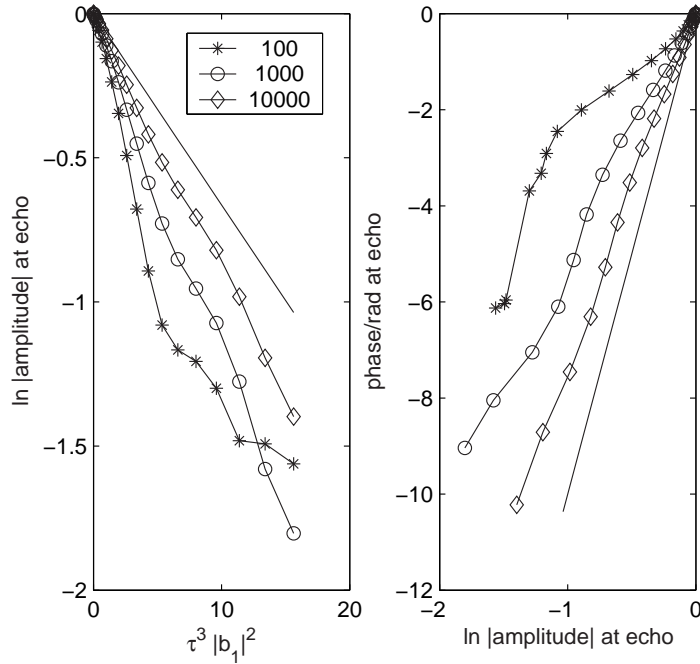


Figure 2.11: Echo analysis, varying b_L : $b_2 = 0$; $\mu M_0 = 10$; $N_z = 150$. The straight lines are predictions of Leggett's unbounded-cell formulae; deviation is greatest where the cell (and b_L) are smallest. b_L is shown in the legend.

The straight lines show the infinite-cell predictions of Leggett. Note the increasing deviations as the effective cell size is decreased, b_L is decreased. The echoes consistently suffer extra attenuation due to the presence of the boundaries. Also, the results are not simple straight lines, so any analysis based on Leggett's formula must take into account the effects of the finite size of the experimental cell (see Chapter 3, Section 3.5).

Varying μM_0

Since Leggett predicted that the phase should vary in proportion to μM_0 , phase is normalised by μM_0 in Fig. 2.12. Also the time axis is normalised by $(1 + \mu M_0^2)^{-1/2}$ (see Eqn. (2.53)). Note again the deviation from Eqn. (2.53); more deviation as μM_0 is increased. Of particular interest is that the slope of phase, $\arg(S(2\tau_w))$, versus log amplitude, $\ln |S(2\tau_w)|$, stops increasing with increasing μM_0 .

The slope of such a graph is called $\mu M_0(\text{measured})$, and the value of μM_0 in the simulation $\mu M_0(\text{input})$, and the results are plotted in Fig. 2.13. The value of $\mu M_0(\text{measured})$ depends on the other dimensionless parameters, b_1 and b_2 , as well as $\mu M_0(\text{input})$. Smaller b_1 means greater deviation from the ideal. An approximate

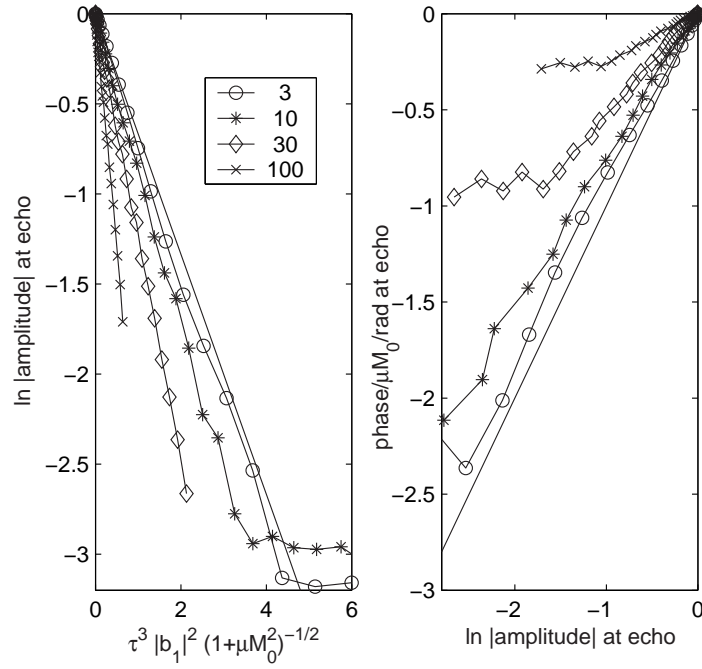


Figure 2.12: Echo Analysis, varying μM_0 : $b_L = 10^4$; $b_2 = 0$; $N_z = 150$. μM_0 is in the legend. The straight lines are predictions of Leggett's unbounded-cell formulae; deviation is greatest when μM_0 is greatest.

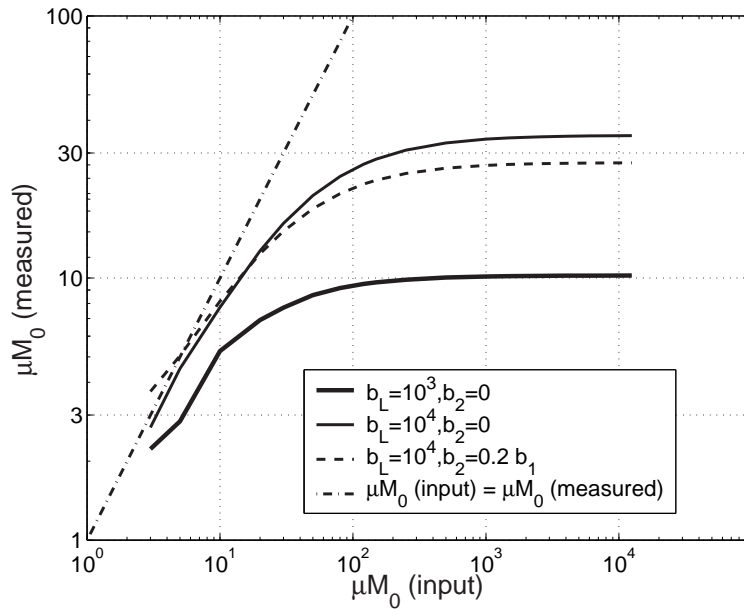


Figure 2.13: The value of the spin-rotation parameter which would be observed, as a function of the spin-rotation parameter input to the model. $\mu M_0(\text{measured})$ values are derived from the results of linear-fitting of log-amplitude versus phase, when log-amplitude $\gtrsim -2$. Numbers of basis functions used: $N_z = 6|b_1|^{1/3}$; $N_r = |b_2|^{1/2} + 2$.

value for the saturation value of μM_0 (measured) as μM_0 (input) $\rightarrow \infty$ is $0.3b_L^{1/2}$ (see Fig.7b in Ref. [59]), when b_2 is zero. It is not possible to measure arbitrarily large μM_0 .

Varying b_2/b_1 : Delayed Echoes

Few people have included inhomogeneous field gradients in their analysis of restricted spin-diffusion. The problem can be treated semi-analytically, for classical spin-diffusion, neglecting the radial variation (see Le Doussal and Sen[62]). However, the second order gradient introduces the second dimension, ρ into the problem. Symmetry is broken in both radial and axial directions. Therefore, a numerical simulation is of use.

Fig. 2.14 shows the two Leggett-Rice type plots (log-amplitude versus time-cubed, and phase versus log-amplitude) and the fractional delay of the echo. The fractional delay is defined by

$$\delta\tau/\tau_w = \frac{\tau_{\text{echo}} - 2\tau_w}{\tau_w} \quad (2.58)$$

where τ_{echo} is the time of the maximum, post- π -pulse signal: $\delta\tau$ and is positive for delayed echoes, negative for advanced. One might hope that the fractional delay would be independent of the waiting time, τ_w , for given parameters, but it is not.

When $b_2/b_1 > 0.5$ there is an absolute minimum of field along the axis, causing severe distortion of the echo; as can be witnessed by the results for $b_2 = 0.6b_1$ in Fig. 2.14. The particular set of parameters shown mean that the echo is delayed, at least while the echo is reasonably well formed. Reversing the sign of b_2 reverses the sign of delay (see also Fig. 2.7). Furthermore, the results of a Leggett-Rice type analysis depend on the sign of the second-order field variation. Small negative b_2 leads surprisingly to an enhancement of the echo, as well as advancement.

The delay depends not only upon the second-order field variation, but also varies with b_1 and μM_0 (Fig. 2.15). Look at the second of the two figures, wherein μM_0 is changed: the points unexpectedly fall on just two curves for quite a long time, at least two characteristic units. There is one curve for positive μM_0 (advanced), one for negative (delayed). It appears there is some kind of simple scaling law for the echo mistiming as a function of the inter-pulse waiting time. The delay looks to be proportional to the second order gradient in some sense, and to scale in time with the first order gradient and spin-rotation parameter, in accordance with Fig. 2.15.

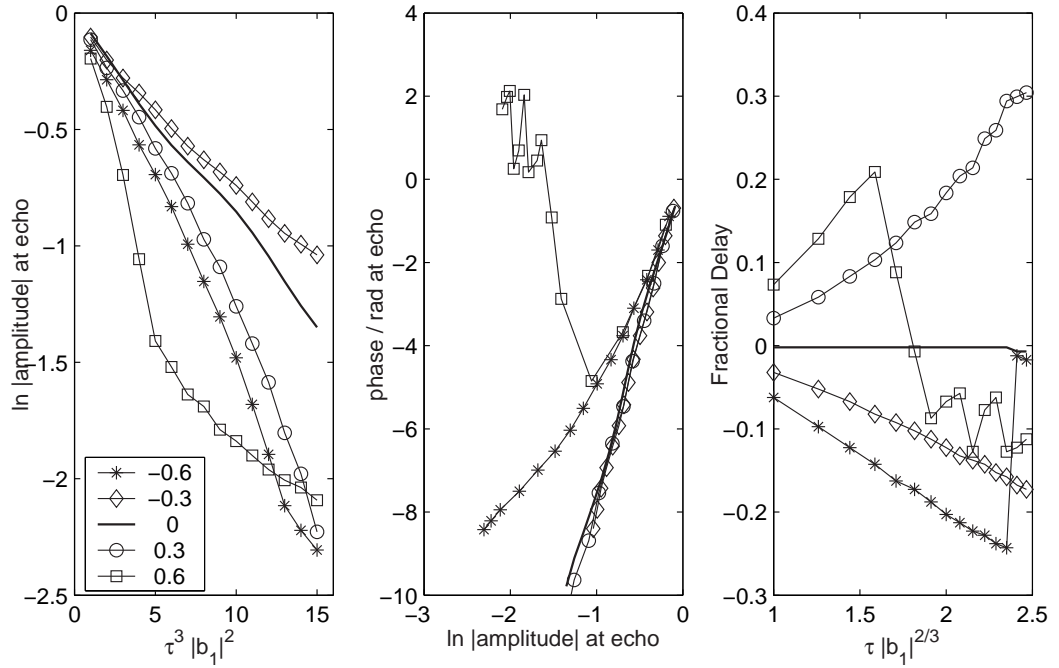


Figure 2.14: Echo Analysis, varying b_2/b_1 : $b_L = 10^4$; $\mu M_0 = 10$; $N_z = 150$, $N_r = 50$. b_2/b_1 is in the legend. The delays depend on the sign and magnitude of the second order gradient.

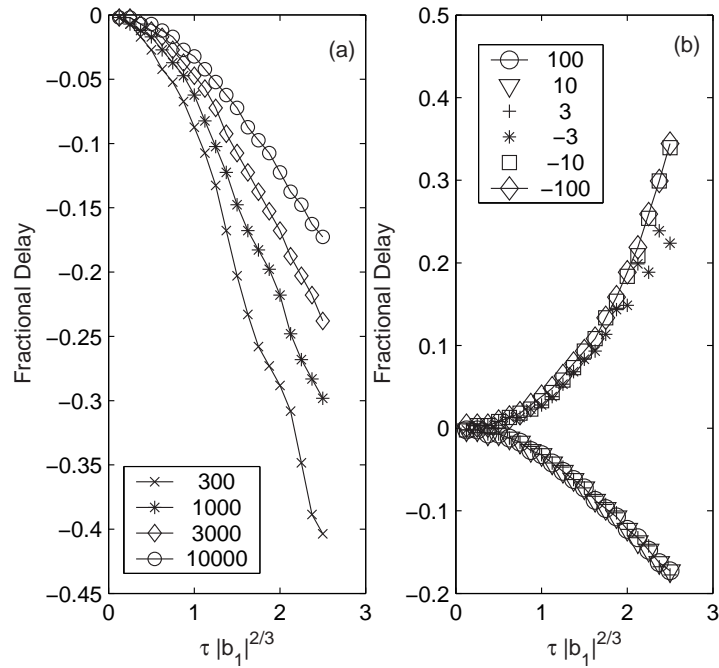


Figure 2.15: Fractional echo delay as a function of time. Plot(a): Various b_L , $\mu M_0 = 10$. Plot(b): Various μM_0 , $b_L = 10^4$. Note the scaling of the delays in (b). For both plots $b_2/b_1 = -0.3$; 150 axial and 50 radial basis functions used.

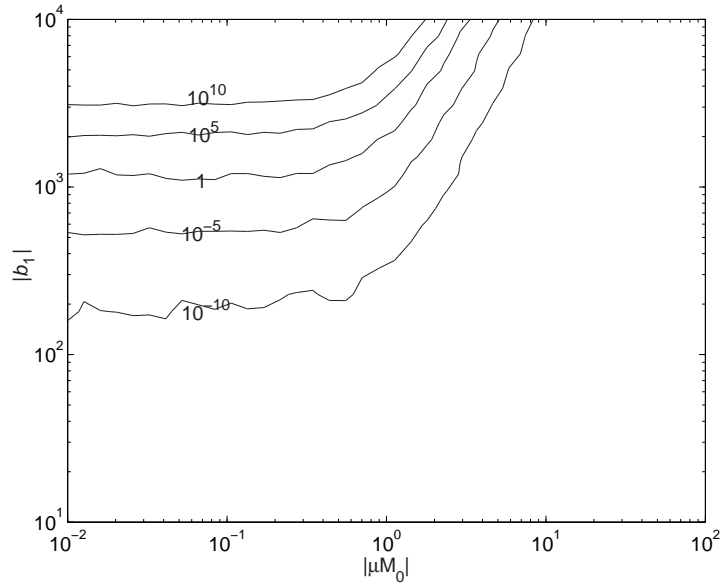


Figure 2.16: Numerical violation of axial eigenfunction orthogonality. $N_z = 100$. See Eqn. (2.59a) for definition. Original figure prepared by Olivier Buu.

2.4.4 Numerical Problems

The eigenfunction method is preferred for solving the equations of motion, for reasons of computational efficiency (see page 34). The numerical eigenvector solutions of the axial eigenvalue equation, Eqn. (2.30) are not always orthogonal, as required by Eqn. (A.9), although they are always good eigenvectors with the relevant associated eigenvalues. The eigenfunctions of the radial pseudo-hamiltonian matrix are orthogonal to approximately machine floating-point precision.

The violation of orthogonality is most easily defined by:

$$\int_{-1}^{+1} d\zeta \psi_m(\zeta)\psi_n(\zeta) = [F]_{mn} \quad (2.59a)$$

$$\|F - I\| \neq 0 \quad (2.59b)$$

Fig. 2.16 shows contours of the value of the function $\|F - I\|$ (where I is the identity matrix): the norm of the difference between eigenvector inner-products and the identity matrix. The eigenfunctions were found to be true eigenfunctions of the Hamiltonian matrix, to a few times floating point precision, despite their non-orthogonality. The orthogonality violation is worst when $|b_1| \gtrsim 500$, $|\mu M_0| \lesssim 2$.

It is not clear whether the numerical problem is due to the MATLAB routine `eig`, and specifically the normalisation it uses (see footnote on page 34), or whether the numerical problem is intrinsic to the problem of degenerate eigenvalues and branch-points as detailed by Stoller *et al*[58]. The outputs from `eig` are normalised in a

Hermitian conjugate way (as for solutions of Schrödinger's equation), which is not what we need (see Eqn. (A.10)).

The numerical errors cause incorrect evaluation of the eigenfunction overlap matrix Eqn. (2.49b), which in turn means discontinuities at the π -pulse, in echo simulations. Therefore where orthogonality is strongly violated, one must use the operator-exponentiation method instead. There is no such problem for calculating the spectra, since the eigenvalues are known to be accurate, and we explicitly normalise the eigenfunctions according to Eqn. (A.10).

2.5 Solution for a Sphere

The same process we used to calculate spin-dynamics in a cylinder can also be applied to a sphere. The equation of motion in the obvious co-ordinates is non-separable. The boundary conditions are of course different, so we must use a different basis set.

2.5.1 Equation of Motion

The co-ordinates used are, unsurprisingly, spherical polar with polar angle taken relative to the applied field. We take the field variation direct from Eqn. (2.11). The boundary condition for a sphere of radius R is:

$$\left. \frac{\partial m_-(r, \theta)}{\partial r} \right|_{r=0, R} = 0 \quad (2.60)$$

ensuring that there are no spin-sources or sinks at either the wall or the origin of co-ordinates. Again the symmetry in φ reduces the problem to two dimensions. In spherical polar co-ordinates, the equation of motion is non-separable, even when only the first order gradient is considered.

Dimensionless units are defined much as before:

$$\rho = r/R; \quad 0 \leq \rho \leq 1; \quad 0 \leq \theta \leq \pi \quad (2.61a)$$

$$\tau = tD_{\text{eff}}/R^2 \quad (2.61b)$$

$$b_1 = \gamma G_1 R^3 / D_{\text{eff}}; \quad b_2 = \gamma G_2 R^4 / D_{\text{eff}} \quad (2.61c)$$

The dimensionless equation of motion is

$$\begin{aligned} \frac{\partial m_-(\rho, \theta, \tau)}{\partial \tau} = & \frac{1}{\rho^2} \left\{ \frac{\partial}{\partial \rho} \left(\rho^2 \frac{\partial}{\partial \rho} \right) + \frac{1}{\sin \theta} \frac{\partial}{\partial \theta} \left(\sin \theta \frac{\partial}{\partial \theta} \right) \right\} m_- \\ & - i \left\{ b_1 \rho \cos \theta + \frac{1}{2} b_2 \rho^2 (3 \cos^2 \theta - 1) \right\} m_- \end{aligned} \quad (2.61d)$$

2.5.2 Basis Set

The basis functions ϕ_{nl} are solutions of the homogeneous equation which satisfy the boundary condition Eqn. (2.60):

$$(\nabla^2 + \kappa_{nl}^2)\phi_{nl} = 0 \quad (2.62a)$$

$$\phi_{nl} = \Xi_{nl} P_l^0(\cos \theta) j_l(\kappa_{nl}\rho) \quad (2.62b)$$

The subscripts n and l label radial and angular functions respectively, paying homage to the quantum mechanics of a hydrogen atom. The numbers κ_{nl} must be found numerically. It is easy to show from Eqn. (2.62a) and Eqn. (2.60), using the divergence theorem, that the basis functions must be orthogonal, if they correspond to different κ_{nl} . The P_l^0 are the Legendre polynomials, and the j_l are the spherical Bessel functions[†]. The Ξ_{nl} are normalisation factors, defined much as in Eqn. (2.21):

$$\Xi_{nl} = \left(\int_0^1 \rho^2 d\rho j_l^2(\kappa_{nl}\rho) \right)^{-1/2} \quad (2.63)$$

$$\Xi_{nl} = \frac{\kappa_{nl}}{j_l(\kappa_{nl})} \sqrt{\frac{2}{\kappa_{nl}^2 - l(l+1)}} \quad \Xi_{00} = \frac{1}{\sqrt{3}}$$

See the appendix of Cates *et al*(1988)[63], for the method of finding the κ_{nl} , some of their values, and the formula for the normalisation factors; the results of this thesis agree. Abramowitz and Stegun[55], chapter 10, p437–439 also proved useful.

2.5.3 Matrix Elements

Converting a basis set with two labels (radial and angular) to a matrix is not trivial. The matrix must be based on both integers n and l (running from zero to $N_n - 1$ and $N_l - 1$ respectively), which form a single matrix index: $nl = N_n l + n$. The full matrix is therefore made up of a sub-matrix for each value of l , each sub-matrix being of size N_n on each side. The whole matrix is therefore of dimension $N_n N_l$ on each side.

The matrix elements are defined as in Eqn. (A.7). Again, we split the pseudo-hamiltonian matrix into kinetic and pseudo-potential terms; we further split the pseudo-potential into first and second order gradient (terms proportional to b_1 and b_2 in Eqn. (2.61d)). The simplified forms of the matrix elements are taken from the thesis of Agnès Roni[64].

[†]The spherical Bessel functions are distinct from the cylindrical Bessel functions, J_0 used for the radial basis functions Eqn. (2.19) in the cylinder. They are related to the spherical Bessel functions by: $j_l(x) = \sqrt{\frac{1}{2}\pi/x} J_{l+\frac{1}{2}}(x)$. See [55], Eqn.(10.1.1)

The kinetic elements can be found analytically, given the κ_{nl} :

$$T_{nl n' l'} = \kappa_{nl}^2 \delta_{nn'} \delta_{ll'} \quad (2.64a)$$

The integrals for the first-order potential terms can be found semi-analytically: the integrals can be formulated by hand, but the Bessel functions must be evaluated numerically. The radial integrals are to be found in Hasson *et al*[65], Eqn.(A1). The angular integrals are equivalent to Clebsch-Gordon coefficients, (see Abramowitz and Stegun[55] or thesis of Roni[64]).

$$\begin{aligned} V_{nl n' l'}^{(1)} &= \Xi_{nl} \Xi_{n' l'} \int_0^1 \rho^3 d\rho j_l(\kappa_{nl} \rho) j_{l'}(\kappa_{n' l'} \rho) \times \int_0^\pi d\theta \cos \theta P_l^0(\cos \theta) P_{l'}^0(\cos \theta) \\ &= \Xi_{nl} \Xi_{n' l'} \left\{ \frac{j_l(\kappa_{nl}) j_{l'}(\kappa_{n' l'}) [\kappa_{nl}^2 + \kappa_{n' l'}^2 - l(l+2) - l'(l'+1) + 2]}{\kappa_{nl}^2 - \kappa_{n' l'}^2} \right\} \\ &\quad \times \left\{ \frac{(l+1)\delta_{l, l'-1}}{\sqrt{(2l+1)(2l+3)}} + \frac{(l'+1)\delta_{l, l'+1}}{\sqrt{(2l'+1)(2l'+3)}} \right\} \end{aligned} \quad (2.64b)$$

The only non-zero elements are such that $|l - l'| = 1$: they form blocks, one block off-diagonal in the full matrix.

I could not find a formula for the radial integrals for the second-order potential, so they were numerically integrated (using the MATLAB function `quad8`). The angular parts are only non-zero where the difference between l and l' is either zero or two (diagonal or two-off-diagonal blocks), and can be found as for the first-order angular integrals[64].

$$\begin{aligned} V_{nl n' l'}^{(2)} &= \Xi_{nl} \Xi_{n' l'} \int_0^1 \rho^4 d\rho j_l(\kappa_{nl} \rho) j_{l'}(\kappa_{n' l'} \rho) \times \int_0^\pi d\theta P_2^0(\cos \theta) P_l^0(\cos \theta) P_{l'}^0(\cos \theta) \\ &= \Xi_{nl} \Xi_{n' l'} \int_0^1 \rho^4 d\rho j_l(\kappa_{nl} \rho) j_{l'}(\kappa_{n' l'} \rho) \times \\ &\quad \left\{ \frac{6(l'+1)^2(l'+2)\delta_{l, l'+2}}{(2l'+2)(2l'+3)\sqrt{(2l'+1)(2l'+5)}} + \frac{2l(l+1)\delta_{l, l'}}{(2l-1)(2l+3)} \right. \\ &\quad \left. + \frac{6(l+1)^2(l+2)\delta_{l, l'-2}}{(2l+2)(2l+3)\sqrt{(2l+1)(2l+5)}} \right\} \end{aligned} \quad (2.64c)$$

2.5.4 Results

Several tests are required to ensure that the computing is correct, mainly comparison with the results of calculations by other groups, most notably that of Don Candela[61]. The simplest test was comparison of matrix elements, with Gerard Vermeulen (senior colleague of Agnès Roni[64]). Also, we have successfully reproduced Figs.2a, 2b and 5b of Candela *et al*(1991)[61]. Figures 2a and 2b therein show

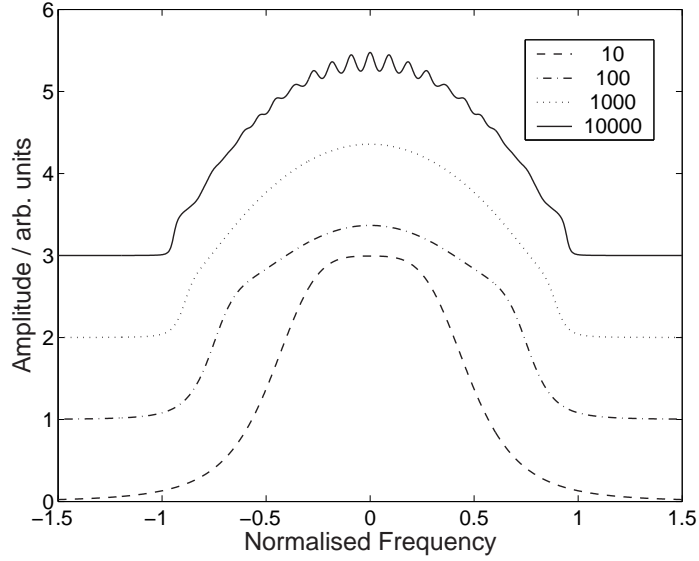


Figure 2.17: High-temperature lineshape for a sphere in a linear gradient. $\mu M_0 = 0$; $b_2/b_1 = 0$; $N_l = 31$; $N_n = 6$. b_1 is shown in the legend. The ideal shape, where there is no spin-transport, is a parabola from -1 to +1.

spatial variations of a few eigenfunctions, and the lowest few eigenvalues as functions of gradient parameter (his Δ is related to the parameters we use: $\Delta^3 = i/b_1$). Figure 5b shows real and imaginary parts of a spectrum.

The final test of the maths is the lineshape when the Leggett-Rice effect is absent, and spin diffusion is minimal. All of Candela's figures were produced using the first seven spherical Bessel functions and 32 Legendre polynomials ($l = 0..6, n = 0..31$), so the same basis set is used to calculate Fig. 2.17. The spectrum is expected to be a parabola from -1 to +1 in normalised frequency units (frequency divided by b_1 , as in Fig. 2.5). It is clear that the test is passed, although there are some edge effects near ± 1 ; the distortions are strongest when b_1 is smallest. For $b_1 = 10^4$, the basis set is not large enough, so the spectrum is distorted in the middle of the cell, near zero frequency.

The tests having been passed, we can now calculate the magnetisation for arbitrary field variations up to second order, which allows me to produce eigenmodes, FIDs, spectra, spin-echoes and even look at the time-space variation of magnetisation. No such results are shown here, because they have either been done before[61], or are very difficult to visualise (space-time variation requires three plotting dimensions), or look substantially the same as the cylinder (spin-echoes). A sphere and a right-cylinder are quite similar in proportion, although their spin-wave mode degeneracies are different.

CHAPTER 3

COMPARING THE MODEL TO 6.2% ^3He - ^4He MIXTURE DATA

This chapter describes the comparison between the model developed in chapter 2 and experimental data. First comes the details of the experiments performed in Nottingham from October 1999 to July 2000, at saturated vapour pressure, in 0.5% and 6.2% ^3He - ^4He and in pure ^3He . Then, we extend and improve the spin-transport model, and use it to understand both spectra and spin-echo data by *least-squares fitting*. The results of the spin-echo fitting will reveal the variation of spin-transport parameters with temperature, allowing us to measure the *anisotropy temperature* of the 6.2% mixture.

3.1 Background

Various groups have carried out NMR experiments to test the ideas of Meyerovich and Musaelian[19][20], Jeon and Mullin[21], and Fomin[24] on transport decoherence at extreme low temperature in Fermi-liquid ^3He - ^4He mixtures. Wei *et al*[45] measured spin-echo attenuation in ^3He to determine the transverse spin-diffusion coefficient, D_{\perp} , as a function of temperature: They observed saturation corresponding to an anisotropy temperature of $T_a = 16\text{mK}$ in an 8T magnetic field. Ager *et al*[28] found $T_a = 19\text{mK}$ in a 6.2% ^3He - ^4He mixture (just less than saturation; see Dobbs[1], p208–219) in 8.8T. These early results supported the theory which predicts that spin-transport properties do not diverge (Jeon and Mullin[21], Meyerovich

and Musaelian[19][20]), with values of T_a larger than expected, but not inconsistent with the theory. The theory is valid only at very low concentrations of ³He, so no direct comparison could be made between theory and experiment. More recent experiments using spin-echoes have found smaller anisotropy temperature: Akimoto *et al* found 12mK in 14.7T using very dilute, 0.09% ³He-⁴He [46]; and 4.3mK in $\approx 3.8\%$ ³He-⁴He in 14.7T[47].

Owers-Bradley *et al*[48] and Candela *et al*[39] (in Nottingham) found 13mK and 12mK (6.2% ³He-⁴He and pure ³He respectively) in 11.3T. In this chapter, the data from the Nottingham experiments of 1999 and 2000 are analysed using a modified version of the model developed in chapter 2. For this system, the dilute-limit theory predicts $T_a(11.3T) = 2.8\text{mK}$ (or 2.5mK in 10T field)[21][16].

By contrast, Vermeulen and Roni[43] used a spin-wave damping technique, with enhanced polarisation, and measured no saturation of spin-diffusion, more in agreement with Fomin (although the other theories could not be ruled out due to the uncertainty of their results): they found an upper limit of $T_a = 2.5\text{mK}$ at 10T. Also, Candela *et al*[61] measured the spin-rotation parameter, using a model to compare with the spin-wave spectra, in very dilute ³He-⁴He mixtures in 8T down to 7mK: they found no systematic deviation from $1/T^2$. The same group did something similar for their 1986 paper[37], which studied pure ³He at low field.

Summary of Experiments

Table 3.1 shows a summary of the spin-transport experiments in ³He-⁴He mixtures. There is a great variation in the results, particularly the anisotropy temperature, as normalised to 10 tesla ($T_a \propto B$ is expected). A major factor in the variation of results is likely to be the influence of the boundaries, which affect the number of significant spin-wave modes (or diffusive equivalents where μM_0 is nearly zero, 3.8%³He). Where there are few such modes, boundaries cannot be neglected in any analysis, particularly of spin-echo experiments. The current chapter is a presentation of the analysis using the model of chapter 2, as published by Buu *et al*[53, 54].

Data-Analysis Methods

Most of the high-field experiments use the method of spin-echoes. Commonly, two graphs are plotted: log-amplitude of echo against cube of inter-pulse waiting time ($\ln |S(t_{\text{echo}})| = \ln |h|$ against t_w^3); and phase of echo against log-amplitude of echo ($\arg(S(t_{\text{echo}})) = \phi$ against $\ln |h|$). Straight lines are fitted through the results, and the spin-transport parameters are determined by comparison with the equations (39)

Ref.	Authors	Year	Conc ⁿ %	Field Tesla	Method	$T_a(10T)$ mK	N_{modes}
[41]	Owers-Bradley <i>et al</i>	1983	5	0.028	Wave	n/a	n/a
	” ”	”	9.5	”	Wave	”	”
[27]	Ishimoto <i>et al</i>	1988	1.3 to 8.6	0.03–0.06	Wave		n/a
[61]	Candela <i>et al</i>	1991	0.06	8	Wave	n/a	8–19
	” ”	”	0.18	”	Wave	”	18–40
[28]	Ager <i>et al</i>	1995	0.05 to 0.46	8.8	Echo	n/a	n/a
	” ”	”	1	”	Echo	9	21
	” ”	”	3.8	”	Echo	15	8
	” ”	”	6.4	”	Echo	22	15
[48]	Owers-Bradley <i>et al</i>	2000	6.2	11.3	Echo	12.1	41
[43]	Vermeulen, Roni	2001	9.3	5×10.5	Wave	< 2.5	> 20
[46]	Akimoto <i>et al</i>	2002	0.09	14.7	Echo	8	200
[53, 54]	Buu <i>et al</i>	2002	6.2	11.3	Echo	5.5	44
[47]	Akimoto <i>et al</i>	2003	3.8	14.7	Echo	2.9	12–20

Table 3.1: Comparison of experiments in ³He-⁴He mixtures. Anisotropy temperature assumed $\propto B$, normalised accordingly. Fermi temperature is very low for concentrations less than 1%. There may be mean free path effects in [46]. Finite size effects are only negligible if $N_{\text{modes}} \gtrsim 50$. [43] uses a non-equilibrium enhanced polarisation method. [53, 54] is a re-analysis of [48], and is described in detail in this chapter. N_{modes} calculated using Eqn. (2.44), and information in the papers.

and (43) of Leggett[26], which are equivalent to Eqn. (1.24)(a and b) in this thesis. Akimoto *et al*[47] fitted phase and amplitude simultaneously, treating the complex signal at echo, $he^{i\phi}$, and varying the complex effective spin-diffusion coefficient, D_{eff} .

Vermeulen and Roni measured the half widths of the peaks in their spectra, as functions of the shifts of the peaks, for each temperature and polarisation. They found the widths were proportional to the shifts and measured the constant of proportionality. By applying semi-analytic results for the lowest modes trapped in a cylinder[37] or sphere[61] they used the constant of proportionality to measure the spin-transport parameters. By contrast, Candela *et al*[61] fitted a part of the spectrum in a least-squares manner, using a linear spin-wave mode model.

3.2 Experiments

The experiments detailed and analysed in this chapter were performed between October 1999 and July 2000, shortly before I began working with the group in Nottingham. The same cell was used for experiments in pure ³He until December 1999, then 6.2% ³He-⁴He from February to April 2000, then 0.5% ³He-⁴He during June and July 2000. The details of the cell and the principle results have been presented elsewhere: in the two papers by Buu *et al*[53][54], and the thesis of D

Clubb[66].

Broadly the experimental apparatus consisted of a cylindrical *cell* surrounded by an NMR coil, attached to an adiabatic-demagnetisation refrigerator. The cell was connected by a *filling channel* to a *reservoir* containing the thermometry, which was in turn connected to a heat-exchanger. A diagram of the apparatus is shown in Fig. 3.1.

Experiments were performed in the temperature range 3–100mK. Above 15 millikelvin, the dilution fridge was used alone. At 15mK the adiabatic demagnetisation stage was loaded with a large field, pre-cooled with the dilution fridge, thermally disconnected using a superconducting heat-switch; then the field could be reduced with a corresponding reduction in temperature (see Pobell[67], chapter 10, p181–224).

3.2.1 The Experimental Cell

The NMR cell was a hollow cylinder made of Stycast1266 epoxy resin, of inner diameter 2.3mm and length 2.3mm. It was connected to the reservoir by a 10mm long, 0.5mm diameter filling channel.

Both the reservoir and the heat-exchanger were made of silver. The reservoir had a capacity of 1.3cm^3 , and the lower part contained silver-sinter. The upper part contained a *vibrating-wire resonator* (VWR) viscometer/thermometer. The reservoir was connected to the heat-exchanger by a cupronickel capillary. The 200mm long heat-exchanger was packed with silver sinter, and was screwed onto a copper adiabatic-demagnetisation stage. The adiabatic-demagnetisation stage consisted of specially shaped annealed copper, mounted on a commercial dilution fridge. Up to 9T could be applied to the demagnetisation stage (cancelled in the sample region and near the superconducting heat-switch); a separate sample field up to 12T could be applied. A thermal shield hanging from the mixing chamber of the dilution fridge could be used as a heat-sink. At the lowest temperatures, up to 12 hours was allowed for the system to reach thermal equilibrium.

Thermometry

The thermometry for the cell was provided by the VWR in the reservoir. From the shift in resonant frequency and the damping, the viscosity of the helium can be measured, which in turn allows the temperature of the helium to be determined [11][12][13][68]. The temperature of the helium may be different from the temperature of the surrounding materials, despite the silver-sinter heat-exchanger, due to the Kapitza, thermal boundary-resistance effect. There was also a capacitance

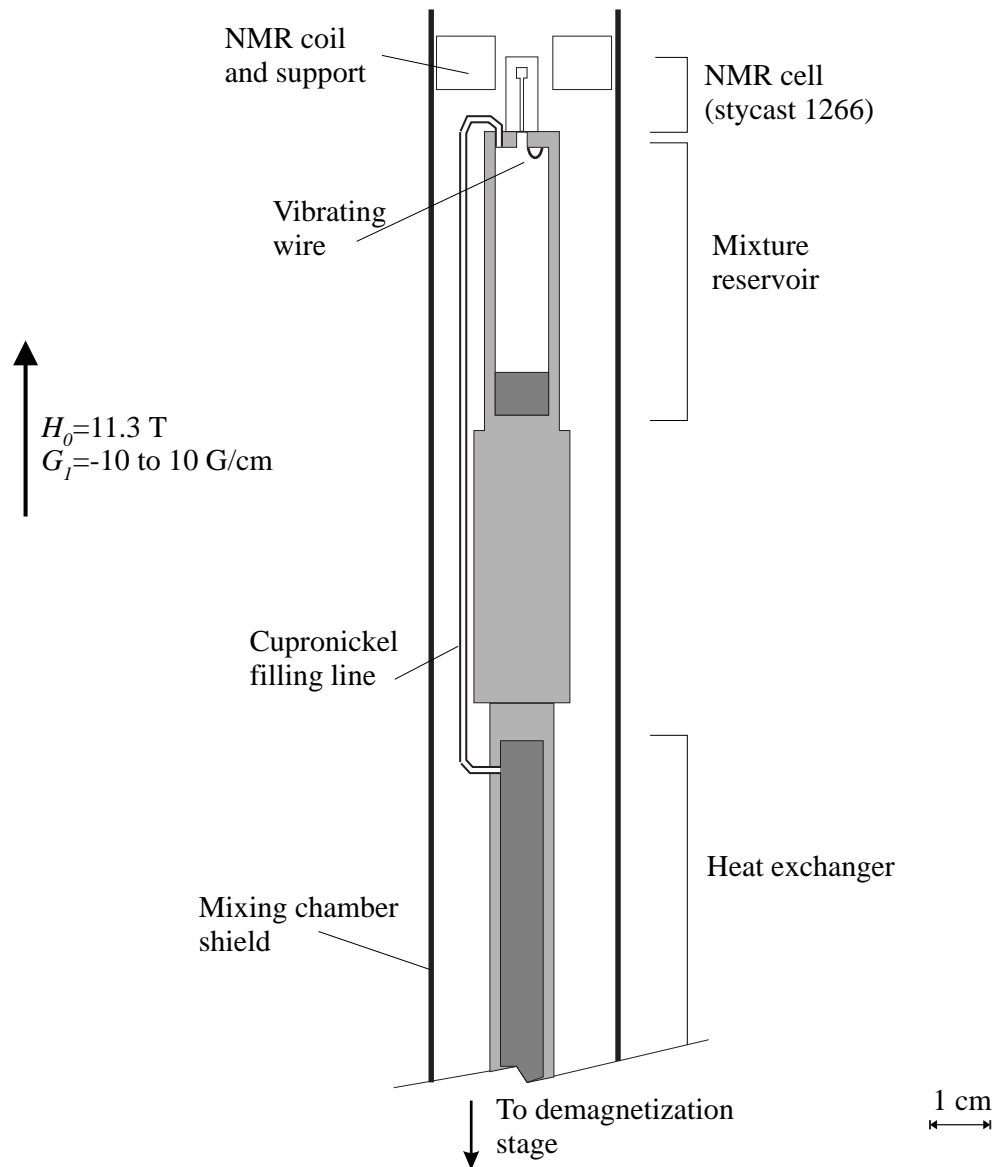


Figure 3.1: Experimental Apparatus: Heat-exchanger and mixture reservoir are made of silver. Heat-exchanger is mounted on the adiabatic-demagnetisation stage. NMR coil is not in thermal contact with the cell; it is heat-sunk to the mixing chamber shield. Figure by Olivier Buu, re-produced from Buu *et al*[53].

thermometer in the reservoir, which did not give reliable readings.

Attached to the mixing chamber of the refrigerator were: a Gold-Erbium (AuEr) thermometer, measuring magnetic susceptibility; a Palladium-Iron (PdFe) thermometer, using the same principle as the AuEr; a Ruthenium Oxide (RuO_2) thick-film chip resistance thermometer; and a set of superconducting fixed-point thermometers for calibration down to about 15mK. For more details of these thermometers, see Pobell[67], chapters 11 and 12 (p226–302). A separate RuO_2 resistor was attached to the adiabatic-demagnetisation stage; it gave accurate readings of the helium temperature down to about 15mK.

3.2.2 NMR Details

The cell was placed within a 6mm diameter NMR saddle coil, tuned to 367MHz (corresponding to 11.3T sample field). The coil was embedded in a support made of Stycast1266, which was attached to the mixing-chamber shield. There was no direct mechanical contact between the coil and the cell, preventing heat transfer when rf-pulses were transmitted; pulses could be up to 50W and $30\mu\text{s}$. A significant fraction of the excess heat was dissipated in the mixing chamber, rather than the demagnetisation stage, reducing the temperature rise caused by each NMR pulse (see section 3.6.2). Static field gradients in the range -100 to +100mT/m were applied to promote spin-transport. The residual line-width after shimming was about 600Hz.

Some of the data from experiments on 6.2% ^3He - ^4He have been published by Buu *et al*[53][54] and Owers-Bradley *et al*[48][†]. Also there are some examples in David Clubb's thesis[66].

FIDs

For Free Induction Decay (FID) experiments on 6.2% ^3He - ^4He , the tipping angle was usually 7° , corresponding to a pulse duration of $1\mu\text{s}$. The NMR frequency was often de-tuned from resonance, by a few kHz, to avoid mains noise at $\pm 50\text{Hz}$ and multiples, as well as any dc offset. By convention, the imaginary part of the spectrum (the Fourier transform of the FID signal) is called the *absorption spectrum*, the real part is the dispersion spectrum.

Many FIDs were taken, with various applied gradients at various temperatures, which can of course be turned into spectra. For certain field gradients, peaks can be seen, which are more prominent for lower temperatures, indicating that they

[†]I was not involved in the experiments which produced the NMR data, but did work on some of the data analysis.

are *spin-wave modes*. When the gradient is reversed, the peaks change character, probably due to the influence of the filling channel.

Spin Echoes

Spin-echo experiments were also carried out: a tipping pulse of 21° ($3\mu\text{s}$ in the 6.2% mixture, with an RF-field strength around 0.6mT), followed by a π -pulse (which lasted for $26\mu\text{s}$) after a waiting period of a few milliseconds. For each combination of temperature and gradient, a sequence of spin-echo experiments was performed, with varying inter-pulse waiting times. Between the experiments, time was left for magnetic and thermal equilibrium to return: up to two hours. Also, some multiple-spin-echo experiments (MSEs) were carried out: MSEs exploit the non-linear behaviour of the spin-dynamics, and involve two 90° pulses separated by a waiting period.

The spin-echo experiments were analysed by David Clubb[66] using a simple data-analysis program written in MATLAB by Olivier Buu (see Appendix B). The program derived the amplitude and phase of the each of the echoes in a train, with systematically varied inter-pulse waiting times. The phase should be a smoothly increasing (or decreasing depending on the sign of μM_0) function of the waiting time. However, when there are few data points, it is not clear if the phase should be incremented by 2π , or even 4π ; such a judgement was made by Clubb on a case-by-case basis. Also, the times of the echoes were obtained: the echoes were sometimes delayed, sometimes early (see Fig. 2.7 and Fig. 2.8 for a theoretical prediction of the same thing).

From the analysis of echo amplitude and phase, the formulae of Leggett[26] were applied. Straight lines were fitted, using linear-regression routines in a program called `Origin`, through graphs of $\ln|h|$ versus t_w^3 and ϕ versus $\ln|h|$. The straight-line fits yielded the transport parameters D_\perp and μM_0 , for each temperature at which a train of echoes was taken. Thus a picture was drawn of the spin-transport coefficient variation with temperature, and published (Owers-Bradley *et al*[48]). In the Chapter 2 it was established that formulae in Eqn. (1.24)(a and b) could not always be directly applied with any accuracy. From the number of modes expected to be present in the cell (Table 3.1) it seems likely that experiments re-analysed here violate Leggett's approximation of an unbounded experimental region.

3.3 Assumptions of the Model

A model of the spin-dynamics was developed in chapter 2, and now one must check how valid were the assumptions which were made; where the assumptions were not valid for the experiment being discussed, the model should be modified.

The most obvious assumption is that the spin-dynamics can be treated linearly, as in Eqn. (2.2) to Eqn. (2.8); the tipping pulses are assumed to be very small, and the π -pulses are assumed to be uniform and to invert the magnetisation exactly. See section 3.4.2 for a more detailed treatment of the non-linear behaviour.

All of the simulations in chapter 2 take the initial tipping to be uniform, as well as the receiver-response function. The latter assumption is quite valid, as the NMR coil is much larger than the cell. However, the initial tipping angle is only uniform under certain conditions: see section 3.4.1.

3.3.1 Mean Free Path

The equations of Leggett and Rice[25][26] are hydrodynamic: they are local and describe a continuous medium. They are valid only if the mean free path is smaller than both the size of the sample and the distance over which the distribution of *elementary excitations* changes significantly. The latter length scale is equivalent to the inverse of the free-space wave-number, Eqn. (2.56a), which is sometimes known as the de-phasing length, and is also equivalent to the length of the cell divided by the number of eigenmodes (Eqn. (2.44)), $2L/N_{\text{modes}}$. Therefore we look to see if

$$v_F \tau_{\perp} < 2L/N_{\text{modes}} \quad (3.1)$$

is satisfied, where v_F is the Fermi velocity and τ_{\perp} the *transverse spin-transport lifetime*.

The 6.2% ³He-⁴He sample to be treated in this chapter has $T_F = 410\text{mK}$, implying $v_F = 29\text{ms}^{-1}$ (effective mass is approximately $m^* \simeq 2.5m_{\text{He3}}$, see Ishimoto *et al*[27], Table I); extrapolated to the lowest temperatures (3.5mK), $\tau_{\perp} \lesssim 2\mu\text{s}$. Therefore the mean free path is never greater than $60\mu\text{m}$. The inverse wave-number in free space is greater than $2.3\text{mm}/41 = 56\mu\text{m}$ at the lowest temperatures. Consequently, we expect the hydrodynamic equation of motion to be valid to the lowest temperatures, especially if there is any anisotropy or low-temperature saturation of spin-transport.

3.3.2 Magnetic Relaxation and the Boundary Condition

In the hydrodynamic equation of motion Eqn. (2.1), there is no mention of magnetic relaxation, except through diffusion. It is assumed that other relaxation processes are negligible, i.e. that T_1 and T_2 are much longer than the time for diffusion. We know diffusion occurs on the order of a few milliseconds in ^3He and ^3He - ^4He mixtures. The bulk longitudinal relaxation time, T_1 , is always greater than 100s in an 11T field, for either 6% ^3He - ^4He or pure ^3He (van Steenberg *et al*[69]). Indeed, in the 6% mixtures, at 100mK, the bulk T_1 is estimated to be greater than 10 000 seconds. It is reasonable to assume that the intrinsic transverse magnetisation time, T_2 , will be of the same order of magnitude.

Magnetisation relaxation must therefore be dominated by surface relaxation propagated by spin-diffusion, which raises a query about the boundary condition, which has previously been taken to be the same as used by Candela *et al*[37]: $(\mathbf{n} \cdot \nabla)m = 0$. The idea is that an active layer near the surface (about the same thickness as an intrinsic coherence length) relaxes much faster than the bulk, and the resulting non-equilibrium magnetisation distribution drives diffusion of magnetisation to the wall, promoting further relaxation. The rate is limited either by the surface relaxation or by the bulk diffusion coefficient. There are no publications which detail surface relaxation rates for the interface between Stycast1266 and ^3He or mixtures. Candela *et al* argue, using numbers for surface relaxation on Grafoil, that the T_2 close to the surface is at least $100\mu\text{s}$. For physically reasonable wave-numbers (smooth magnetisation distribution), the boundary condition is well satisfied; also relaxation is much slower than bulk spin-diffusive losses by at least three orders of magnitude (see Buu *et al*[54]). Surface relaxation is particularly slow for impure ^3He , as the surfaces are probably coated by a thin layer of (non-magnetic) ^4He , due to its lower zero-point motion. Therefore the fastest magnetisation loss mechanism by far is diffusion, so ignoring T_1 and T_2 is a good approximation.

3.3.3 Filling Channel

There are three main issues with the filling channel: the change in the boundary condition, longitudinal spin-transport from the reservoir, and instabilities due to non-linear behaviour.

Longitudinal spin-diffusion is usually measured by inverting the magnetisation in a cell much like the one used in these experiments, and then observing the magnetisation recovery due to diffusion from the reservoir. Since the channel is long and narrow, and longitudinal spin-diffusion is similar in magnitude to transverse

spin-diffusion, we can neglect the effects of longitudinal spin-transport.

The cell is not a perfect, spin-reflecting cylinder: the filling channel breaks the symmetry, and must locally alter the boundary condition (the channel does not reflect magnetisation as the walls do). The data show that the channel does strongly affect the spin-wave spectra: see Figure.4 of Buu *et al*[53]. The effect depends on the sign of the applied field gradient. If the gradient is such that the longest-lived spin-wave modes are trapped against the wall of the cell furthest from the filling channel, then the channel may only weakly perturb the spectrum. The opposite also holds: the other sign of gradient forces modes trapped near the channel, making them strongly perturbed.

If we describe spin-echo experiments as sums over spin-wave modes, and if the modes before the π -pulse are weakly perturbed, then those after the π -pulse must be strongly perturbed, and vice versa. However, if the evolution of magnetisation before the π -pulse is only weakly perturbed, then after the π -pulse it takes a time at least as long as the inter-pulse waiting time for the magnetisation to reach the filling-channel end of the cell. Therefore, for the correct sign of gradient, even a spin-echo experiment is well described by the cylindrical-boundary condition.

There are some complicated issues involving instabilities of spin-transport when two volumes with opposite values of longitudinal magnetisation are connected by a channel: the so called Castaing instability[70][71][72]. Again the geometry of the filling channel saves us: spin-transport is stable on the timescale of a typical experiment. A more quantitative treatment of the channel is not possible without a non-linear simulation of spin-transport in the channel itself, and a more complete understanding of the magnetic field variation, which is much more computationally demanding than a simple cylinder, or sphere.

3.3.4 Demagnetising Field

The *demagnetising field*, also known as the dipolar field, is the magnetic field due to the magnetisation of the sample. It is geometry dependent, and scales with the magnetisation density of the helium. In chapter 4, the demagnetising field is treated more completely. For now, a simple order or magnitude estimate will suffice.

Table I of Krotkov *et al* suggests we should expect a demagnetising field frequency scale of $f_M \sim 20\text{Hz}$. The demagnetising field becomes important when f_M is as large as either the field inhomogeneity, $f_{G_1} = (2/2\pi)\gamma G_1 L \sim 7500\text{Hz}$, or the characteristic free space frequency of spin-wave modes (Eqn. (2.56b)), $f_C = f_{G_1}/N_{\text{modes}} \sim 180\text{Hz}$. Clearly the demagnetising field will have no more than a

perturbative effect on the spin-dynamics of the saturated mixture, although it will be important for pure ^3He .

3.3.5 Static Magnetic Field Variation

We have taken only the first three terms in the Legendre-polynomial expansion of the magnetic field (central Larmor frequency, G_1 and G_2 in Eqn. (2.11)), and only the component parallel to the cell axis. Off-axis components of field have second-order effect, and so can be neglected in the secular approximation made while deriving the linearised equation of motion Eqn. (2.8).

In the cylinder the equation of motion is separable provided G_3 and higher terms are zero. As we will see in sections 3.5.1 to 3.6.2, the uncertainties in the first and second order field gradients mean that we have no useful knowledge of higher order terms. It therefore makes sense to terminate the expansion at G_2 .

Also, the magnetic field due to the magnetisation of the material of the cell walls (Stycast 1266) should be negligible; the magnetic field gradient due to the cupronickel capillary is also small. Such stray magnetic fields are considered by Buu *et al*[53][54].

3.3.6 Thermal Equilibrium and Temperature Changes

The time to reach thermal equilibrium was estimated to be less than two hours, based on some thermal modelling of the fridge by Olivier Buu. The magnetic relaxation times are less than 1000 seconds. Two hours were left between spin-echo experiments. There is a serious issue (Ragan *et al*[73]) around the temperature rise due to the inversion of the magnetisation in a spin-echo experiment. The results of such an analysis are included in the temperature error bars on the results in section 3.6.

The cell was likely to be in good thermal contact with the reservoir, including the thermometers, even at the lowest temperatures, due to the thermal conductivity of the helium solution: the time-constant for thermal equilibrium between the reservoir and cell is a few hundred seconds. Again, read the paper Buu *et al*[53] for more details.

3.4 Improvements to the Model

The only addition to the model needed for data analysis is the effect of finite amplitude and duration RF-pulses. This section also contains a comparison between

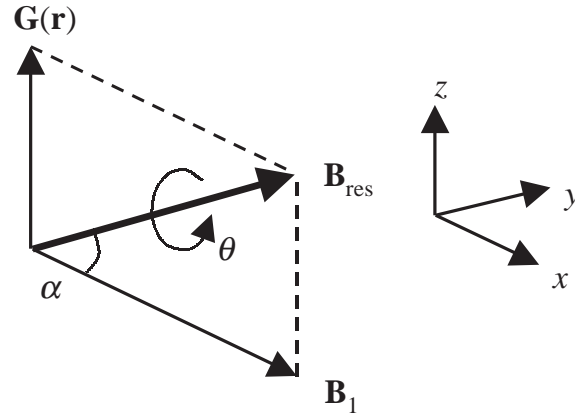


Figure 3.2: RF-Pulses: A diagram showing the resultant field. The symbols will be used in the mathematical description of finite NMR pulses. The resultant magnetic field in the rotating Larmor frame, $\mathbf{B}_{\text{res}}(\mathbf{r})$ is a vector sum of the static field inhomogeneity in the z -direction, $\mathbf{G}(\mathbf{r})$, and the instantaneous RF-pulse field $|\mathbf{B}_1|$

the improved model and the non-linear model (due to V.V. Dmitriev), which also accounts for such pulses.

3.4.1 Finite Pulses

The idealised model assumed that the RF-pulses are infinitely sharp: they change the magnetisation uniformly and in no time, as in Eqn. (2.38) and Eqn. (2.48). A brief calculation shows that ideal pulses are unlikely to be a good approximation: a spin at one end of the cell de-phases by a radian relative to spins at the other end in a time approximately $1/2\gamma G_1 L \simeq 21\mu\text{s}$ in a typical experiment; the duration of a π -pulse is around $26\mu\text{s}$. Therefore significant precession occurs during a π -pulse, so the change in magnetisation must be non-uniform[†]. Any non-hydrodynamic behaviour should decay on a time-scale τ_{\perp} , the transverse spin-transport lifetime[25], which is much quicker than any timescale on which the simulation is run.

Rotation in Real Space

Fig. 3.2 shows the symbols to be used in describing the finite pulses mathematically. A pulse is intended to rotate the magnetisation uniformly by an angle, θ , about the x -axis. Instead, the rotation is by an angle $\theta(\mathbf{r})$, about an axis which is rotated around the y -axis by $\alpha(\mathbf{r})$ from the x -axis; both angles depend on position through

[†]During the following analysis, spin-motion during pulses will be neglected. Such spin-motion would involve large-angle deviation from equilibrium, meaning non-linear behaviour which is beyond the scope of the model.

the field inhomogeneity. θ is the angle due to Larmor precession during the time of the pulse, t_{pls} . The RF-field, \mathbf{B}_1 , is taken to be parallel to the x -axis and the field inhomogeneity $G(\mathbf{r})$ is parallel to the z -axis, as in section 2.1, page 30.

$$\alpha(\mathbf{r}) = \arctan \left(\left[G_1 z + G_2 \left(z^2 - \frac{\rho}{2} \right) \right] / |\mathbf{B}_1| \right) \quad (3.2a)$$

$$\theta(\mathbf{r}) = \gamma t_{\text{pls}} |\mathbf{B}_{\text{res}}(\mathbf{r})| = \gamma t_{\text{pls}} \left(\left[G_1 z + G_2 \left(z^2 - \frac{\rho}{2} \right) \right]^2 + |\mathbf{B}_1|^2 \right)^{1/2} \quad (3.2b)$$

The rotations are performed by pre-multiplying the vector magnetisation by the relevant Euler matrices:

$$\mathbf{R}_y(\alpha) = \begin{pmatrix} 1 & 0 & 0 \\ 0 & \cos \alpha & \sin \alpha \\ 0 & -\sin \alpha & \cos \alpha \end{pmatrix} \quad (3.3a)$$

$$\mathbf{R}_x(\theta) = \begin{pmatrix} \cos \theta & 0 & -\sin \theta \\ 0 & 1 & 0 \\ \sin \theta & 0 & \cos \theta \end{pmatrix} \quad (3.3b)$$

The combination of the two rotations, i.e. precession by $\theta(\mathbf{r})$ about the local effective field direction $\alpha(\mathbf{r})$ is:

$$\mathbf{R}_{x'}(\alpha, \theta) = \mathbf{R}_y(\alpha) \mathbf{R}_x(\theta) \mathbf{R}_y^T(\alpha) \quad (3.4)$$

Conversion between Representations

For most of this thesis, and in most of the simulation code, the complex number representation of the magnetisation m_{\pm} has been used, in either the basis set Eqn. (2.19) or the sum over eigenfunctions Eqn. (2.31). The rotations are easiest to code in real space, and relate to the vector $\mathbf{M}(\mathbf{r})$ with three elements. It is trivial to convert from m_{\pm} to a vector, but basis-set to real-space is not.

In a computational implementation, one generally solves the *pseudo-hamiltonian* matrix for the eigenfunctions in the basis set as defined in section 2.2.2. Therefore conversion between a sum over eigenfunctions and a sum over basis functions is trivial. Converting from basis to real space is done by defining matrices for forward and backward transformations, which are in general non-square matrices. First, axial conversions: $\tilde{\psi}(k_l)$ or $\tilde{\psi}_l$ is a function in the basis, $\psi(\zeta_j)$ or ψ_j is a discrete real space representation of the same function, much as in section 2.2.4:

$$\tilde{\psi}(k_l) = \int_{-1}^{+1} d\zeta \Theta_l \cos(k_l \zeta) \psi(\zeta) \simeq \sum_{j=1}^{N_z} \Theta_l \cos(k_l \zeta_j) \psi(\zeta_j) \quad (3.5a)$$

$$\tilde{\psi}_l = \sum_{j=1}^{N_z} A_{jl}^{\zeta \rightarrow k} \psi_j \quad A_{jl}^{\zeta \rightarrow k} = \Theta_l \cos(\zeta_j k_l) \quad (3.5b)$$

The method relies on converting the integral $\int_{-1}^1 d\zeta f(\zeta)$ to a sum over elements corresponding to positions $\sum_{j=1}^N f(\zeta_j)$. The matrices for forward and backward transformations are the transposes of one another:

$$A_{lj}^{k \rightarrow \zeta} = A_{jl}^{\zeta \rightarrow k} \quad (3.5c)$$

i.e. the reverse transformation is a simple sum, equivalent to a sum the reverse of a sum over positions.

The radial conversions change an integral $\int_0^1 \rho d\rho f(\rho)$ to a sum over elements corresponding to positions $\sum_{l=1}^N \rho_l f(\rho_l)$. Note the integral is over $\rho d\rho$, not $d\rho$:

$$\tilde{\phi}(\kappa_l) = \int_{-1}^{+1} \rho d\rho \Xi_l J_0(\kappa_l \rho) \phi(\rho) \simeq \sum_{j=1}^{N_r} \rho_j \Xi_l J_0(\kappa_l \rho_j) \psi(\rho_j) \quad (3.6a)$$

$$\tilde{\phi}_l = \sum_{j=1}^{N_r} B_{jl}^{\rho \rightarrow \kappa} \phi_j \quad B_{jl}^{\rho \rightarrow \kappa} = \rho_j \Xi_l J_0(\rho_j \kappa_l) \quad (3.6b)$$

Therefore the backward transform is different, a simple sum over functions at given positions rather than a sum over the product of functions and radial-coordinates at given positions:

$$B_{lj}^{\kappa \rightarrow \rho} = \Xi_l J_0(\rho_j \kappa_l) \neq B_{jl}^{\rho \rightarrow \kappa} \quad (3.6c)$$

Note that the effects of a pulse are not separable into axial and radial variations. The rotations must be performed for every point in the two-dimensional space with cylindrical symmetry. The approximation is made that the longitudinal magnetisation, M_z , is uniform, which is most accurate after a small tipping pulse; the spin-rotation parameter μM_0 is taken to be uniform, and of equal magnitude before and after the π -pulse.

Results of Simulations

Fig. 3.3 shows the effect of finite-duration π -pulses for a reasonable experiment (although μM_0 is a little large). The tipping angle θ is 1° . The magnetic field variation across the cell is $2G_1 L = 0.23\text{mT}$. A π -pulse requires $\gamma t |B_1| = \pi$; in figure Fig. 3.3 the RF-field strengths vary from 0.5 to 15mT. For the weakest π -pulse the RF-field is of comparable strength to the field-inhomogeneity, so the magnetisation at the ends of the cell are tipped through angles appreciably away from π radians, distorting the echoes. The finite-pulses cause some of the longitudinal component of the magnetisation to be rotated into the transverse plane, which explains the slight enhancement of the echo.

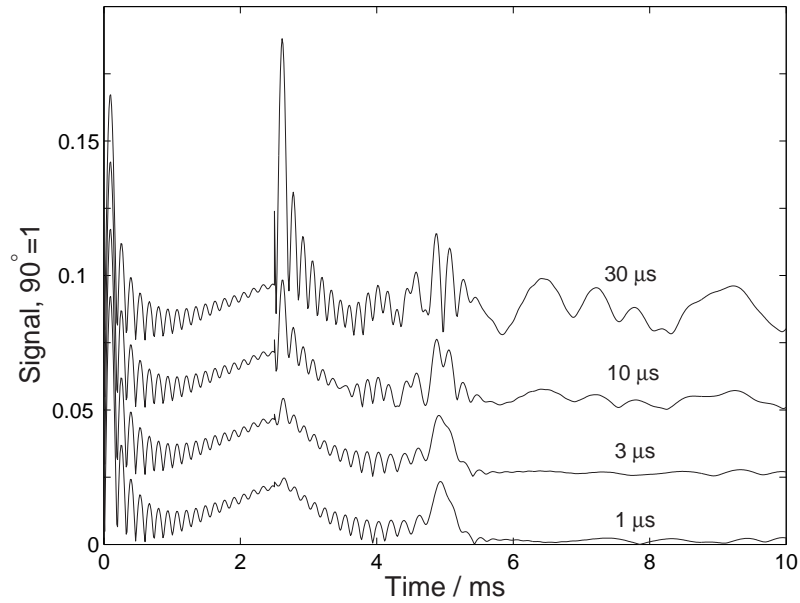


Figure 3.3: Effect of Finite-Duration π -pulses. Parameters for the model are $\mu M_0 = 20$; $D_{\perp} = 10^{-4} \text{ m}^2\text{s}^{-1}$; $G_1 = 100\text{mT/m}$; $G_2 = 0$; $L = 1.15\text{mm}$; $\theta = 1^\circ$ (tipping pulse); The simulation uses 111 axial basis functions (radial variations can be ignored when $G_2 = 0$); π -pulse durations are in the legend. Inter-pulse waiting time is 2.5ms. The finite duration π -pulses distort the echo.

Fig. 3.4 shows an analysis of the spin-echoes for the same parameters as Fig. 3.3, with many different inter-pulse waiting times. The log-amplitude is actually the logarithm of the magnitude of the ratio of the signal around the expected echo time to the maximum signal just after the tipping pulse (which is after time zero for the weakest pulses). Care must be taken to calculate the correct phase. It seems that the finite pulses systematically enhance the echo amplitudes, but leave the phase largely unchanged. The effect is most clearly seen when the π -pulse duration is at least as great as the inverse of the inhomogeneous broadening.

We have also run similar simulations with second order gradients present. The results are confusing: for one sign of second order gradient (positive) the echo is enhanced by a weak π -pulse, but for the other sign (negative) the echo is almost unaffected. In conclusion, any comparison between the model and the data must include the effects of finite π -pulse amplitude and duration.

3.4.2 Non-linearities

Non-linear phenomena in the spin-dynamics of a polarised Fermi-liquid are responsible many interesting phenomena, including: Homogeneous Precessing Domains

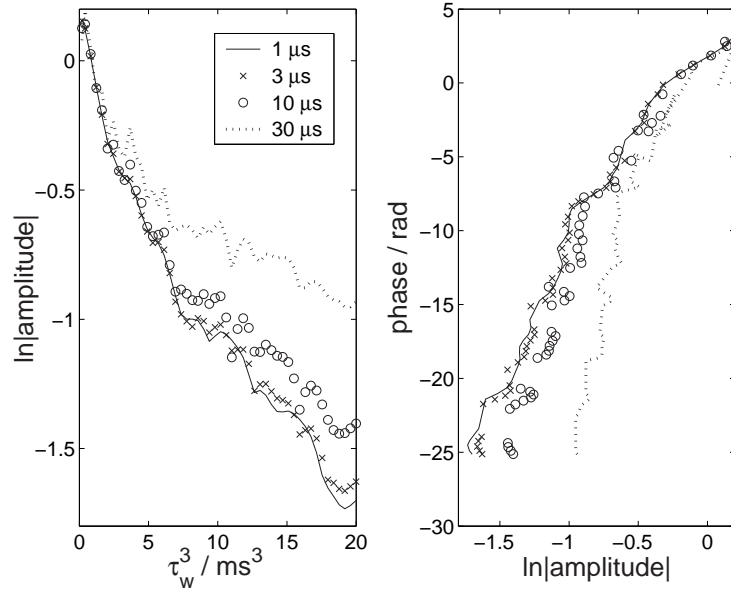


Figure 3.4: Effect of Finite-Duration π -pulses. Parameters for the model are the same as Fig. 3.3: $\mu M_0 = 20$; $D_{\perp} = 10^{-4} \text{ m}^2\text{s}^{-1}$; $G_1 = 100\text{mT/m}$; $G_2 = 0$; $L = 1.15\text{mm}$; $\theta = 1^\circ$ (tipping pulse); The simulation uses 111 axial basis functions (radial variations can be ignored when $G_2 = 0$); π -pulse durations are in the legend. Notice the enhancement of the echo; magnetisation is rotated from the z -direction to the xy -plane by the resultant magnetic field during the π -pulse.

(HPDs, e.g. Borovik *et al*[34] and Fomin[74]); Multiple Spin-Echoes (MSEs, see for example Refs. [75][76][77]); Castaing Instabilities [72][70][71]). Also, the demagnetising field due to the magnetisation of the sample itself affects the motion of magnetisation non-linearly.

We are interested in the small non-linearities which appear when the tipping angle is not very small, and the π -pulses are of small amplitude, so that the inversion of magnetisation is far from perfect. In the experiments in Nottingham, early 2000, the tipping pulses were usually $3\mu\text{s}$ and the π -pulses $26\mu\text{s}$, i.e. a tipping angle of 21° , and pulses of slightly greater amplitude than the field inhomogeneity (about 0.6mT against 0.2mT).

To assess the effects of non-linearities, we have used a simulation of the motion of magnetisation which originated in Moscow (Kapitza Institute, see Dmitriev *et al*[51]), and has also been used extensively by the group of Girgl Eska, in Bayreuth (for example Taubenreuther *et al*[78]).

Presented in Fig. 3.5 are both linear and non-linear simulations of a typical spin-echo experiment, although the spin-rotation parameter is perhaps unrealistically large. The long-time signals are independent of tipping angle, which implies

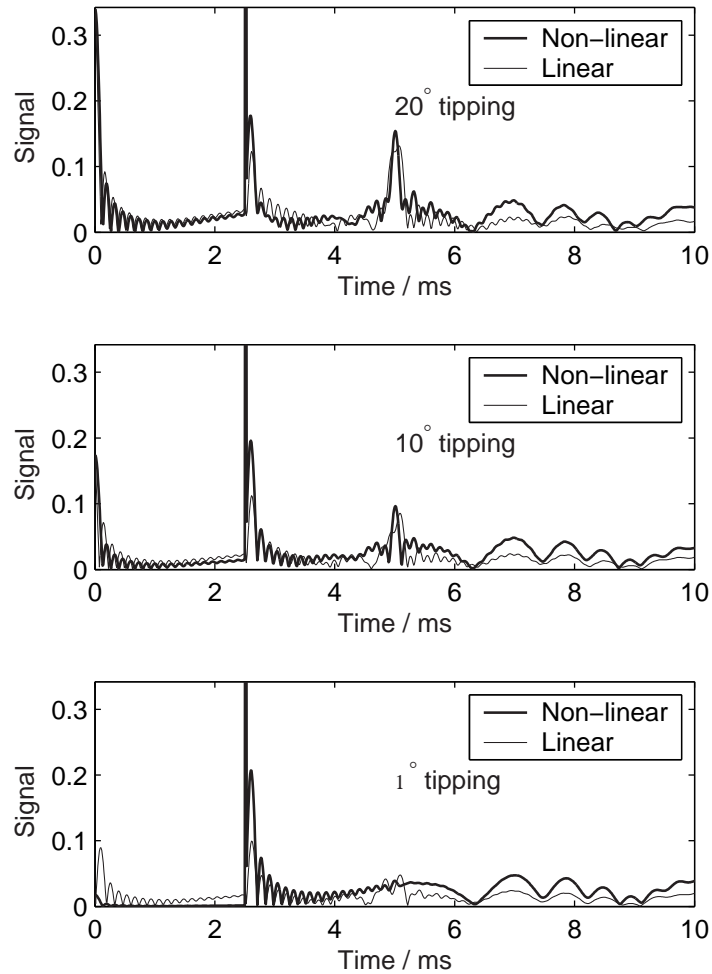


Figure 3.5: Comparison between signals from linear and non-linear models. Parameters are: $\mu M_0 = -29.2$; $D_{\perp} = 1\text{cm}^2\text{s}^{-1}$; $30\mu\text{s}$ π -pulse; $G_1 = 10\text{G}/\text{cm}$; $G_2 = 0$; $N_z = 126$. The signals are scaled so the amplitudes shortly after the π -pulse are similar.

that they are caused by the π -pulse inducing transverse magnetisation. The linear model underestimates the long-time signal amplitude, implying that non-linearities after the π -pulse are responsible for part of the long-time signal. The initial FIDs are equivalent, but the simulation normalises the outputs of the linear and non-linear models differently (the post- π -pulse signals are similar amplitude for both models). The post- π -pulse signals in the 1° simulations are dominated by the imperfections of the π -pulse, meaning non-linear behaviour is important. The 10° and 20° simulations show subtle differences between the models, but the overall features are remarkably similar. It seems that non-linearities are a perturbation to linear-dynamics when the tipping angle is around 10° or 20° , as in the experiments to be analysed. Analyses of many echo simulations are shown in Fig. 3.6 (10° tipping

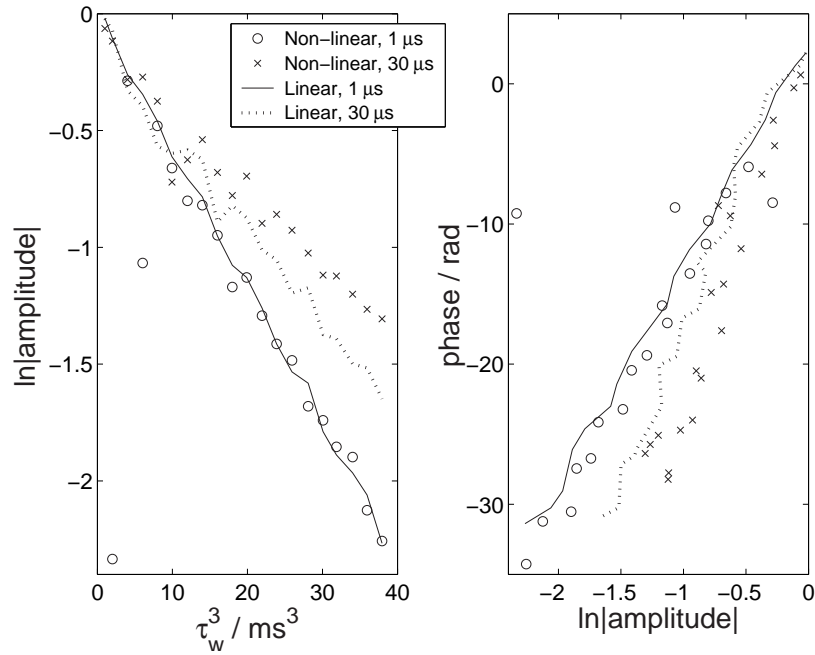


Figure 3.6: Effect of non-linearities (10° tipping): see legend. $\mu M_0 = -29.2$; $D_\perp = 1 \text{ cm}^2\text{s}^{-1}$; $G_1 = 10\text{G/cm}$; $G_2 = 0$; $N_z = 126$; $N_r = 2$; $\theta_1 = 10^\circ$; $\theta_2 = 180^\circ$ Non-linearities enhance the echoes in general, and result mainly from imperfect inversion during the π -pulse.

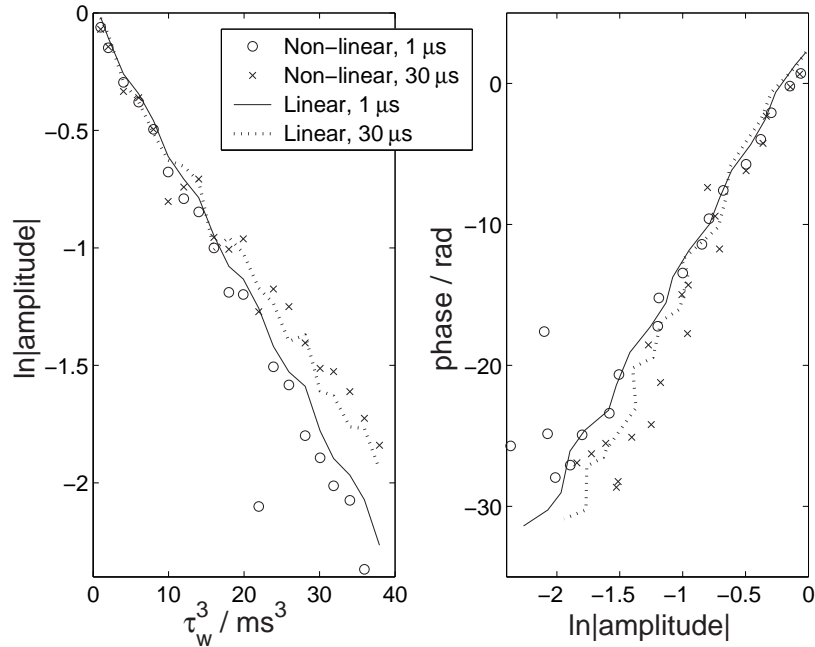


Figure 3.7: Effect of non-linearities (20° tipping): see legend. $\mu M_0 = -29.2$; $D_\perp = 1 \text{ cm}^2\text{s}^{-1}$; $G_1 = 10\text{G/cm}$; $G_2 = 0$; $N_z = 126$; $N_r = 2$; $\theta_1 = 20^\circ$; $\theta_2 = 180^\circ$ Non-linearities enhance the echoes in general, and result mainly from imperfect inversion during the π -pulse.

angle) and Fig. 3.7 (20° tipping angle)[†]. Non-linear effects are counter-intuitively most apparent for smaller tipping angles, since the imperfect π -pulse dominates the spin-dynamics. If an analysis of echo amplitude and phase is carried out for the 21° experiments in Nottingham 2000, then non-linear effects can safely be neglected for computational ease: we can use the model developed in chapter 2, with the imperfect pulse treatment of section 3.4.1.

3.5 Fitting NMR Data

The model so far presented is meant for comparison with real data, produced in Nottingham in 1999 and 2000. Spectra are very sensitive to the magnetic field variation, which makes them useful for determining G_1 and G_2 , but less useful for measuring the spin-transport parameters. Knowledge of the field gradients can be used to fit the amplitudes and phases in spin-echo experiments in 6.2% ³He-⁴He, at several temperatures. Thus the temperature variation of the spin-transport parameters of such a mixture may be determined. The results are published in Buu *et al*[53, 54]

3.5.1 Spectra

The spectra yield much useful information about field inhomogeneity, although some of the results are difficult to explain. The analyses of this section were mostly performed by Olivier Buu, and do not include the effects of finite-amplitude pulses or non-linear terms in the equation of motion.

High-Temperature Lineshape

The easiest data to fit are the spectra (Fourier transforms of FIDs) at high temperature, when spin-transport is negligible. One can calculate the spectrum based on the magnetic field profile in the cell (see Eqn. (2.13a)), and the gradient parameters can be varied until the predicted and measured line-shapes match. The fitting is performed using the `lsqcurvefit` least-squares routine from MATLAB: further details of the algorithm can be found online[57].

The results of the line-shape fitting indicate that the second order gradient, G_2 depends on both the sign and magnitude of the first order gradient G_1 . Furthermore, neglecting the radial variation seems to improve the fit, even if $G_2 \neq 0$. It is possible

[†]In producing Fig. 3.6 and Fig. 3.7 the simulation uses uniform initial tipping, i.e. assuming that the tipping pulse is very strong and short. Therefore, it has perhaps not captured all of the non-linear behaviour which would occur in a real experiment with pulses of equivalent strength to a $30\mu\text{s}$ π -pulses.

that there are terms in the magnetic field of higher than first or second-order, due to the magnetisation of the walls of the cell, or the cupronickel capillary, or the gradient coils. It is not clear how to treat such terms, so we consider a second order expansion to be sufficient for fitting our purposes.

For an example of a fitted line-shape, look in the appendix of Buu *et al*[53]. The results of the line-shape fitting give us good starting parameters for fitting data with the more sophisticated spin-transport based model.

Spin-Wave Modes

Fitting spin-wave spectra at low temperatures gives us more information about the combination of spin-transport parameters. Crudely, counting the number of peaks should allow us to know b_1 , as in Eqn. (2.44), which depends on the ratio $\mu M_0/D_\perp$. The positions of the peaks tell us something about the gradients; the radial variation should generate a family of peaks for each axial peak.

Again we use the MATLAB routine `lsqcurvefit` to least squares fit: the positions of the peaks are checked against the eigenvalues of the pseudo-hamiltonian in the correct units[†]. An example of peak-fitting is presented in Fig. 3.8. The optimal gradients are in broad agreement with the results of the high-temperature line-shape fitting, but the spin-transport parameters disagree with much of the literature. The spectra were calculated with $\mu M_0 = -10$ (using m_+ notation, not m_-), and have sharper peaks than the experimental spectra, probably because of quadratic (and higher order) radial field variations, which are lifting a degeneracy in the simulations.

3.5.2 Spin Echoes

Spin-echo experiments are less sensitive to the magnetic field variation but more sensitive to the spin-transport parameters than spectroscopic experiments. We have seen that we have a model which should compare well to experiments, and we have some idea of the parameters to begin data fitting.

For each spin-echo experiment, the amplitude $|h|$, phase ϕ and echo delay $\delta\tau$ were measured. Each set of experiments at fixed temperature and gradient, with various waiting times, was compiled to give a data set suitable for fitting: a list of inter-pulse waiting times, amplitudes, phases and delays. The analysis was performed by Dave Clubb, using a program which accounted for dead-time and effects of RF amplifiers.

[†]Other groups have compared a linear model to real spectra, not always using a least-squares method. See Refs. [37][42][43][61].

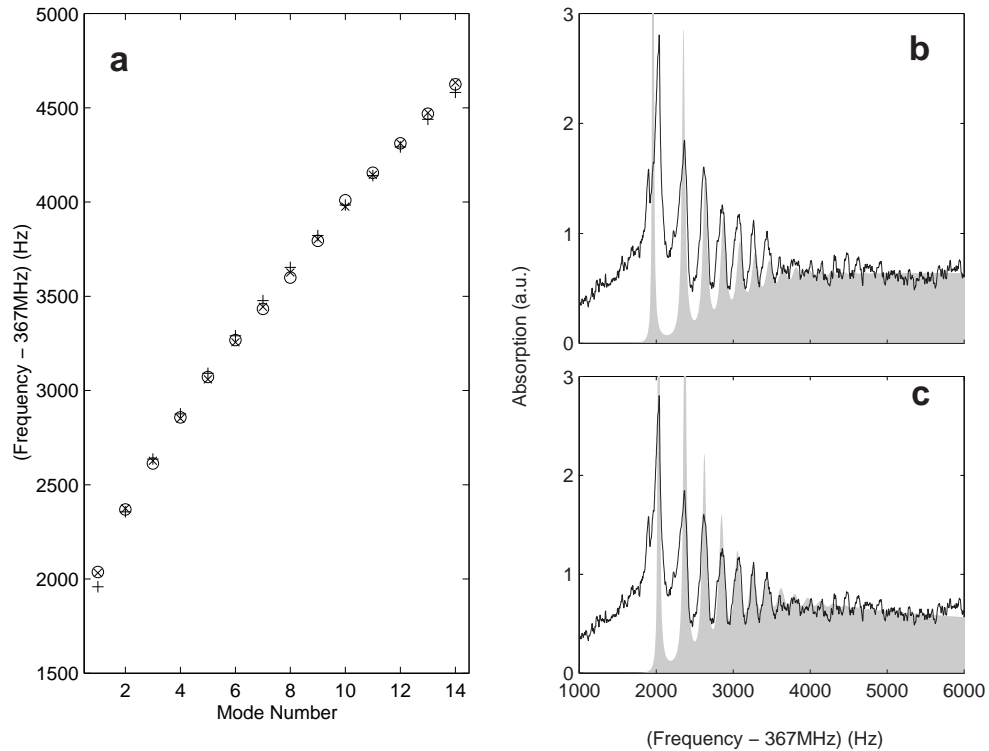


Figure 3.8: The linear model fitted to the peaks in a data spectrum. Data measured at 3.5mK with (nominal) 86mT/m applied gradient. Assuming a linear field profile, best fit to frequencies of first 14 peaks was $b_L = 10572$. When the quadratic term was included, best fit was $b_L = 5658$ and $b_2 = 0.23b_1$. (a) Experimental (\circ) and theoretical ($+$) frequencies. (b) Comparison between experimental (line) and theoretical (shaded) spectra with linear field. (c) Same as (b), using quadratic field profile, ignoring radial variation. Figure by Olivier Buu, re-produced from Buu *et al*[54].

See Appendix B for details of the NMR signal analysis. Data with $\log |h| \lesssim -2.5$ were usually rejected, as there was too much noise in the data, and too many uncertainties in the model. The phase was unwrapped manually, by adding units of 2π until the phase varied approximately linearly with $\log |h|$. The amplitudes were normalised by the initial FID signal. Data sets passed to the least-squares fitting routine were often small: 8 to 12 points, phase and amplitude information for each, along with waiting times. The manually added phase increments were removed, and then replaced in an automated way.

The operator method was used to simulate the magnetisation up to the π -pulse. After the π -pulse, for temperatures below 13mK the program used the eigenfunction method; above 13mK, μM_0 was sufficiently small that the eigenfunction orthogonality was violated, so the operator method was used instead. The penalty was that

the operator method is computationally slower than the eigenfunction method, so fewer points in time were simulated, leading to possible small errors in picking the echo time, amplitude and phase.

The tipping and π -pulses lasted $3\mu\text{s}$ and $26\mu\text{s}$ respectively, with equal RF-field strengths (as in the experiment). The aspect ratio was assumed to be unity. The first order gradient was fixed $G_1 = 105\text{mT/m}$. The second order gradient was fixed for each fitting attempt, and attempts were made with $b_2/b_1 = 0, +0.1, +0.2$ excluding radial variation, and $b_2/b_1 = +0.1, +0.2$ including radial variation. The parameters passed to the model via the MATLAB fitting-routine `lsqcurvefit` were: logarithm of the dimensionless gradient $\log_{10} b_L$; logarithm of the spin-rotation parameter $\log_{10} |\mu M_0|$; offset in $\log |h|$; offset in ϕ . The logarithms make it possible to deal with a large parameter range, using one fitting algorithm.

Phase information from both data and simulation were treated identically. The values of $\log |h|$ data below 20mK were weighted by a factor of 10, to keep the phase and amplitude data on the same scales, so phase was not preferentially fitted. Above 20mK, there was no re-scaling of data. The delays were not fitted, as the uncertainties were too large, and the data too scattered, to be of use. However, the sign and approximate magnitude of the delays told us that we had the correct sign and approximate magnitude of second order gradient.

Comments on the Fitting Process

Data-fitting is as much of an art form as is it a science. The weighting of data is reasonable: keep $\log |h|$ about the same magnitude as ϕ , or else ϕ will have a disproportionate effect on the sum of squares of errors. The logarithmic scaling of parameters b_L and μM_0 is related more to the details of the minimisation algorithm `lsqcurvefit` than to the data itself.

The fitting of the spectra left us with a limited knowledge of the magnetic field variation, which we capture in just two parameters: G_1 and b_2/b_1 . Leaving out the radial factor in the spin-dynamics gives us more chance of obtaining a good fit, but also has no real physical basis, unless higher order gradients are present. Slightly smaller second order gradients were used for spin-echo fitting than for spectrum fitting, partly because of the scale of the echo-delay data, and partly because better fits were achieved with $b_2/b_1 \leq 0.2$. The first-order gradient was fixed at $G_1 = 105\text{mT/m}$ for all fits: a value which was a common result of early spin-echo fitting, where G_1 was a variable parameter, and is also consistent with the spectrum fitting.

One could have passed real and imaginary parts of the echo signal (instead of

phase and amplitude) to the fitting routine, but there is implicit information in ϕ if we assume that the echo phase must be monotonically increasing with time. The monotonic increase is lost if we do not add 2π s, i.e. if we take real and imaginary parts. The drawback is that, by automating the 2π increments, the phase becomes a discontinuous function of the parameters of the model. Therefore, least-squares minimisation is prone to breaking down.

The offset in phase is of course almost arbitrary, although it varied little from one data set to another. The offset in amplitude helps account for the difficulty in distinguishing the initial FID from the signal due to the RF-pulse. Such difficulty may be due to the somewhat arbitrary amount of the *dead-time* used (see Appendix B).

The whole fitting process took about a month (the data sets were already available). Each fit took a few hours, the optimisation was watched and re-started manually if the route taken seemed unreasonable. The fits above 40mK are unreliable, because there are very few data points: as few as 5 amplitude-phase pairs with $\log |h| \gtrsim -2$ at 100mK.

Example Results

A typical result of spin-echo fitting at a lower temperature (6.7mK) is presented in Fig. 3.9, and at higher temperature (39mK) in Fig. 3.10. For both figures the radial variations are excluded from the simulation; $b_2 = 0.1b_1$ and $G_1 = 105\text{mT/m}$ are fixed parameters.

3.6 Results: D_{\perp} and μM_0 vs T

The primary results of spin-echo fitting process were values of μM_0 and $b_L \propto \mu M_0 / D_{\perp}$ for each data set, i.e. at each temperature. Values were obtained for various second order field variations, at every temperature for which a data set was available. From the combination of μM_0 and b_L , the diffusion coefficient D_{\perp} was derived.

3.6.1 Transport parameters

The results of the spin-echo fitting (b_L and μM_0 as functions of temperature) are shown in Fig. 3.11 and Fig. 3.12. The derived result for D_{\perp} versus T is shown in Fig. 3.13. b_L , the combination of transport coefficients and the gradient defined in Eqn. (2.57), is expected to saturate when $\mu M_0 \gtrsim 1$, as μM_0 and D_{\perp} are expected to have

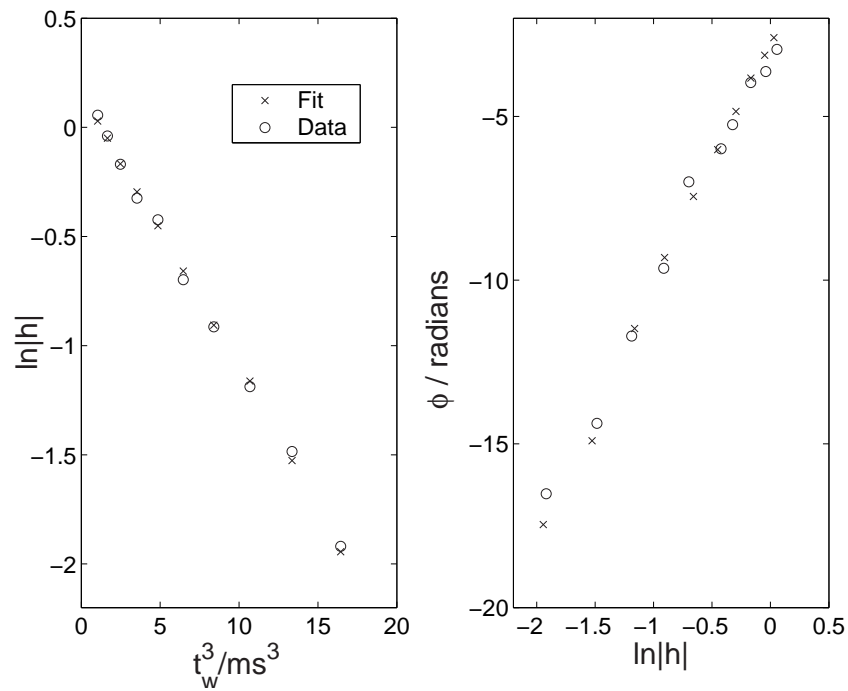


Figure 3.9: Example of Spin-Echo Fitting at 6.7mK. Data \circ , Fit \times . No radial variation used in simulation; $G_1 = 105\text{mT/m}$ and $b_2/b_1 = 0.1$ (fixed); $b_L = 11979$ and $\mu M_0 = -9.01$ (fitted).

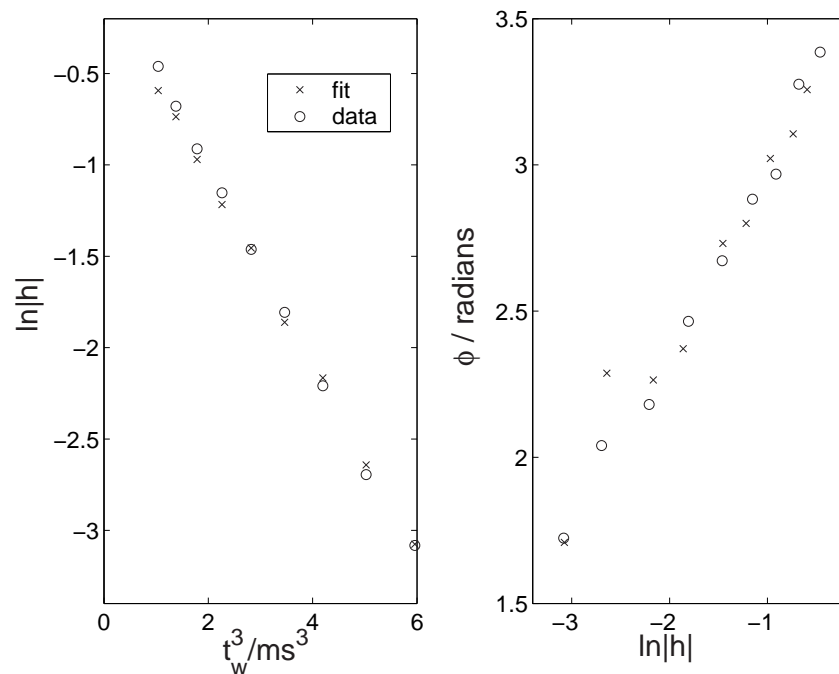


Figure 3.10: Example of Spin-Echo Fitting at 39mK. Data \circ , Fit \times . No radial variation used in simulation; $G_1 = 105\text{mT/m}$ and $b_2/b_1 = 0.1$ (fixed); $b_L = 9210$ and $\mu M_0 = -0.74729$ (fitted).

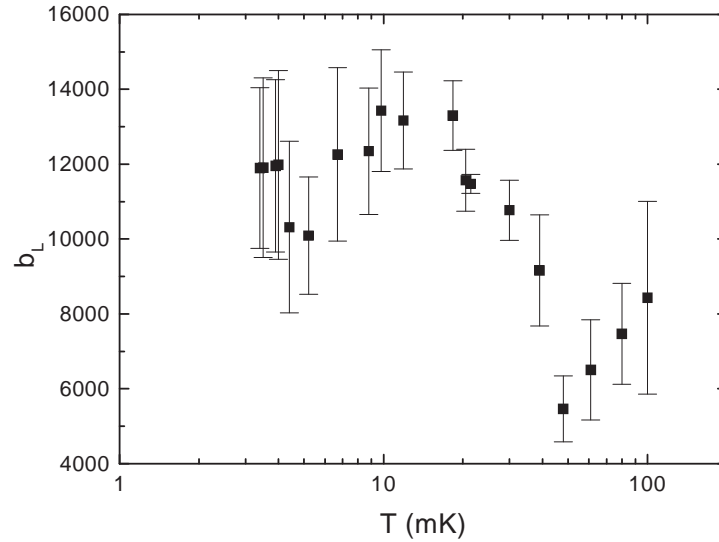


Figure 3.11: Results of Spin-Echo Fitting: b_{\perp} as a function of temperature.

the same dependence on τ_{\perp} , the lifetime of transverse-magnetisation elementary excitations.

The lines in Fig. 3.12 and Fig. 3.13 are results of a fit to the temperature variation predicted (χ^2 minimisation, counting error bars as one standard deviation, using `Origin`):

$$\mu M_0 = \frac{C_{\mu}}{T^2 + T_{a\mu}^2} \quad C_{\mu} = 760 \pm 100 \text{ mK}^2 \quad T_{a\mu} = (6.2 \pm 0.7) \text{ mK} \quad (3.7a)$$

$$D_{\perp} = \frac{C_D}{T^2 + T_{aD}^2} \quad C_D = 22 \pm 5 \text{ mK}^2 \text{ cm}^2 \text{ s}^{-1} \quad T_{aD} = (6.0 \pm 1.0) \text{ mK} \quad (3.7b)$$

$T_{a\mu}$ and T_{aD} are anisotropy temperatures associated with the spin-rotation and spin-diffusion coefficients.

3.6.2 Uncertainties in Results

Useful confidence limits can be placed on the results of our fits to formulae Eqn. (3.7a) and Eqn. (3.7b) because the uncertainties in the values of the transport coefficients have been carefully worked out. The least- χ^2 -fitting process returns a mean value for T_a and its uncertainty.

Temperature

The temperature for each data set is derived from a thermometer outside the cell, so there may be thermal effects mimicking a saturation of the transverse spin-transport lifetime, τ_{\perp} . Perhaps there are thermal gradients, but these are likely to be small:

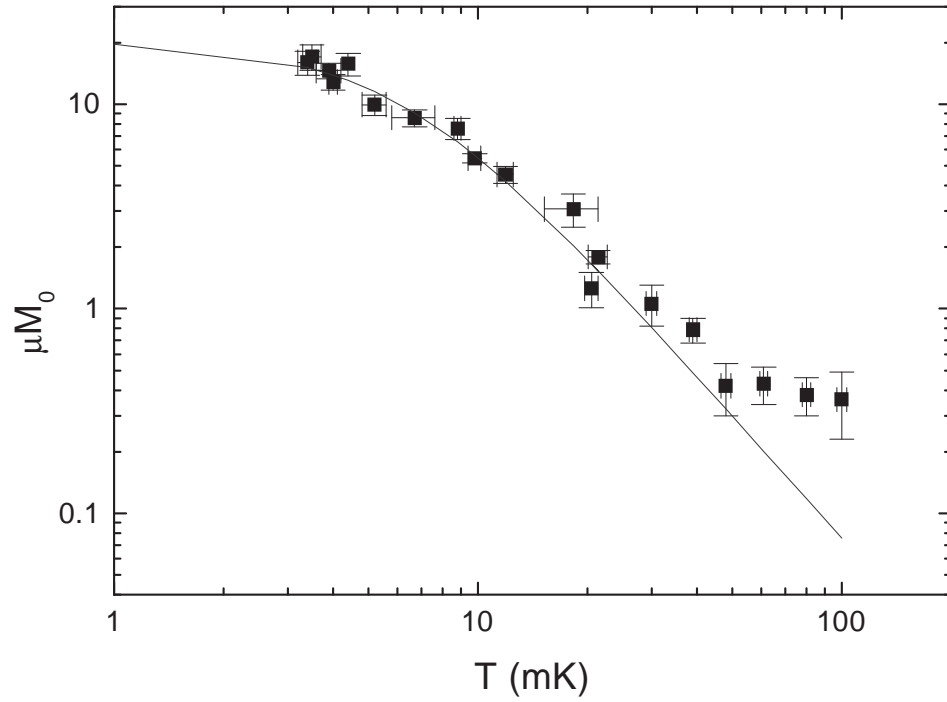


Figure 3.12: Results of Spin-Echo Fitting: μM_0 as a function of temperature. The line is a fit to the formula $\mu M_0 = \frac{C_\mu}{T^2 + T_{a\mu}^2}$, with $T_{a\mu} = 6.2 \pm 0.7 \text{mK}$

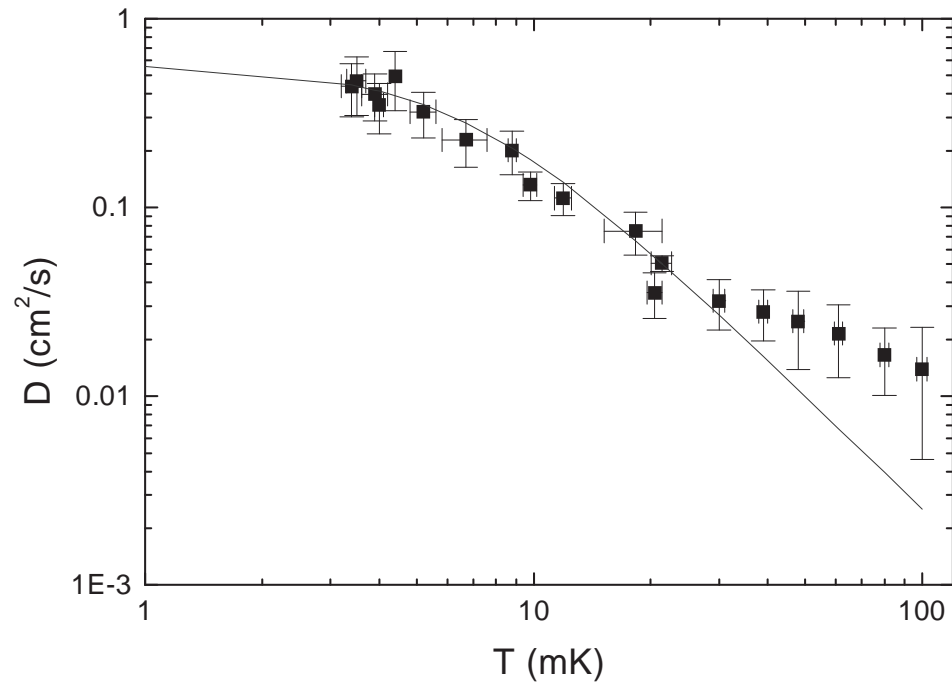


Figure 3.13: Results of Spin-Echo Fitting: D_\perp as a function of temperature. D_\perp is derived from μM_0 and b_L Fig. 3.11 and Fig. 3.12. The line is a fit to the formula $D_\perp = \frac{C_D}{T^2 + T_{aD}^2}$, with $T_{aD} = 6.0 \pm 1.0 \text{mK}$

heat leaks are small, and time is allowed between experiments to reach thermal equilibrium.

The π -pulse adds energy by inverting the magnetisation, away from equilibrium, but the energy involved thermalises on a timescale approximately T_1 , which is much, much longer than the duration of an experiment. The time between experiments is sufficient for thermal equilibrium to be reached; however, the temperature of nuclear adiabatic demagnetisation stage drifts slowly between experiments, due to the energy deposited by the pulses. The NMR pulses can cause transient heating of the helium directly, as discussed by Ragan *et al*[73]. A graph of the temperature increased due to such a mechanism is shown in Buu *et al*[53]. At the lowest temperature, 3.5mK, the effect is 0.4mK; at higher temperatures the heating is negligible.

The dominant part of the uncertainty in temperature is the slow drift between experiments, with some additional effect from NMR pulse-heating at the lowest temperatures. These two effects are combined in the error bars in Fig. 3.11, Fig. 3.12 and Fig. 3.13.

μM_0 and D_\perp

The values of μM_0 are the result of the fitting process already described. The error bars are the upper and lower bounds of the values fitted using the different second order gradients (with and without radial variations); the points are the mean of the set of values fitted, at each temperature. The same process determines the errors and values of b_L . The diffusion coefficient D_\perp is found from formula Eqn. (2.57); the error bars are the combination of errors in μM_0 and b_L .

3.6.3 Discussion

Both spin-transport coefficients μM_0 and D_\perp , increase with decreasing temperature.

At high temperature neither coefficient follows a Fermi-liquid $1/T^2$ law. One expects deviations from $1/T^2$ above about $T_F/10^\dagger$: for the 6.2% ³He-⁴He mixture, the Fermi temperature is $T_F = 410\text{mK}$, so deviations should occur above about 40mK. Also, the phase variation in the echoes above about 40mK are very small (μM_0 is small), so any other effect which changes the phase may overwhelm the spin-rotation effect: the demagnetising field is a candidate. The quality of the fit deteriorates at high temperature. The high temperature values of the spin-transport coefficients differ from the measurements published by, for example Ager *et al*[28]

[†]A very approximate rule-of-thumb, of unknown origin: perhaps Ref. [5]. Data on viscosity of ³He-⁴He mixtures seems to agree: See Refs. [12][13][14] (and Fig. 1.3)

and Ishimoto *et al*[27], by about 25% (see Buu *et al*[53] for details). The differences may be due to finite-size effects.

At low temperature, below about 30mK, our results follow the curve fits to the formula Eqn. (3.7a) and Eqn. (3.7b); the results show substantial deviation from the $1/T^2$ law. The value of the *anisotropy temperatures* derived from the two transport parameters agree well with each other, to within one standard deviation. The combined value for the anisotropy temperature to be quoted is $(6 \pm 1)\text{mK}$.

The value of T_a should be compared with other experiments: see Table 3.1. Our result falls below that of most other spin-echo experiments, but above the spin-wave damping experiment of Vermeulen and Roni[43]. The result is greater than the theoretical prediction of Jeon and Mullin[21][16], but cannot be strictly compared, as their theory is valid for extremely dilute mixtures only.

CHAPTER 4

THE DEMAGNETISING FIELD AND TRANSVERSE SPIN-TRANSPORT

The *demagnetising field* is the magnetic field due to the magnetisation of the sample being studied and is sometimes known as the dipolar field. In this chapter it will be shown how the demagnetising field can be included in the linear model of spin-dynamics in a Fermi-liquid. Some results of calculations using the model will be presented: spectra, FIDs and the effects of the demagnetising field on the eigenmodes themselves.

Other groups have studied the effects of the demagnetising field with restricted applicability: Krotkov *et al*[79] derived the equation of motion suitable for ^3He and perturbative solutions; Walker[80] and Joseph and Schlömann[81][82] studied magnetostatic modes in a ferromagnet; Nacher *et al*[83][84] developed a model using a finite number of spins with periodic boundary conditions; and Jeener [85] solved for a very small number of fixed spins. All included the demagnetising field in their models, but such models cannot be directly compared to experiments in Fermi-liquid ^3He . The model of this chapter can be applied to such experiments if the tipping angle is sufficiently small, and the basis set is sufficiently large.

4.1 Equation of Motion

The linearised equation of motion for magnetisation including the demagnetising field and the Leggett-Rice effect was derived by Krotkov *et al* (Ref. [79] equations

(2)–(40)). Presented here is an alternative derivation due to RM Bowley.

The magnetic field \mathbf{H}_0 is to be augmented by the two terms of the demagnetising field: \mathbf{H}_d due to the static equilibrium magnetisation, in the z -direction and smaller than \mathbf{H}_0 by a factor of χ the susceptibility[†]; and \mathbf{h} due to the non-equilibrium magnetisation in the xy -plane, which is smaller still by a factor of about $\sin\theta$; θ is the tipping angle. One substitutes $(\mathbf{H}_0 + \mathbf{H}_d + \mathbf{h})$ for \mathbf{H}_0 into equation Eqn. (1.22), remembering that $\mathbf{\Omega}_0 = \gamma\mu_0\mathbf{H}_0$. Assuming that the equilibrium magnetisation is uniform and unvarying with time, the linearised vector equation describing the magnetisation is:

$$\frac{\partial \mathbf{m}}{\partial t} - \gamma\mu_0(\mathbf{m} \times (\mathbf{H}_0 + \mathbf{H}_d) - \mathbf{M}_0 \times \mathbf{h}) = \frac{D_0}{1 + \mu^2 M_0^2} (1 + \mu \mathbf{M}_0 \times) \nabla^2 \mathbf{m} \quad (4.1)$$

The above equation can be directly compared with Eqn. (2.4). The next two steps are then straightforward (take components, form complex numbers like $h_{\pm} = h_x \pm ih_y$).

$$\frac{\partial m_{\pm}}{\partial t} = \mp i\gamma\mu_0\{m_{\pm}(H_0 + H_d) + M_0 h_{\pm}\} + \frac{D_0}{(1 \mp i\mu M_0)} \nabla^2 m_{\pm} \quad (4.2)$$

The remaining task is to find both \mathbf{H}_d and \mathbf{h} .

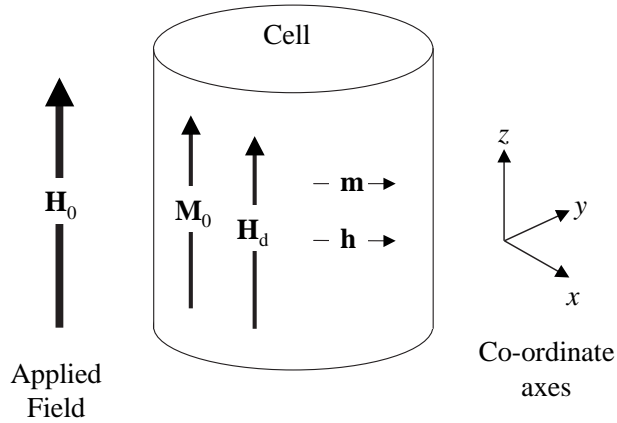


Figure 4.1: Diagram showing terms in demagnetising field. \mathbf{M}_0 is the equilibrium magnetisation; \mathbf{H}_d is the associated demagnetising field. \mathbf{m} is non-equilibrium magnetisation, and \mathbf{h} the associated demagnetising field.

The demagnetising field can be found by solving Maxwell's equations in the quasi-static limit (time derivatives are zero) when there is no electric current:

$$\nabla \cdot \mathbf{B} = \mu_0 \nabla \cdot (\mathbf{H}_0 + \mathbf{H}_d + \mathbf{h} + \mathbf{M}_0 + \mathbf{m}) = 0 \quad \text{and} \quad \nabla \times \mathbf{H}_d = 0 \quad (4.3)$$

[†] χ is very much less than one for a non-ferromagnet, typically about 10^{-6} for liquid ^3He

The equilibrium case is studied first ($\mathbf{m} = \mathbf{h} = 0$) in section 4.1.1; then the non-equilibrium case, section 4.1.2. Fig. 4.1 is a schematic diagram showing the terms used in the derivation of the demagnetising field.

4.1.1 Demagnetising Field Due to Equilibrium Magnetisation

This subsection is a derivation of the demagnetising field \mathbf{H}_d due to the static, equilibrium magnetisation. The very small terms in \mathbf{H}_d which are transverse to the z -axis are ignored. \mathbf{H}_d can be considered as a perturbation to the applied field, \mathbf{H}_0 , whose transverse terms are ignored as they are second order in smallness, of order χ^2 .

Definition

Fourier transform and inverse Fourier transform of a vector quantity, \mathbf{A}

$$\tilde{\mathbf{A}}(\mathbf{k}) = \int d^3\mathbf{r} e^{-i\mathbf{k}\cdot\mathbf{r}} \mathbf{A}(\mathbf{r}) \quad (4.4)$$

$$\mathbf{A}(\mathbf{r}) = \frac{1}{(2\pi)^3} \int d^3\mathbf{k} e^{i\mathbf{k}\cdot\mathbf{r}} \tilde{\mathbf{A}}(\mathbf{k}) \quad (4.5)$$

In Eqn. (4.3), the non-equilibrium terms are set to zero:

$$\nabla \cdot \mathbf{B} = \mu_0(\nabla \cdot \mathbf{H}_d + \nabla \cdot \mathbf{M}_0) = 0 \quad \text{and} \quad \nabla \times \mathbf{H}_d = 0 \quad (4.6)$$

The Fourier transforms of Eqn. (4.6) are:

$$\mathbf{k} \cdot \tilde{\mathbf{H}}_d + \mathbf{k} \cdot \tilde{\mathbf{M}}_0 = 0 \quad \text{and} \quad \mathbf{k} \times \tilde{\mathbf{H}}_d = 0 \quad (4.7)$$

Therefore:

$$\tilde{\mathbf{H}}_d(\mathbf{k}) = - \left(\frac{\mathbf{k} \cdot \tilde{\mathbf{M}}_0(\mathbf{k})}{k^2} \right) \mathbf{k} \quad (4.8)$$

Using the fact that $\mathbf{M}_0(\mathbf{r}) = M_0 \hat{\mathbf{z}}$ is along the z -direction, the z -component is:

$$\left(\tilde{\mathbf{H}}_d(\mathbf{k}) \right)_z = - \left(\frac{\hat{\mathbf{z}} \cdot \tilde{\mathbf{M}}_0(\mathbf{k})}{k^2} \right) k_z^2 = - \frac{\tilde{M}_0(\mathbf{k}) k_z^2}{k^2} \quad (4.9)$$

In real space:

$$\left(\mathbf{H}_d(\mathbf{r}) \right)_z = + \frac{1}{(2\pi)^3} \frac{\partial^2}{\partial z^2} \int d^3\mathbf{k} e^{i\mathbf{k}\cdot\mathbf{r}} \frac{\tilde{M}_0(\mathbf{k})}{k^2} \quad (4.10)$$

Substituting the Fourier transform of $1/k^2$, which is $1/4\pi|\mathbf{r} - \mathbf{r}'|$, and using the real space version of M_0 :

$$H_d = \left(\mathbf{H}_d(\mathbf{r}) \right)_z = + \frac{1}{4\pi} \frac{\partial^2}{\partial z^2} \int d^3\mathbf{r}' \frac{M_0(\mathbf{r}')}{|\mathbf{r} - \mathbf{r}'|} \quad (4.11)$$

Krotkov *et al*[79] define the demagnetising field operator:

$$\hat{n}_{zz}[f(\mathbf{r})] = - \frac{1}{4\pi} \frac{\partial^2}{\partial z^2} \int d^3\mathbf{r}' \frac{f(\mathbf{r}')}{|\mathbf{r} - \mathbf{r}'|} \quad (4.12)$$

Assuming the equilibrium magnetisation is a constant M_0 :

$$H_d = -M_0 \hat{n}_{zz}[1] \quad (4.13)$$

4.1.2 Demagnetising Field Due to Non-Equilibrium Magnetisation

The quantities related to the equilibrium magnetisation (\mathbf{H}_0 , \mathbf{M}_0 and \mathbf{H}_d) can be subtracted from the full Maxwell equations Eqn. (4.3), and we now solve for the non-equilibrium quantities: $\nabla \cdot \mathbf{h} + \nabla \cdot \mathbf{m} = 0$ and $\nabla \times \mathbf{h} = 0$, Fourier transform, and solve:

$$\tilde{\mathbf{h}}(\mathbf{k}) = - \left(\frac{\mathbf{k} \cdot \tilde{\mathbf{m}}(\mathbf{k})}{k^2} \right) = - \left(\frac{k_x \tilde{m}_x(\mathbf{k}) + k_y \tilde{m}_y(\mathbf{k})}{k^2} \right) \mathbf{k} \quad (4.14)$$

since \mathbf{m} is in the xy -plane. We would prefer these equations to be cast into a single, complex number; the h_- representation is arbitrarily chosen, multiplied by $e^{i\Omega_0 t}$ and any terms oscillating at or faster than the Larmor frequency (h_+ , m_+) rapidly time-average to zero.

$$h_-(\mathbf{r}) = - \frac{1}{(2\pi)^3} \int d^3\mathbf{k} e^{i\mathbf{k} \cdot \mathbf{r}} \left(\frac{k_x \tilde{m}_x + k_y \tilde{m}_y}{k^2} \right) (k_x - ik_y) \quad (4.15)$$

$$= - \frac{1}{(2\pi)^3} \int d^3\mathbf{k} e^{i\mathbf{k} \cdot \mathbf{r}} \left(\frac{k_x^2 + k_y^2}{2k^2} \right) \tilde{m}_- \quad (4.16)$$

Then, put

$$\frac{k_x^2 + k_y^2}{2k^2} = \frac{1}{2} - \frac{k_z^2}{2k^2} \quad (4.17)$$

then differentiate the integral, as in Eqn. (4.10), apply the convolution theorem, and use the definition Eqn. (4.12) of the demagnetising field operator:

$$h_-(\mathbf{r}) = + \frac{1}{2} m_-(\mathbf{r}) - \frac{1}{2} \hat{n}_{zz}[m_-(\mathbf{r})] \quad (4.18)$$

The result is the demagnetising field to be substituted into (4.1).

For completeness, the solution relating to the opposite-rotation reference-frame is $h_+ = -\frac{1}{2} m_+ + \frac{1}{2} \hat{n}_{zz}[m_+]$

4.1.3 Linearised equation of motion

The final, linearised form of the equation of motion is to be found by substituting Eqn. (4.13) and Eqn. (4.18) into Eqn. (4.2):

$$\begin{aligned} \frac{\partial m_-}{\partial t} = & \frac{D_0}{(1 + i\mu M_0)} \nabla^2 m_{\pm} \\ & + i \left\{ \Omega_0(\mathbf{r}) m_- - \gamma \mu_0 M_0 \hat{n}_{zz}[1] m_- + \gamma \mu_0 M_0 \frac{1}{2} (m_- - \hat{n}_{zz}[m_-]) \right\} \end{aligned} \quad (4.19)$$

Collecting together terms, and defining the demagnetising frequency ω_M :

$$\begin{aligned} \frac{\partial m_-}{\partial t} = & \left\{ + i\Omega_0(\mathbf{r}) + \frac{D_0}{(1 + i\mu M_0)} \nabla^2 \right\} m_- \\ & + i \frac{1}{2} \omega_M \left\{ (1 - 2\hat{n}_{zz}[1]) m_- - \hat{n}_{zz}[m_-] \right\} \end{aligned} \quad (4.20)$$

$$\omega_M = \gamma \mu_0 M_0 \quad (4.21)$$

The last term in the equation of motion $-i\frac{1}{2}\omega_M\hat{n}_{zz}[m_-]$ is non-local; the equation is integro-differential, rather than purely differential. In cylindrical co-ordinates, even if Ω_0 contains terms only second or lower order, the equation is not separable into radial and axial terms. The equation of motion remains complex symmetric, as in the terms of Appendix A.

4.1.4 Frequency Scales

To understand the physical consequences of the equation of motion (also to assist in programming), it proves useful to convert the coefficients of each term into frequency scales, and to then use dimensionless units. There are four such frequency scales used in this thesis: the demagnetising field scale, ω_M of Eqn. (4.21); the effective diffusion frequency scale, ω_D of Eqn. (2.42); and frequency variations due to first and second order field inhomogeneities, ω_{G_1} and ω_{G_2} :

$$\omega_M = \gamma \mu_0 M_0 \quad (4.22a)$$

$$\omega_D = D_{\text{eff}}/L^2 \quad (4.22b)$$

$$\omega_{G_1} = \gamma G_1 L \quad (4.22c)$$

$$\omega_{G_2} = \gamma G_2 L^2 \quad (4.22d)$$

Re-writing Eqn. (4.20) in frequencies, using dimensionless units spatial units but real time units, and subtracting the central Larmor frequency:

$$\begin{aligned} \frac{\partial m_-}{\partial t} = & \left\{ + i(\omega_{G_1} \zeta + \omega_{G_2} (\zeta^2 - \frac{1}{2} \rho^2)) + \omega_D \nabla^2 \right\} m_- \\ & + i \frac{1}{2} \omega_M \left\{ (1 - 2\hat{n}_{zz}[1]) m_- - \hat{n}_{zz}[m_-] \right\} \end{aligned} \quad (4.23)$$

The time co-ordinate can be made dimensionless by dividing through by ω_D [†].

Whichever frequencies are largest should dominate the dynamics. Sharp peaks are expected if the demagnetising field is larger than either the inhomogeneous broadening or the diffusion. If the gradient is large a broad spectrum is expected, possibly with peaks from the Leggett-Rice effect. If the diffusion frequency is largest, motional narrowing is likely, giving just one sharp peak.

Another view of the dynamics, based on length scales (in the absence of the demagnetising field) is given by Buu *et al*[54]. There is a de-phasing scale $L_g = (|D_{\text{eff}}|/\gamma G_1)^{1/3}$; a time-dependent diffusion scale $L_d = (|D_{\text{eff}}|t)^{1/2}$; and the length of the cell $2L$. Short waiting-time echo experiments have L_d very small and are in the free-diffusion regime, where Leggett's formulae are valid. When the cell length $2L$ is smallest, motional narrowing is dominant (long time scale, fast diffusion). When the de-phasing length is smaller than the other length scales, then the dynamics are characterised by localisation of magnetisation.

4.1.5 Matrix Formulation

The same techniques can be applied to solve the linearised equation of motion as for the equation without demagnetising field, so a matrix form for each of the three terms proportional to ω_M is to be derived. One term is trivial (the identity matrix), and the other two are described in Appendix C. The work therein is almost entirely due to RM Bowley and Olivier Buu, and is included for completeness. The most important point is that the equation is non-separable, so the basis functions must be combinations of axial and radial functions, put together into a single, larger matrix.

Formulae for the matrix elements are given in Appendix C, but the final equations must be integrated numerically. The integrations were performed using the MATLAB function `dblquad`. A basis set of 50 axial functions ($n = 0$ to 49) and 9 Bessel functions ($l = 0$ to 8) was used; the time to compute the matrix elements was 19 days, on a 1300MHz PC running Windows98. It is not expected that a such a basis set will be large enough to represent real experiments: in the previous data analysis, typically a 130 by 30 (axial by radial) basis functions were used, which would require 1400 days computation for the demagnetising field matrices. Also, a matrix of 150 axial basis functions and only the uniform radial basis functions was calculated, taking about four days. The matrices are real and symmetric, so the properties of the pseudo-hamiltonian are unchanged by the addition of the demagnetising field.

[†]The dimensionless gradients are $b_1 = \omega_{G_1}/\omega_D$ and $b_2 = \omega_{G_2}/\omega_D$

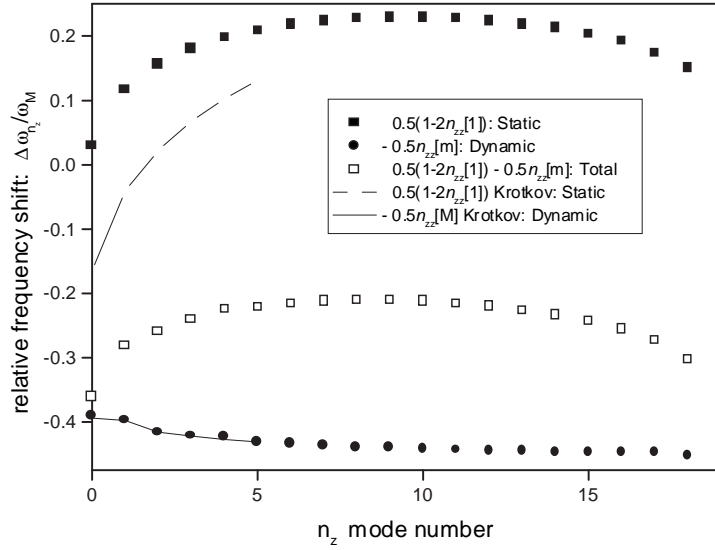


Figure 4.2: Perturbative comparison with Krotkov *et al.*: The shifts due to a very small demagnetising field were simulated, then normalised by that demagnetising field. The values from Ref. [79] were taken from Table II and Eqn. (56). The dimensionless first order gradient was $|b_1| = 10^3$.

The matrix tabulation code was mainly written Olivier Buu: my role was debugging and running, then building the results into a simulation to extract physical results.

Comparison with Work of Krotkov *et al*

Since no other group has performed the demagnetising-field matrix calculation directly, we have tested a subset of the solutions against the perturbation theory of Krotkov *et al*[79]. A (probably typographical) correction to one of their formula was found (by Olivier Buu), and is included in the calculation of Fig. 4.2. Excellent correspondence between the two methods is found for the dynamic part, and the static parts approximately agree except for an overall shift. We have no clear explanation for the shift, although it may be related to the approximations made by Krotkov *et al*. The combined effect of the two ends of the cell is expected to cause the results of the two methods to differ except for the first five or six modes.

4.1.6 Spatial Variation of Demagnetising Field

Physical insight into the effects of the demagnetising field can be gained by plotting the spatial variation of the static part, $\hat{n}_{zz}[1]$. The spatial variation can be derived by considering the expansion of the Green's function $1/|\mathbf{r} - \mathbf{r}'|$ in terms of cylindrical

Bessel functions, as in Eqn. (C.1). The static term can be split into two terms, as shown in section C, Eqn. (C.3) and Eqn. (C.4). The results are two triple integrals, the spatial parts of which (ζ', ρ') are analytically solvable, using the relations of the Bessel functions (Ref. [55], Eqn. 9.1.27):

$$\int_0^1 \rho' d\rho' J_0(k\rho') = \frac{J_1(k)}{k} \quad (4.24)$$

Therefore, the static part of the demagnetising, as a function of space, is given by a single integral:

$$\hat{n}_{zz}[1](\zeta, \rho) = \int_0^\infty dk J_0(k, \rho) J_1(k) \left\{ 1 - \frac{1}{2} [2 - e^{-\alpha k(\zeta+1)} - e^{-\alpha k(1-\zeta)}] \right\} \quad (4.25)$$

The integral is performed numerically, and the result is plotted in the left-hand panel of Fig. 4.3, on a grid of 41 axial positions by 21 radial positions. The middle panel is a representation of the second order field variation, scaled and shifted to be on the same scale as the demagnetising field. The difference between the two is shown in the right-hand panel. The static demagnetising field is a second order field variation (of magnitude roughly equivalent to $-\omega_M/3.6$) with some higher order terms, particularly near the outer edge of the cell ($\rho = 1$).

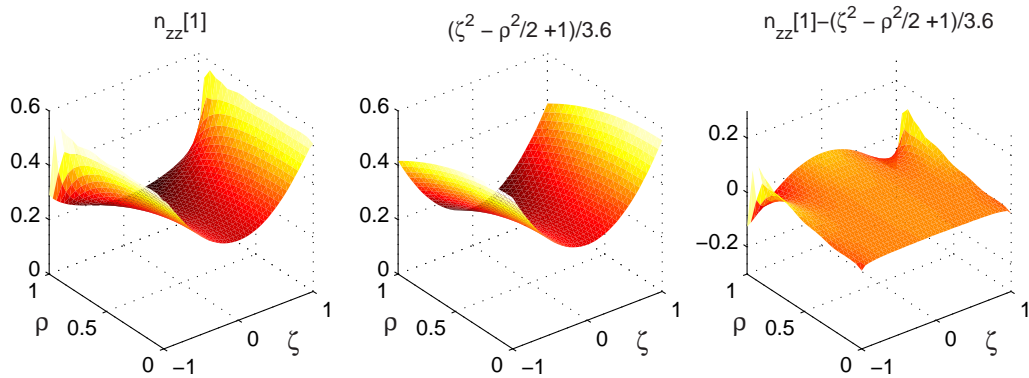


Figure 4.3: Demagnetising Field: Spatial Variation of Static Part

4.2 FIDs

It was necessary to re-write the simulation code to use the un-separated axial/radial basis set (not a trivial exercise), compare the new code with the old separated-bases code, and also tabulate the demagnetising-field matrices. It was then a simple matter to produce simulations of FIDs, spectra and spin-echo experiments, as well as study the damping, shifts and spatial variations of the eigenmodes.

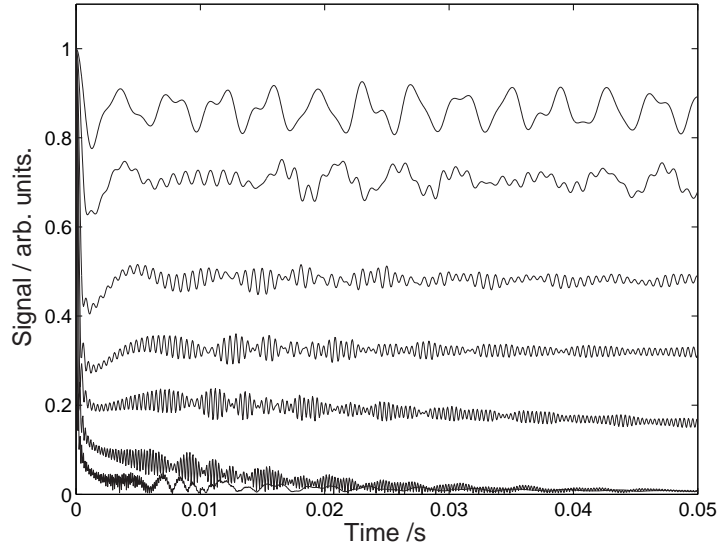


Figure 4.4: Simulation of Effect of the demagnetising field on FIDs: Inputs to the model are: $L = 2.3\text{mm}$, $f_M = 1100\text{Hz}$, $D_{\perp} = 1 \times 10^{-5}\text{m}^2\text{s}^{-1}$, $\mu M_0 = 15$. The first order gradients are zero (top curve), 10, 20, 30, 40, 60, and 100mT/m. The signals have not been offset. The gyromagnetic ratio is that of ^3He nuclei. Radial variations are ignored in this simulation, and there is no second order gradient. Beats can be seen indicating the presence of a few, long-lived eigenmodes.

Conceptually, the simplest simulations are of FID signals, some of which are presented in Fig. 4.4. When the gradient is large, the FID is much as if there were no demagnetising field: rapid decay, then a few beats of Leggett-Rice modes. When there is little or no field inhomogeneity, most of the signal is very long-lived. There is a smooth transition between two regimes, which are demagnetising-field (signal mostly long-lived) or field-inhomogeneity dominated (short-lived signal).

The FIDs yield less information than the spectra, although it is clear that there are long-live eigenmodes, which should show up as sharp peaks in the spectra.

4.3 Spectra

4.3.1 Varying ω_M

The effect of the demagnetising field is clearly demonstrated in Fig. 4.5 and Fig. 4.6 (respectively $\mu M_0 = 0$ and $+7$). The most obvious effect is known as *spectral clustering*, see for example Jeener[85]: when the demagnetising field is large, the spectrum is dominated by one large peak (or several peaks if the damping due to diffusion is sufficiently small, as in Fig. 4.6). The broad background due to inhomogeneous broadening is lost. A weaker demagnetising field makes the spectrum

asymmetric, a similar effect to second- and higher-order field inhomogeneities.

Fig. 4.6, with $\mu M_0 = 7$ shows that the peaks associated with Leggett-Rice spin-wave modes (on the left) disappear to be replaced by demagnetising-field modes (on the right). When ω_M and μM_0 are have opposite signs, the peaks are on the same side of the spectrum and thus the transition is less clear.

The spectrum shifts bodily because of the homogeneous part of the demagnetising field associated with the transverse magnetisation, Eqn. (4.18). Further movements of peaks relative to one another are due to the inhomogeneous terms, mathematically described by either $\hat{n}_{zz}[1]$ or $\hat{n}_{zz}[m]$.

A closer look at Fig. 4.6 makes it clear that the peaks are split for large ω_M , an effect caused by the radial inhomogeneity in the demagnetising field (break a symmetry, break a degeneracy). For the parameters of Fig. 4.5 and Fig. 4.6, there are about three sub-peaks per main peak, implying at least six radial basis functions are required (nine are used in the production of the figures).

The demagnetising field strength at which the crossover-occurs from inhomogeneous broadening to the demagnetising-field dominated regime is when $f_M \simeq f_{G_1}$. Leggett-Rice peaks are perturbed, and degeneracy is lifted (peaks are split) at even lower demagnetising field, i.e. when $f_M \simeq \Delta f$, the demagnetising field is just a few times the inter-mode frequency shift[†].

4.3.2 Varying ω_{G_1}

In Fig. 4.7 and Fig. 4.8, $\Delta f = (f_{G_1}^2 f_D)^{1/3}$ varies from zero to 28.3Hz, always much less than f_M . Therefore the demagnetising field cannot be treated as a perturbation to the applied magnetic field inhomogeneity. When there is no applied field inhomogeneity, the width of the spectrum is set by the demagnetising field frequency scale; increasing the gradient makes the spectrum broader, and reduces spectral clustering.

4.3.3 Shift and Split: an interesting observation

Fig. 4.9 is an example of more subtle behaviour. The main figure demonstrates the splitting of a mode (and the associated peak in the spectrum) when a small gradient is introduced (f_{G_1} in the figure varies from zero to 56Hz). Such splitting increases with increasing gradient, until peaks cross one another, in a non-perturbative manner. It is worth knowing that $|f_D| = 0.08\text{Hz}$, so $\Delta f \leq 6.3\text{Hz}$, always much smaller than f_M .

[†]In Fig. 4.5 $\Delta f/f_{G_1} = 0.1$; in Fig. 4.6 $\Delta f/f_{G_1} = 0.052$.

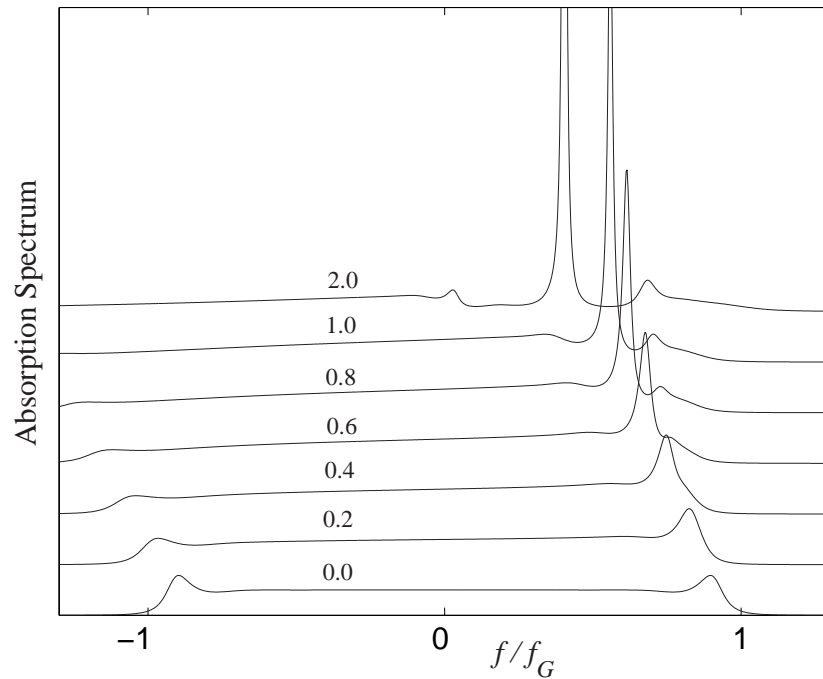


Figure 4.5: Simulated spectra showing effect of demagnetising field: Calculated using m_+ not m_- . Frequency normalised by $f_{G_1} = 1000\text{Hz}$. $|f_D|/f_{G_1} = 0.001$; $\mu M_0 = 0$; f_M/f_{G_1} shown next to each curve. Spectra are shifted vertically for clarity.

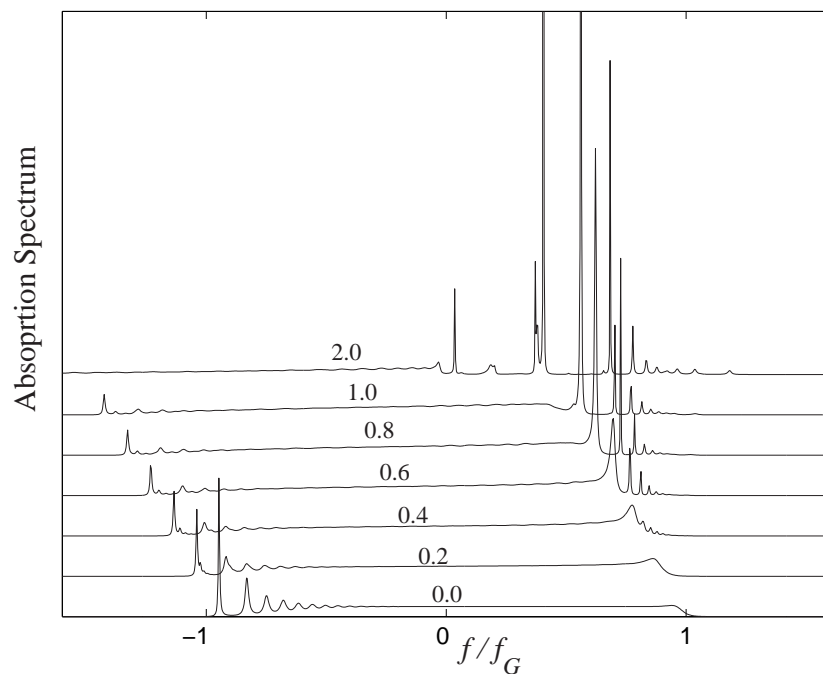


Figure 4.6: Simulated spectra, with demagnetising field. Exactly the same as Fig. 4.5, but $\mu M_0 = 7$ and $|f_D|/f_{G_1} = 1.41 \times 10^{-4}$.

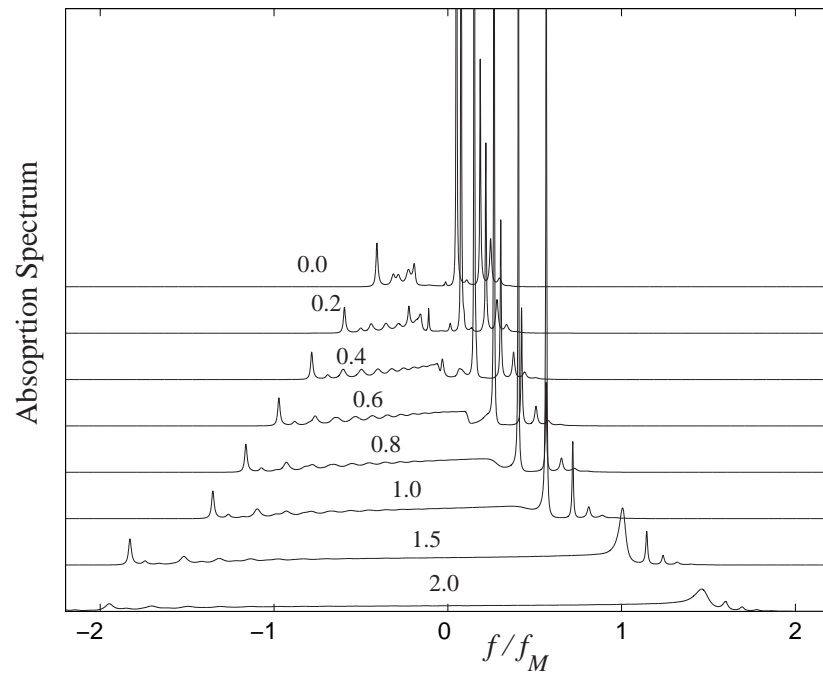


Figure 4.7: Simulated spectra showing effect of demagnetising field: Calculated using m_+ . Frequency normalised by $f_M = 200\text{Hz}$. $f_D = 0.14\text{Hz}$; $\mu M_0 = +7$; f_{G_1}/f_M ; shown next to each curve. Spectra are shifted vertically for clarity.

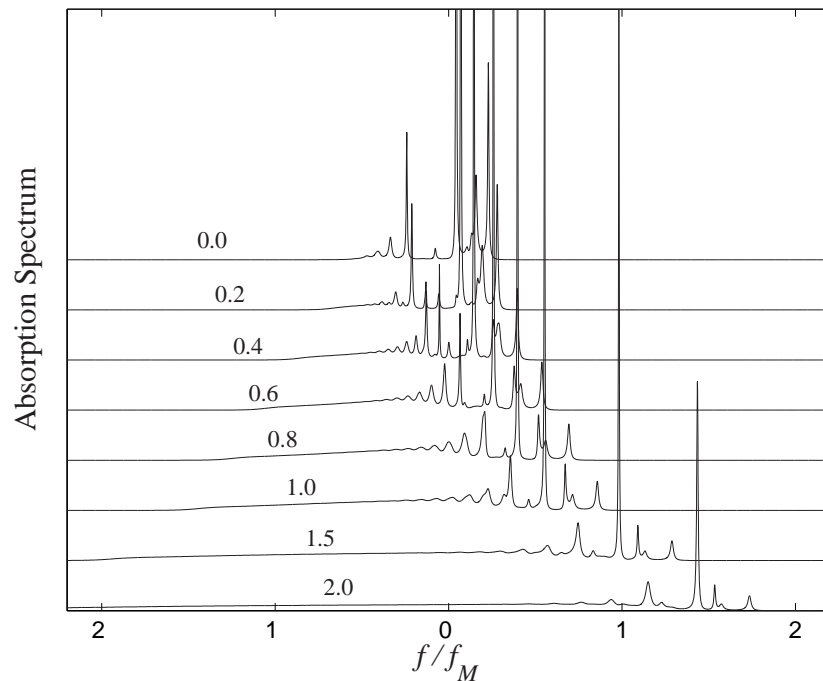


Figure 4.8: Spectra, with demagnetising field. Exactly the same as Fig. 4.7, but $\mu M_0 = -7$.

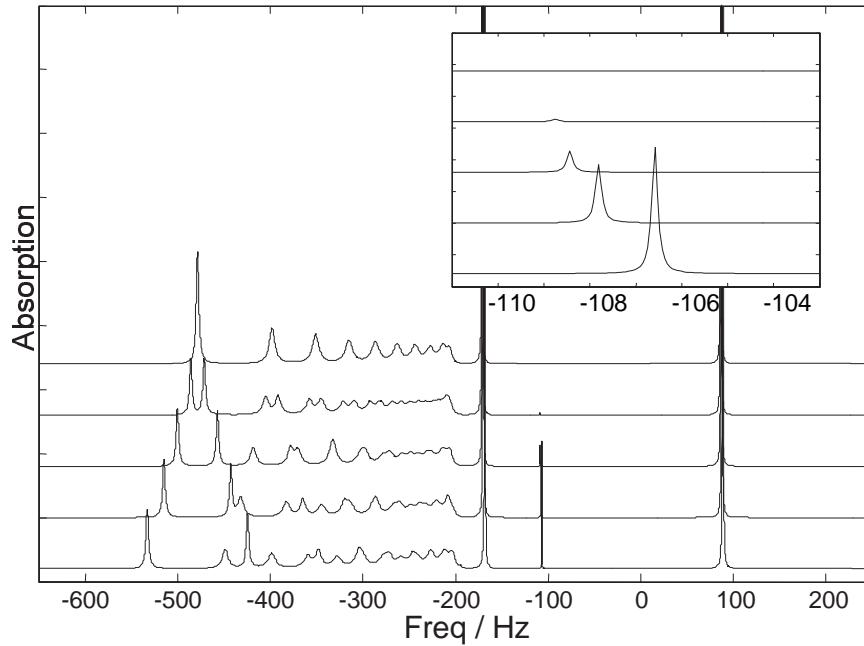


Figure 4.9: Shift and split of peaks as gradient is increased, for fixed demagnetising field. Calculated using m_- . $f_M = 1100\text{Hz}$. $D_\perp = 10^{-5}\text{m}^2/\text{s}$; $\mu M_0 = 15$; $L = 1.15\text{mm}$. Spectra are shifted vertically for clarity. Gradients are 0, 0.2, 0.6, 1, 1.5 mT/m (from top to bottom).

In addition a peak appears at around -109Hz , becomes larger and shifts slightly as the gradient is increased. The explanation is that there is an eigenmode present even when there is no applied gradient, but the mode is exactly antisymmetric, so it is not detected. When a small gradient is applied, the eigenmode shifts off-centre (hence the frequency shift) and becomes asymmetric (hence the overlap with the detector increases, as does the amplitude in an FID/spectroscopy experiment).

4.3.4 The Demagnetising Field and Shimming

In a spectroscopic experiment, the demagnetising field appears much like a second order gradient (or perhaps higher order), as can be seen in Fig. 4.6 to Fig. 4.8, breaking degeneracy because of the radial variation. In Fig. 4.10, it is shown that the demagnetising field and the second order gradient can almost cancel. Also, the pure- G_2 spectrum is strongly asymmetric, but the demagnetising-field dominated spectrum is nearly symmetric.

Imagine trying to shim the applied field when the demagnetising field is present (assume that the linear gradient has been cancelled). Minimising the line-width would occur not when $G_2 = 0$, but when $f_M \simeq -3f_{G_2}$, since the static part of the demagnetising field approximately corresponds to just such a second order gradient

of about that magnitude (see section 4.1.6, Fig. 4.3). Therefore, the best guess at shimming would leave second-order terms in the applied magnetic field, leading to side-peaks in a spectrum if you were looking at spin-wave modes, or delays in spin-echo arrival time.

4.4 Eigenmodes

The previous section dealt with basic, observable properties of the spin-transport equation including the demagnetising field. More physical information can be gained from the simulation by looking at the eigenmodes themselves: the damping, shift and spatial variations of the longest-lived solutions to the eigenvalue-equation.

Magnetostatic modes of a characteristic equation involving the demagnetising field were studied theoretically by Joseph and Schlömann[81][82] for a long cylinder. Their work does not include spin-transport and the model of this thesis (based on magnetodynamic modes) requires finite spin-transport for computational reasons, so a direct comparison of results is not possible.

4.4.1 Damping and Shifts

The cross-over from demagnetising-field dominated to gradient dominated is most apparent when looking at the properties of the least-damped eigenmode (with the smallest, negative, real part of the eigenvalue). Fig. 4.11 shows the variation in both damping (width of peak) and shift (relative to the central Larmor frequency) with changing gradient.

When the gradient is small, the damping is very small, of the same order as the real part of the diffusion timescale, implying that the mode is spread throughout the cell, with no sharp features (which would promote diffusion and loss). When ω_{G_1} increases beyond ω_M , a large increase in damping occurs over a small range of ω_{G_1} , to a regime where the damping depends on the gradient. Such behaviour is indicative of Leggett-Rice type modes.

The shift is a significant fraction of the demagnetising field for small gradient. For gradient-dominated behaviour, the least-damped eigenmode is localised at the end of the cell, hence it has a frequency shift almost equal to ω_{G_1} (there is also a contribution from the static term of the demagnetising field).

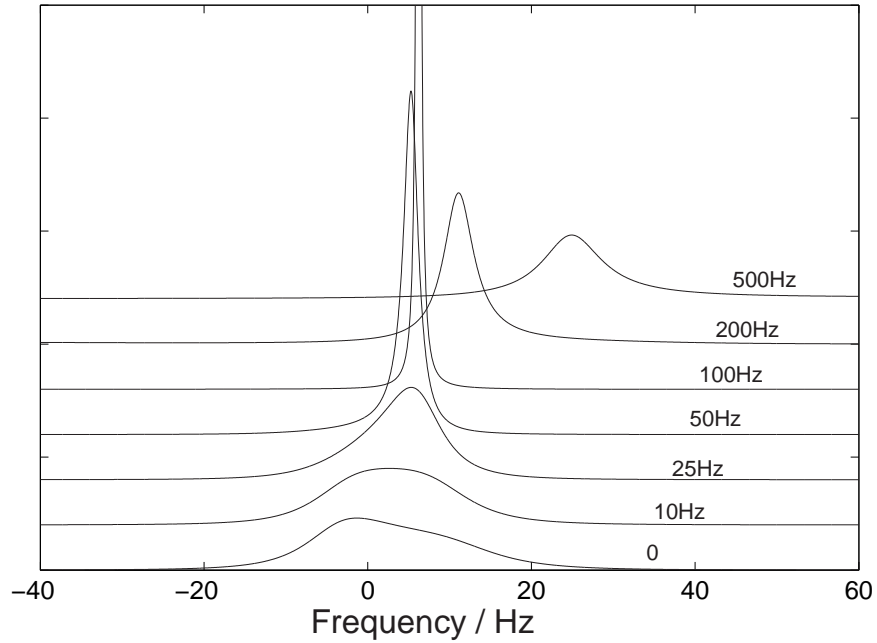


Figure 4.10: Demagnetising Field versus Second Order Gradient: the demagnetising field and the second-order field variation can almost cancel. Parameters to the model: $G_1 = 0$; $D_{\perp} = 10^{-5} \text{m}^2/\text{s}$; $\mu M_0 = 0$; $G_2 = -0.8 \text{T}/\text{m}^2$. Demagnetising frequency f_M shown next to each curve. For reference, $f_{G_2} = -34.3 \text{Hz}$

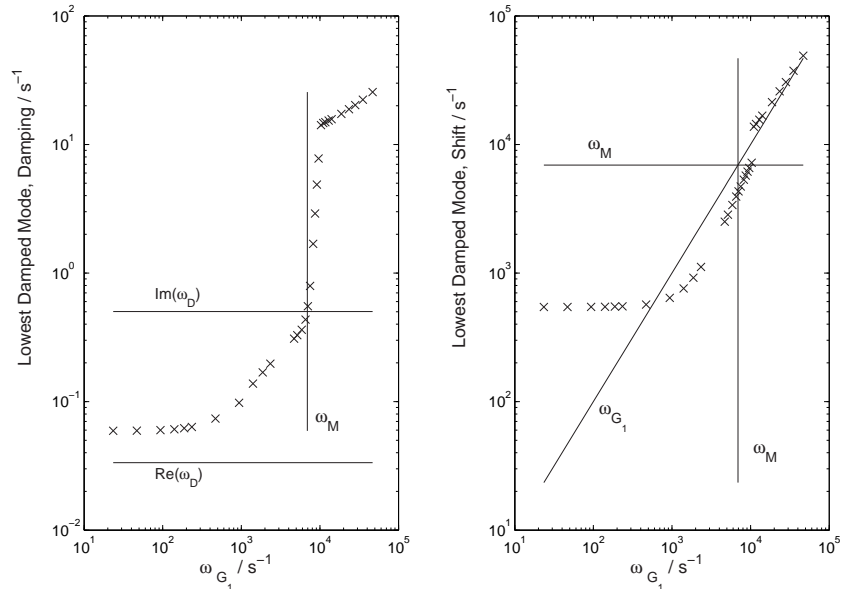


Figure 4.11: Damping and Shift of Least Damped Eigenmode: $L = 1.15 \text{mm}$; $D_{\perp} = 10^{-5} \text{m}^2/\text{s}$; $f_M = 2\pi \times 1100 \text{Hz}$; $\mu M_0 = 15$, calculated using m_{-} , there is no second order applied gradient.

4.4.2 Spatial Variations

The spectroscopic results allow some interpretation of the nature of the eigenmodes, but plotting the spatial variation of such modes is a more direct method of gaining physical insight. Since the eigenvalue equation is non-separable, the results are two-dimensional plots of magnetisation density as a function of axial and radial position. See Fig. 4.12 and Fig. 4.13, which can be thought of as being rotated around the axis of the cylinder, $r = 0$.

The most striking result of Fig. 4.12 is that the eigenmode is confined by the demagnetising field and not the walls, no matter what the sign of μM_0 . Such behaviour is in contrast to Leggett-Rice spin-wave modes in a gradient, which are confined by the gradient and one wall of the cell; the demagnetising field does not behave like a simple linear field variation. When spin-transport is purely diffusive, the structure of the mode is simple; the spin-rotation effect complicates the shape. When ω_M and μM_0 have the same sign (middle panel, Fig. 4.12), the mode is symmetric, and mostly confined in the centre of the cell, with ‘arms’ sticking out. The opposite sign of μM_0 (right-hand panel) makes the mode antisymmetric, with a node in the middle, and two lobes, although still confined mostly away from the wall; such an eigenmode would not be observed by an idealised (uniform response) FID/spectrum experiment.

Fig. 4.13 shows the effect of second-order applied gradient (when Leggett-Rice effect is present), with a characteristic scale $f_{G_2} = -34.3\text{Hz}$. The left-hand panel shows the result when there is no demagnetising field: the least-damped eigenmode is confined at the outer wall of the cell, half way along the axis. When the demagnetising effect is large (right-hand panel), the eigenmode is confined in the centre of the cell, away from the wall. There is a crossover (middle panel), where the mode is mostly at either end of the cell, near the axis; this results can be compared with Fig. 4.10

4.5 Spin-Echoes

The demagnetising field has a similar effect to a second order applied gradient, so it is interesting to see how the demagnetising field affects spin-echoes. Spin-echo calculation is an extension not easily amenable to the methods of Krotkov *et al*[79], but is simple using the matrix-representation method. The π -pulse has all the effects mentioned in section 2.4.1, Eqn. (2.47), but also the value of ω_M becomes the negative its original value ($\omega_M \propto$ longitudinal magnetisation). Therefore the

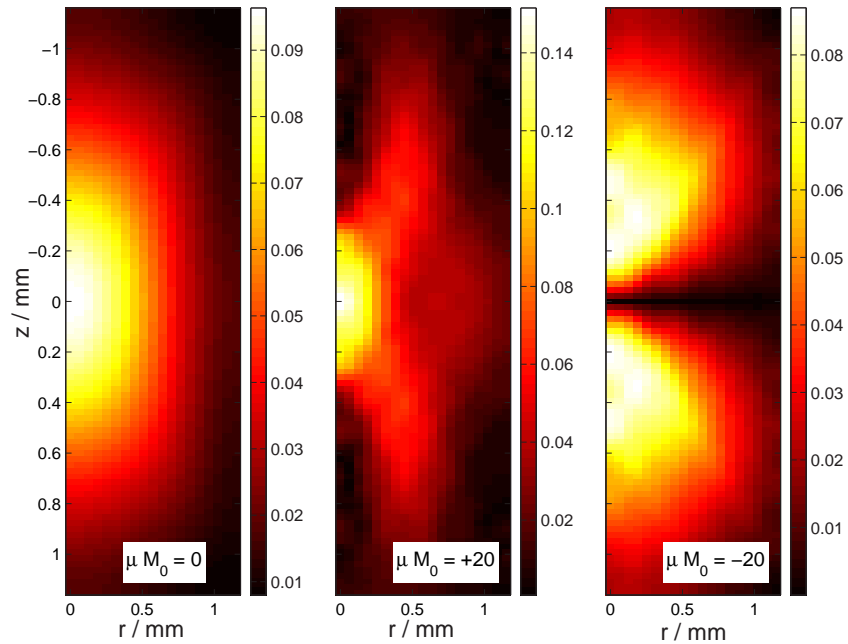


Figure 4.12: Spatial Variation of Least Damped Eigenmode, magnitude of magnetisation represented by colour: $L = 1.15\text{mm}$; $D_{\perp} = 3 \times 10^{-6}\text{m}^2/\text{s}$; $f_M = 200\text{Hz}$; calculated using m_{-} . There are no applied gradients. The modes are all confined away from the walls. The mode in right-hand panel is pure anti-symmetric.

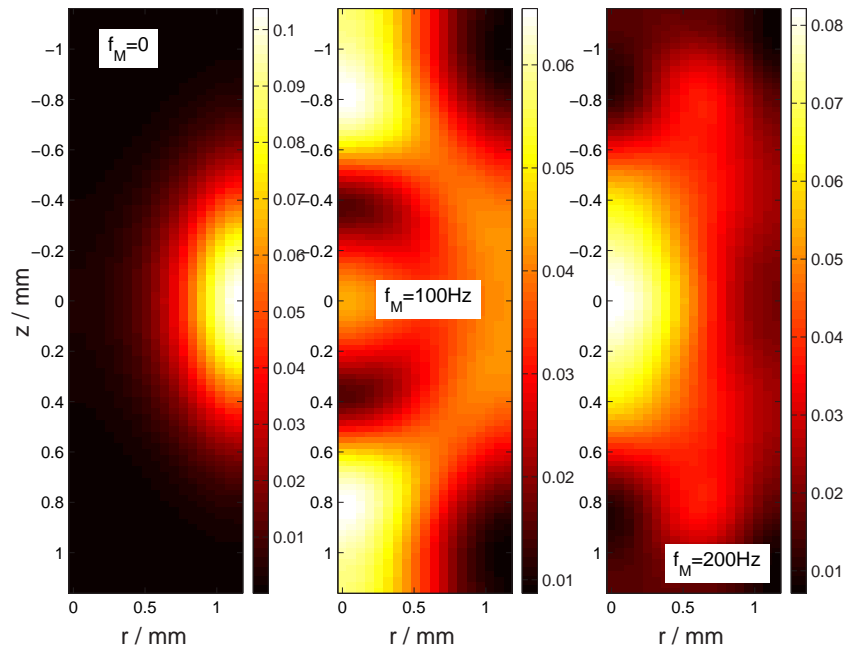


Figure 4.13: Spatial Variation of Least Damped Eigenmode, magnitude of magnetisation represented by colour: $L = 1.15\text{mm}$; $D_{\perp} = 10^{-5}\text{m}^2/\text{s}$; $\mu M_0 = 5$; $G_2 = -0.8\text{T}/\text{m}^2$ implying $f_{G_2} = -34.3\text{Hz}$; calculated using m_{-} . There is no first order applied gradient.

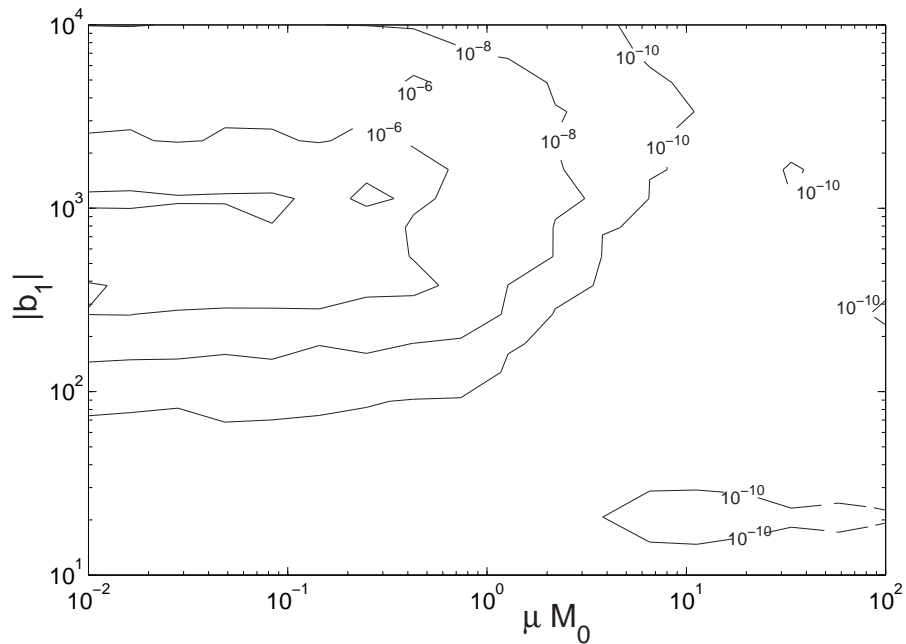


Figure 4.14: Orthogonality Violation, with Demagnetising Field. $\omega_M = 100\text{Hz}$; $\omega_{G_1} = 373\text{Hz}$. See also Fig. 2.16 ($\omega_M = 0$), see Eqn. (2.59a) for numerical definition of orthogonality violation.

demagnetising field is reversed by a π -pulse.

4.5.1 Violation of Orthogonality of Eigenfunctions

First, it is necessary to check that the eigenfunctions are orthogonal, if not then the operator method will be required. Fig. 2.16 shows how orthogonality is violated for pure linear gradient field; Fig. 4.14 presents the results of the same calculation when $f_M/f_{G_1} = 100\text{Hz}/373\text{Hz}$. The demagnetising field suppresses the non-orthogonality, so that in Fig. 4.14 the orthogonality violation is negligible. Further calculations with $G_2 \neq 0$ show that the second order gradient makes no significant difference to the orthogonality violation. The operator method is still needed when the demagnetising field is small.

4.5.2 Echo Signals

Fig. 4.4 shows the presence of both a short-lived component of the FID (inhomogeneous broadening) and a long-lived component (long-lived eigenmodes, spectral clusters). Spin-echo experiments are designed to return the short-lived components, allowing the irreversible decay to be measured. A complication is that, while the applied fields do not reverse at the π -pulse, the demagnetising field does reverse,

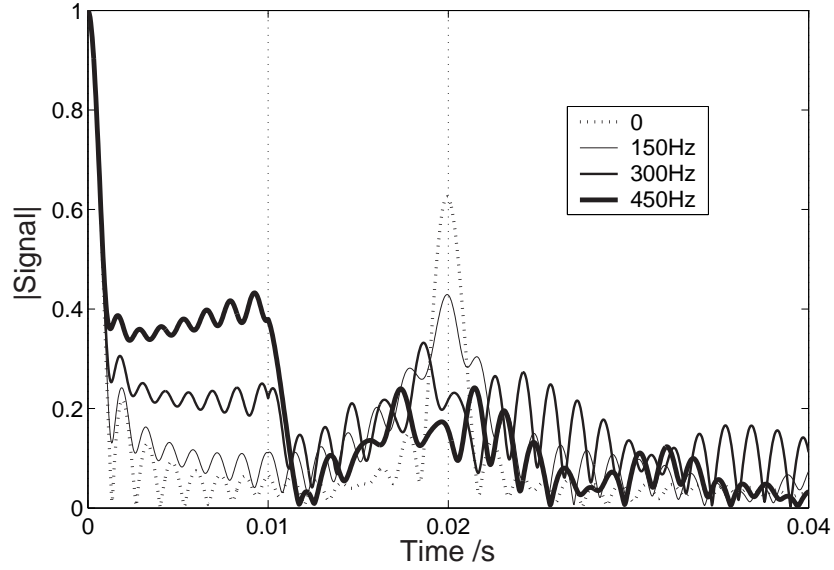


Figure 4.15: Spin Echoes with Demagnetising Field; the π -pulse is at time 0.01s. Parameters of the model are: $\mu M_0 = 10$, $D_{\perp} = 10^{-5} \text{m}^2/\text{s}$; $L = 1.15 \text{mm}$; $f_{G_1} = 373 \text{Hz}$; no second order gradient.

along with the magnetisation.

In Fig. 4.15 the simulation with the largest demagnetising field has a very reduced and distorted echo, because the long-lived components dominate before the π -pulse. After the π -pulse much of the long-lived components (the few least damped eigenmodes) are converted to a sum over more damped, shorter-lived eigenmodes. Therefore, much of the signal is lost to rapid decay, and does not re-phase in the same way as it de-phased before the π -pulse. There is a smooth transition to the demagnetising-dominated case from the no-demagnetising case.

Further simulations (not shown) show that when there is no applied field variation, the two-pulse experiment follows exactly the path of the single-pulse FID, except for the phase change at the π -pulse. Because the field (demagnetising field) reverses along with the phase, the de-phasing continues: for a classic spin-echo, the field does not reverse, so de-phasing is reversed. Therefore, when there is only a demagnetising field and spin-transport, no echo is seen.

Delays, and the lack thereof

Since the demagnetising field is similar to a second order gradient, it is surprising that the simulations in Fig. 4.15 show no delay. The delays caused by the presence of a G_2 term are related to the difference between maximum- and minimum-field seeking magnetisation. Take the case where the magnetisation is maximum-seeking

before the π -pulse: the eigenmodes are frequency-shifted away from each other more when G_2 is negative than when G_2 is positive; therefore the de-phasing will occur more slowly than re-phasing, so the echo will be advanced. See also section 2.4.2, Fig. 2.7 and Fig. 2.8

The same is not true for the demagnetising field, because the magnetic field variation reverses as the magnetisation changes from maximum-field seeking (pre- π -pulse) to minimum-field seeking (post- π -pulse). Thus, re-phasing and de-phasing occur at the same rate, and the echo is neither advanced nor delayed. Of course if $G_2 \neq 0$, then the result will still be an echo mis-timing.

4.5.3 Echo Analysis

If the inter-pulse waiting time is increased, then the short-lived component becomes less important, and the echo is suppressed: see Fig. 4.16. When the amplitude is less than about 15% of its initial value (log-amplitude is less than -1.9), the amplitude deviates from $e^{-t_w^3}$ behaviour, and the phase and timing change erratically, largely due to finite-size effects (note $|b_1| = 310$, so there are only about 13 significant eigenmodes). The echoes for short t_w are not significantly advanced; the small mis-timing is due to a decay envelope, and the effect of oscillations within the echo signal.

When there is no spin-rotation effect, there is residual phase-shift, dependent on the strength of the demagnetising field and the echo amplitude (Fig. 4.16, middle panel). Such a phase shift could easily be confused for $\mu M_0 \neq 0$, and may be responsible for the unexpected, apparent, high-temperature behaviour of the spin-rotation parameter, as shown in Fig. 3.12 (implicitly affecting and Fig. 3.11 and Fig. 3.13).

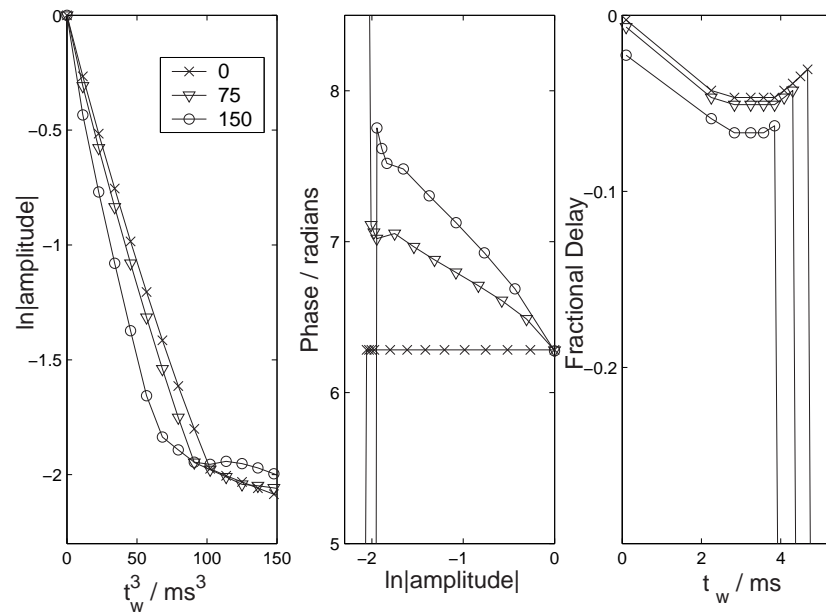


Figure 4.16: Spin Echoes with Demagnetising Field. Parameters of the model are: $\mu M_0 = 0$, $D_{\perp} = 10^{-5} \text{m}^2/\text{s}$; $f_{G_1} = 373 \text{Hz}$, $|f_D| = 1.2 \text{Hz}$; f_M is in the legend, in Hz. There is no second order gradient, and $|b_1| = 310$, so finite-size effects are important.

CHAPTER 5

ANALYSIS OF PURE ^3He DATA, INCLUDING DEMAGNETISING FIELD

5.1 Introduction

This chapter begins with a description of some NMR experiments of spin-transport in pure ^3He in Nottingham 1999: FIDs, spectra, spin-echoes and multiple spin-echoes were performed. Long-lived, linear, magneto-dynamic modes are observed as sharp peaks in the NMR spectra. The frequencies of such peaks are studied with respect to tipping angle, magnetisation, temperature and applied field gradient. The spectra are compared with the linear model of spin-dynamics in a Fermi-liquid with demagnetising field, as developed in chapter 4; the data cannot be understood without the including the demagnetising field in the model.

In contrast to the analysis of the data from experiments in 6.2% ^3He - ^4He mixture, the study concentrates on spectra and inversion-recovery experiments rather than spin-echoes (the match between model and experiment was not good enough for spin-echo comparisons). It should be noted that the demagnetising field has very little effect in 6.2% mixture, but is much larger in pure ^3He . Estimated values used as inputs to the model are obtained from Candela *et al*[39] (Fig.1), the original, approximate analysis of the same data. All simulations of this chapter are in m_+ representation. All spectra presented are absolute values $|\tilde{S}(\omega)|$ not absorption spectra (real parts).

5.1.1 Experimental Details

The experiments studied in this chapter were performed in Autumn 1999 in Nottingham. The same apparatus was also used to study ^3He - ^4He mixtures, as described in chapter 3. As such, the details were almost identical with respect to cooling, magnetic fields, thermometry and NMR apparatus; there were differences in the details of NMR experiments performed.

In 6.2% ^3He - ^4He mixture, the tipping angle in an FID experiment was usually 7° ; in pure ^3He , 8.6° . The π -pulse durations were usually $26\mu\text{s}$ and $21\mu\text{s}$ respectively (although in some pure ^3He experiments a π -pulse lasted $44\mu\text{s}$).

The magnetic field was shimmed using first- and second-order gradients, to minimise the width of the spectrum. As seen in section 4.3.4, shimming can leave a non-uniform static field when the demagnetising field is strong. Typically the NMR line-width after shimming was 600Hz; the demagnetising field frequency scale is 178Hz for pure ^3He in an 11.3 tesla field (for 6.2% ^3He - ^4He mixture, the demagnetising field corresponds to about 19Hz)[†]. Shimming was not performed for each applied linear gradient, only for zero gradient.

More care has been taken in post-processing the spectroscopic data in this chapter than for any other data from the Nottingham 1999 experiments. The signals were subject to both mains noise and broad-spectrum noise; see Appendix B for details. In particular, some of the spectra are *broadened* by up to 5s^{-1} , to remove broad-spectrum noise. The correct phases of the spectra are difficult to determine, so only absolute values are presented, not absorption spectra.

5.1.2 Large-Angle Data

Many single-pulse, FID experiments were performed. Of these, many had signals which lasted for almost a second, corresponding to peaks in the spectrum of widths a few hertz. The phenomenon has been shown to be present only for small tipping angles (Owers-Bradley *et al*[40]). Linear behaviour should occur when the initial tipping angle is small: $\sin \theta \sim \theta$, $\cos \theta \sim 1$, i.e. a few degrees. A figure is presented (Fig. 5.1) showing that non-linear effects occur even at quite small angles. The spectra have been artificially shifted both vertically and horizontally, the clearest way of viewing all the spectra at once. The spectra have been normalised so that the integral of the spectrum over frequency is a constant.

The spectrum for the smallest tipping angle, 4.1° , has many sharp features,

[†]Making use of Krotkov *et al*[79], Table I: numbers relating to experiments at saturated vapour pressure can be scaled, linearly with applied magnetic field.

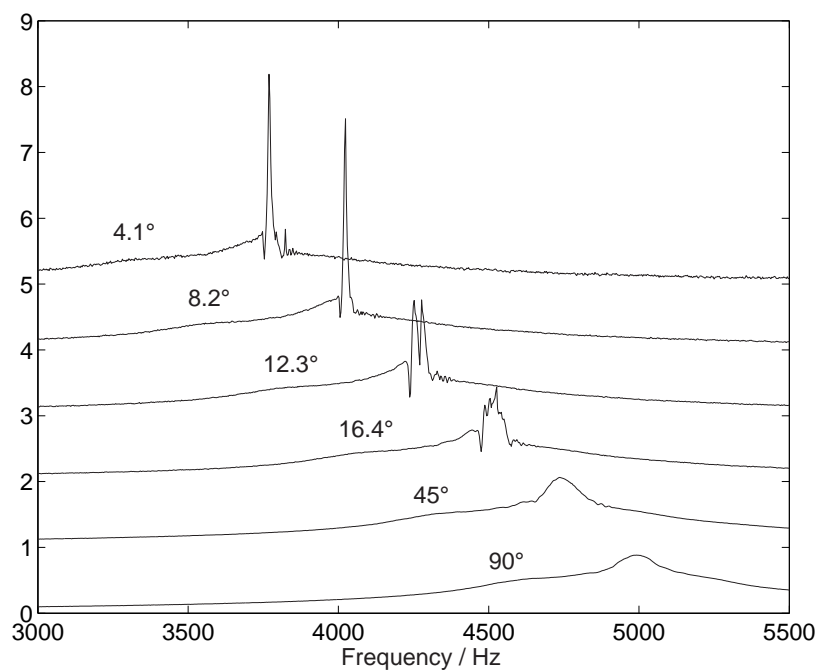


Figure 5.1: NMR spectra: Fourier transforms of FID experiments with various tipping angles. Spectra have been offset both vertically and horizontally for clarity; filtered to remove mains noise; and broadened by 5s^{-1} to reduce broad-band noise. Magnetic field has been shimmed (minimum width of spectrum). Spectra are labelled with tipping angles. The temperature is $13 \pm 2\text{mK}$.

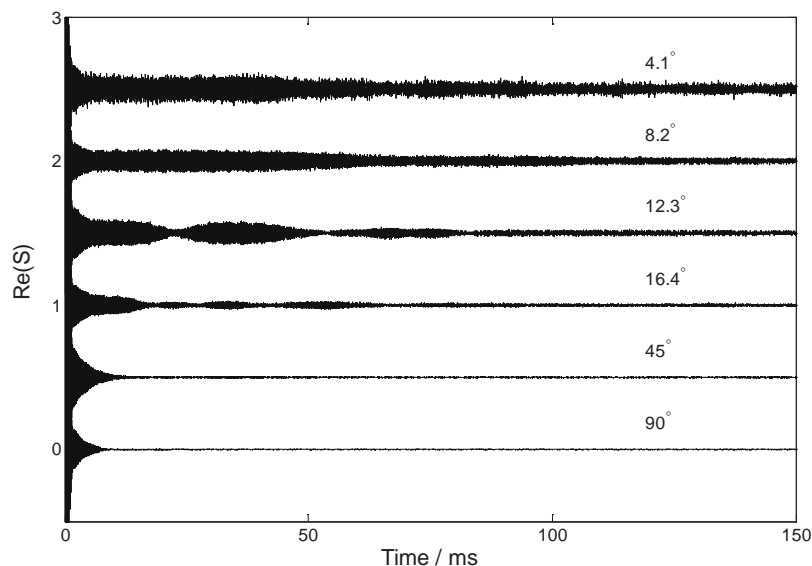


Figure 5.2: FIDs: These signals are inverse Fourier transforms of the filtered spectra shown in Fig. 5.1 without broadening or frequency shifts. Signals offset vertically for clarity (smallest tipping angle at the top). Signals are normalised such that the initial signal is unity. There are beats in the 12.3° and 16.4° experiments.

with one dominant peak, corresponding to a long lived FID signal: indicative of a *magneto-dynamic mode*. The 8.2° experiment is substantially similar; a few features are lost but non-linearities seem to be perturbative. The experiment at 16.4° shows two peaks where smaller angles produce only one peak. The two long-lived magnetisation-modes show up in the FID, Fig. 5.2: beats can clearly be seen. Long-lived signals are present for small tipping angles (linear behaviour), and not for large angles; the spectra for 90° and 45° tipping pulse are smooth.

5.1.3 Small-Angle Data

Long-lived signals are only present in linear or nearly-linear experiments; from now on, only experiments performed with a tipping pulse 8.6° are presented, so non-linear effects are deemed to cause only small changes to the spectrum: broadening and shift of peaks, reduction of number of peaks. Recovery experiments allow us to understand how the long-lived phenomenon depends upon the magnetisation; varying the temperature and applied field gradient clarify the role of the Leggett-Rice effect. In the light of chapter 4, I will argue that the data cannot be explained without reference to both the demagnetising field and spin transport.

5.1.4 Comparison with the Linear Model

We can compare the small-angle experimental data with the results of the model of the linear spin-dynamics of a Fermi-liquid in the presence of the demagnetising field, the model developed in chapter 4. A complication is that the computational load to simulate a real experiment is too high (tabulation of matrix elements takes too long, see section 4.1.5, page 94), so parameters must be adjusted accordingly, and conclusions inferred. Least-squares fitting is unfeasible.

For example, a single, optimised, example spectrum is shown in Fig. 5.3. The data was taken at 20mK, implying $\mu M_0 \sim 5$, and a $D_\perp \sim 2 \times 10^{-6} \text{ m}^2 \text{ s}^{-1}$. The inputs to the model are the demagnetising frequency, first and second order gradients and the spin-transport parameters. The diffusion coefficient is taken from Candela *et al*[39]; the spin-rotation parameter is slightly reduced, making the peaks in the model-spectrum about the right amplitudes for comparison with experiment-spectrum, although with greater peak widths from the model. We have considerable success re-creating both the overall line-shape of the spectrum, and the fine-structure. The positions of the sharpest peaks are matched to about 20Hz, out of a total inhomogeneous broadening of about 2000Hz; relative peak amplitudes are also simulated quite well.

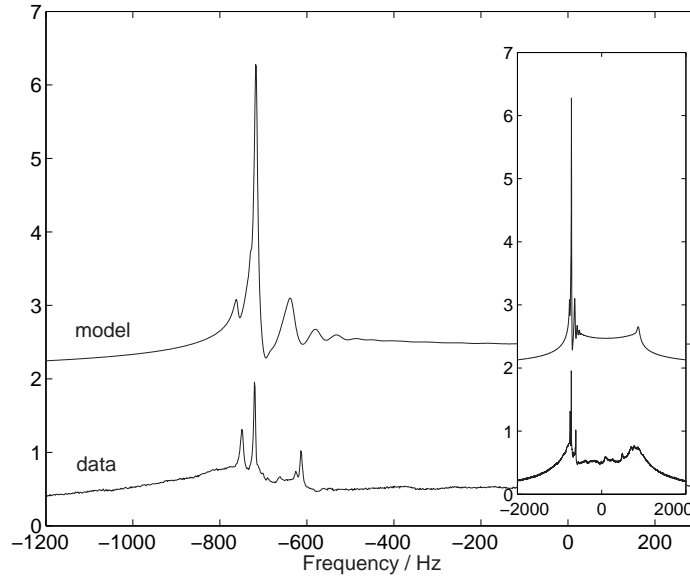


Figure 5.3: Direct comparison between the data and the model. The model has as inputs $\mu M_0 = +3$; $D_{\perp} = 2 \times 10^{-6} \text{ m}^2/\text{s}$; $G_1 = 22 \text{ mT/m}$; $G_2 = +0.5 \text{ T/m}^2$; $f_M = -178 \text{ Hz}$. Data is with $\sim 25 \text{ mT/m}$ applied gradient, at 20 mK ; has been shifted to coincide with the model; and is not broadened.

The limited basis set implies that a full experiment cannot be modelled accurately: in Ref. [59] it was shown that the number of axial basis functions required depends in the gradient and the spin-transport parameters, and is approximately $N \geq 6|\omega_G/\omega_D|^{1/3}$. Using the values from Candela *et al*[39], we see that spectra can be simulated accurately only if the inhomogeneous broadening is less than 65 Hz at 100 mK , or 37 Hz at 3 mK , since we are using a basis set with 50 (axial) by 9 (radial) functions. Failure to meet the condition leads to under-sampling and unphysical peaks appear in the simulated spectrum, although in practice the condition can be relaxed by a factor of about three. The criterion for accurate calculation does not take account of radial inhomogeneity, due to either G_2 or the demagnetising field.

Therefore, the model is far from an accurate calculation of real spectra with applied gradients. The solution is to enhance spin-diffusion in the model; to increase D_{\perp} and to choose μM_0 to broaden or narrow peaks as required. The result is that temperature-dependent effects are difficult to predict using the model. Also, there is no chance of least-squares fitting the data (as in Buu *et al*[53]) until much more computational power is available, but the model can be compared qualitatively with the experimental data. Fine structure in the spectrum or the overall line-shape can be simulated well, but not both.

5.2 Non-equilibrium Spectra

If the magneto-dynamic modes depend on the demagnetising field, then it will be instructive to look at spectra where the magnetisation is less than its equilibrium value. In such experiments, the spin-rotation parameter will be reduced along with the demagnetising field strength.

5.2.1 Recovery Experiments

A *recovery experiment* (or inversion-recovery experiment, see section 1.2.5) involves first tipping the magnetisation of the sample away from equilibrium, usually by 90° or 180° . The sample is then allowed to relax for a time similar to the longitudinal relaxation time T_1 , with the longitudinal magnetisation M following an exponential decay towards its equilibrium value, M_0 :

$$\frac{dM_z}{dt} = \frac{M_0 - M_z}{T_1} \quad (5.1)$$

At suitable intervals, a series of small tipping-angle FID experiments are carried out. The resulting non-equilibrium spectra allow us to understand how the longitudinal magnetisation influences the spin-dynamics.

The integral of the NMR spectrum signal over frequency should be proportional to the magnetisation, so the ratio of magnetisation to its equilibrium value can be calculated from a properly post-processed signal. Analysis of the magnetisation as a function of time yields T_1 (see Fig. 5.4). Typically T_1 is of order 200 seconds: longitudinal spin-diffusion of magnetisation generated from wall relaxation is probably the dominant process[39][69]. The timescale for diffusion of magnetisation across the cell is no greater than a few milliseconds, and the FID measurements are separated by at least 15 seconds, so one can be sure the magnetisation is always uniform before each FID experiment is performed. Measurements of the absolute values of M_z/M_0 are subject to uncertainty of about ± 0.05 .

Fig. 5.5 shows the results of a recovery experiment, where the magnetic field has been shimmed to give a minimal NMR line-width. The residual line-width is approximately 600Hz. The spectrum is shifted about 1100Hz from the resonant frequency, so the signal is away from the mains noise. As the magnetisation grows from zero to equilibrium, peaks appear in addition to the inhomogeneous broadening. These peaks represent magneto-dynamic modes, and have lifetimes up to 0.1s (with lifetimes roughly independent of temperature[39]).

When a gradient is applied, an increase in inhomogeneous broadening occurs but sharp peaks remain: see Fig. 5.6. The peaks form a smaller proportion of the

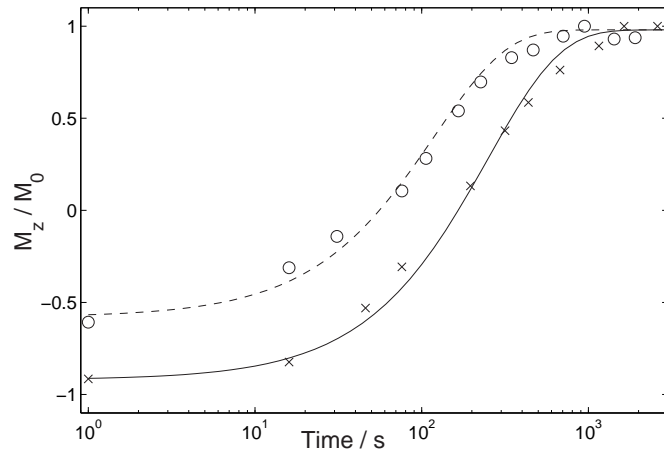


Figure 5.4: Recovery Experiment: Longitudinal Magnetisation as a function of time. Lines are fits-by-eye to $M_z(t) = M_z(\infty) - [M_z(\infty) - M_z(0)] e^{-t/T_1}$. The points are experimental: \circ with minimum field inhomogeneity, at $2.8 \pm 0.2\text{mK}$; dashed line $T_1 = 120\text{s}$. \times with $\sim 30\text{mT/m}$ applied field gradient, at $18 \pm 1\text{mK}$; solid line $T_1 = 250\text{s}$.

spectrum, and their structure is changed. When the magnetisation is reversed such peaks are not seen, only broad features. The spectrum is affected by the presence of the filling channel[54](see also section 3.3.3).

5.2.2 Low Magnetisation Spectra

Where the magnetisation is small ($M_z \ll M_0$), one can be sure both the Leggett-Rice and demagnetising-field effects will be small. As a consequence, the spectrum should be an image of the cell in frequency space, with some end effects due to spin-diffusion[60]. For a pure linear gradient, the spectrum should be zero for Larmor frequencies corresponding to outside the experimental cell, and constant for frequencies within. The line-shape at low magnetisation (Fig. 5.6 , inset, $M = 0.13 \times M_0$) does not fit the picture of a purely linear field inhomogeneity: the spectrum is asymmetric, with a broad peak at one end, and broad edges.

We have attempted to fit the shape of the line when the magnetisation is much less than the equilibrium magnetisation, using an analytical frequency-space distribution of linear and quadratic field variations, ignoring spin-transport and the demagnetising field, almost the same method as Ref. [53]. However, we have not succeeded in producing an automated least-squares fit: the method gives very bad results, because of the broad edges of the spectrum. Instead, fitting has been done by eye, so at least the approximate value of the linear (G_1) and quadratic (G_2) gradients are known; then estimates can be improved using the full model based on

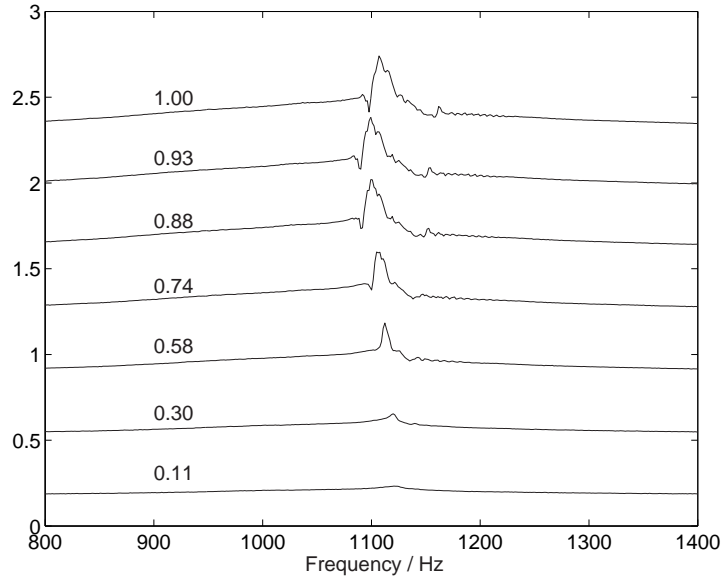


Figure 5.5: Recovery Experiment: field is shimmed (no applied gradient), temperature is $2.8 \pm 0.2\text{mK}$. Magnetisation for each spectrum is given in units of the equilibrium magnetisation, M_0 . Spectra are vertically offset for clarity. Peaks appear as the magnetisation increases.

Eqn. (4.20). It was impractical to shim for each applied field gradient; the estimated G_2 varies with applied linear gradient. Also, there is little data with $M < 0.2M_0$ or $G_1 > 60\text{mT/m}$, making the results inconclusive. The field variation is not known with any great precision: the errors on G_1 and G_2 are $\pm 10\text{mT/m}$ and $\pm 2\text{T/m}^2$ respectively.

5.2.3 Recovery Experiments: Simulation

The magnetisation, in units of the equilibrium magnetisation, is an input to the model. Also supplied are the diffusion coefficient, D_\perp , equilibrium spin-rotation parameter, μM_0 , the equilibrium demagnetising field, ω_{M_0} and the gradients, G_1 and G_2 . The non-equilibrium spin-rotation parameter, μM , and demagnetising field, ω_M are proportional to the magnetisation: $\mu M = \mu M_0(M/M_0)$, and $\omega_M = \omega_{M_0}(M/M_0)$. Spectra are calculated for several values of M/M_0 , thus simulating a recovery experiment.

Fig. 5.7 shows a re-creation of Fig. 5.6, where there is an applied field gradient of 30mT/m . Spin-transport coefficients are almost those from Candela *et al*[39], although μM_0 is a little low, reducing the number of peaks and their heights. A good overall line-shape for the spectra is produced; simulated peaks are similar to

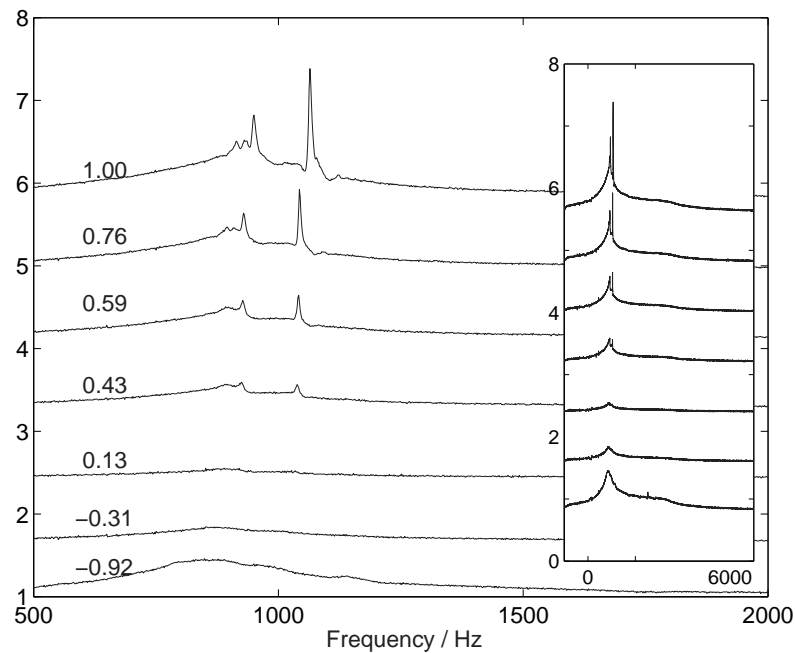


Figure 5.6: Recovery Experiment: applied field gradient is about 30mT/m, temperature is 18 ± 1 mK. Magnetisation M_z for each spectrum is given in units of the equilibrium magnetisation, M_0 . Spectra are vertically offset for clarity.

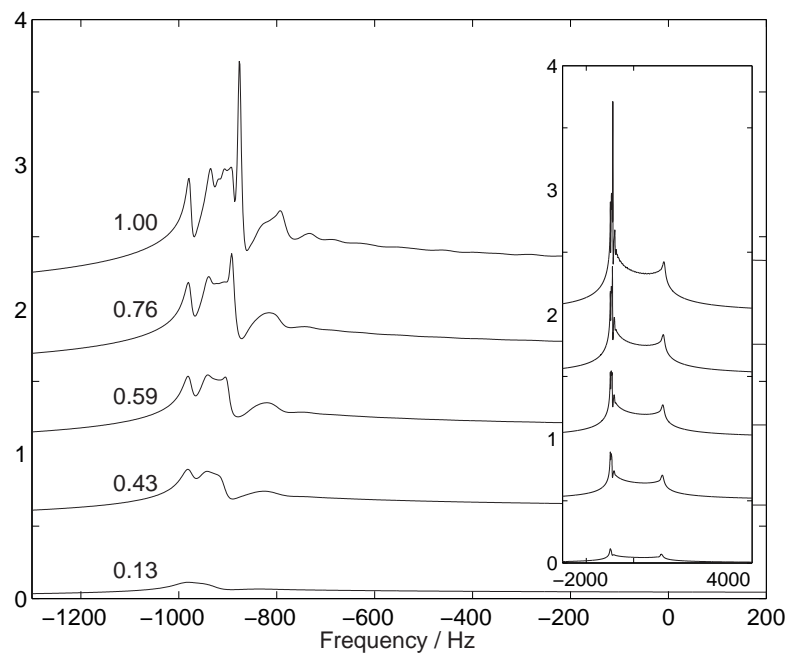


Figure 5.7: Simulated Spectra: re-creation of Fig. 5.6. Inputs to the model are: $\mu M_0 = +3$; $D_{\perp} = 2 \times 10^{-6} \text{m}^2 \text{s}^{-1}$; $G_1 = 30 \text{mT/m}$; $G_2 = -3 \text{T m}^{-2}$; $\omega_{M_0} = -178 \text{Hz}$. The spectra are normalised such that the integral of the spectrum is proportional to M_z/M_0 (values shown next to each curve).

those in the data. Close to equilibrium, however, there seem to be too many peaks in the simulation, and the peaks are too sharp.

We have much less success when there is no applied field gradient, i.e. inhomogeneous broadening is not much larger than the equilibrium demagnetising field. The primary reason is that of the uncertainty in the field variation is about the same magnitude as the field variation itself.

5.3 Equilibrium Spectra

When the magnetisation is at equilibrium, both spin-rotation and demagnetising-field effects are at their most prominent.

5.3.1 Varying the Temperature

Now let us consider the temperature dependence: see Fig. 5.8, with zero applied field variation. The spectra have been shifted so the sharpest peaks coincide at zero frequency. Oddly, the spectrum does not significantly change over more than two orders of magnitude of temperature: there are perhaps a few more peaks at the lowest temperatures. On closer inspection, one sees that the peaks are broadest (there is most damping) for the 28mK spectrum; damping can be characterised by the quantity $D_{\perp}/(1 + \mu M_0^2)$, which peaks at around 50mK, where $\mu M_0 = 1$ [39].

Applying a field gradient should expose standing-wave Leggett-Rice modes: see for example Candela *et al* 1986[37] of the rest of this thesis. A series of equally-spaced peaks is expected, becoming more prominent as the temperature decreases. Fig. 5.9 shows that the behaviour is not typical of the Leggett-Rice effect. The spectra have again been shifted to align the sharpest peaks.

The explanation offered is non-trivial. First define the frequency scales as in Eqn. (4.22), and the half-length of the cell is $L = 1.15$ mm. Note that when the Leggett-Rice effect dominates, there is a characteristic frequency shift between localised spin-wave modes, $\Delta\omega = \omega_G^{2/3}|\omega_D|^{1/3}$. There is also dimensionless ratio of frequencies[40]:

$$\beta = \frac{\omega_{M_0}}{\Delta\omega} = \frac{\gamma\mu_0 M_0}{(\gamma^2 G_1^2 D_{\perp}/|1 - i\mu M_0|)^{1/3}} \quad (5.2)$$

If β is much less than one, the peaks in the spectrum are determined by the Leggett-Rice effect, and perturbed by the demagnetising field[79]. Therefore one should see peaks becoming more obvious with decreasing temperature. If β is much greater than unity, then the demagnetising field dominates, and the peaks may be less

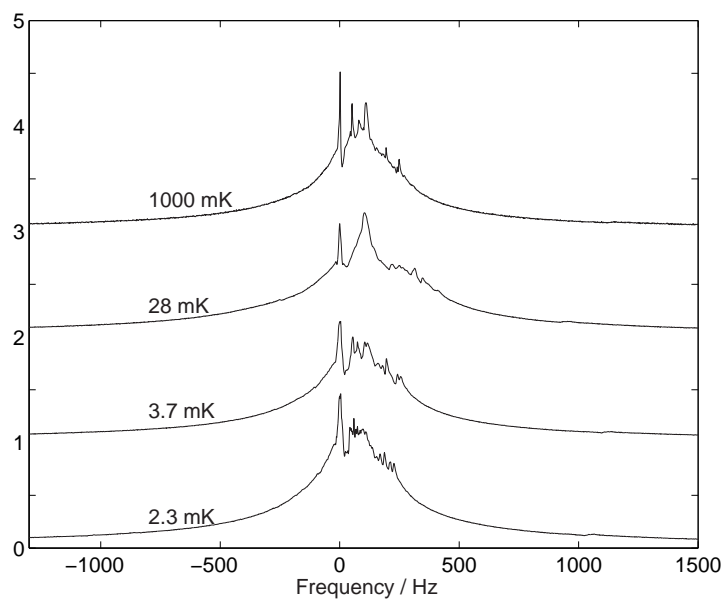


Figure 5.8: Equilibrium Spectra: Only residual field-inhomogeneity remains. The temperature is shown next to each spectrum. Spectra have been shifted vertically for clarity, and horizontally so the sharpest peaks coincide at 0Hz. Spectra have not been broadened. Whatever determines the peaks in the spectra, it seems to vary little over more than two orders of magnitude in temperature.

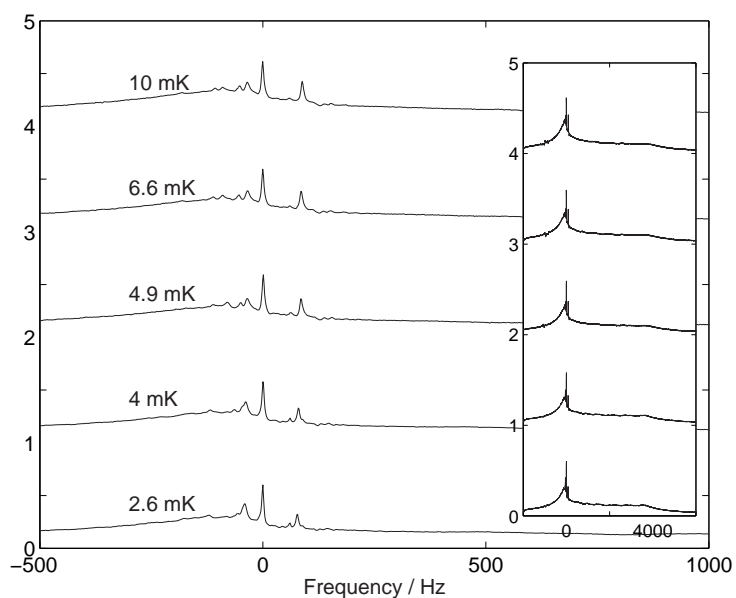


Figure 5.9: Equilibrium Spectra: A field gradient of $\sim 50\text{mT/m}$ is applied. The temperature is shown next to each spectrum. Spectra have been shifted vertically for clarity, and horizontally so the sharpest peaks coincide at 0Hz. Spectra have been broadened by 5s^{-1} . There is little temperature dependence.

temperature dependent. Estimates for the values of the spin-transport coefficients D_{\perp} and μM_0 are taken from Candela *et al*[39], which were determined using spin-echo data, extracted from the same cell at the same time as the data presented here. However, the data were analysed assuming an infinite cell, and no demagnetising field. Therefore the values used are only guidelines and do not represent accurate measurements.

The demagnetising frequency scale for ^3He in an 11.3T field is $\omega_{M_0} \sim 2\pi \times -178\text{Hz}$, and is largely independent of temperature below the Fermi temperature, which is about 1.7K for pure ^3He . The field-variation frequency-scale relevant to Fig. 5.9 is $\omega_G \sim 2\pi \times \frac{1}{2} \times 4000\text{Hz}$, from the width of the spectrum. At 100mK $\omega_D \sim 6.5 \times 10^{-3}\text{rad s}^{-1}$ ($D_{\perp} = 9.3 \times 10^{-9}\text{m}^2\text{s}^{-1}$ and $\mu M_0 \sim 0.4$); at 3mK $\omega_D \sim 0.017\text{rad s}^{-1}$ ($D_{\perp} = 3.4 \times 10^{-7}\text{m}^2\text{s}^{-1}$ and $\mu M_0 \sim 15$). Therefore, $\beta(100\text{mK}) = 1.76$ and $\beta(3\text{mK}) = 1.28$, so neither effect is really dominant. To really understand the spectrum, numerical calculations are required. However, because we have a limited basis set, we have enhanced the transverse spin-transport coefficients for the simulations, which means that we cannot give precise, numerical explanations.

5.3.2 Varying the Field Gradient

The parameter β can be adjusted more directly by changing the applied gradient at a fixed temperature, Fig. 5.10. The most obvious effect is simple inhomogeneous broadening. The peaks at the low-frequency end of the spectrum are more prominent for smaller gradients. The spectra in Fig. 5.10 are normalised such that the integrals over the spectra are equal, which means that the narrow spectra have greater vertical relief. Even accounting for the normalisation effect, the peaks seem most prominent where the applied gradient is least. The spectra have been shifted in accordance with the results of the line-shape field-gradient fitting, so the central Larmor frequencies are all set to zero, as well as possible.

Simulation

The data in Fig. 5.10 were taken at 20mK, implying $\mu M_0 \sim 5$, and a $D_{\perp} \sim 2 \times 10^{-6}\text{m}^2\text{s}^{-1}$. Fig. 5.11 shows the best effort at re-creating the data with the linear model. The gradients, G_1 and G_2 were found, in approximation, using analytic line-shape model, then improved using the full model. G_2 varies with G_1 , because of shimming problems. D_{\perp} has been enhanced by a factor of ~ 5 over the published value at 20mK[39]. Also, μM_0 has been reduced: the peaks are sharper than in the real spectrum, decreasing μM_0 broadens them, and reduces their heights.

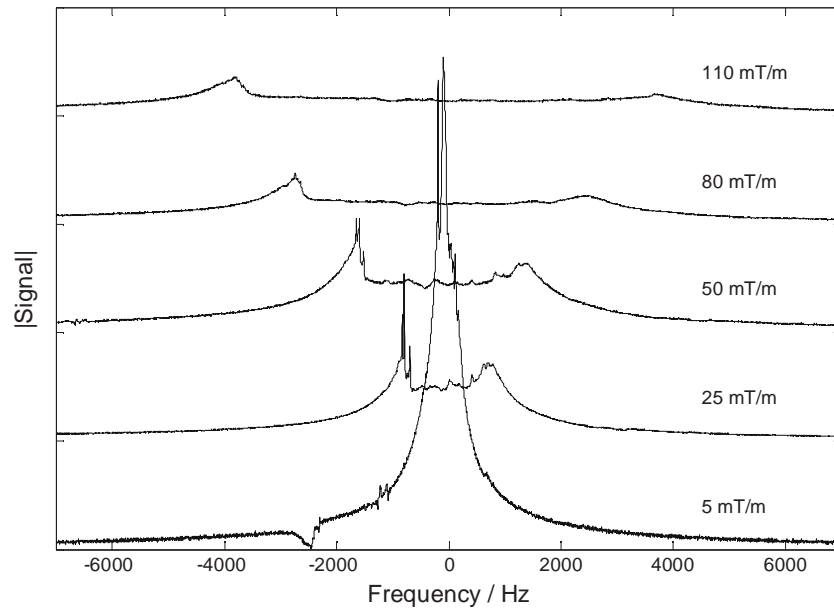


Figure 5.10: Equilibrium Spectra: the temperature is $T=(20\pm 1)$ mK. Applied field gradient varies from 0 to 110mT/m. Spectra have been shifted vertically for clarity, horizontally according to a line-shape fit so the central Larmor-frequencies are all zero, and broadened by 5s^{-1} . The peaks become less obvious as the inhomogeneous broadening increases.

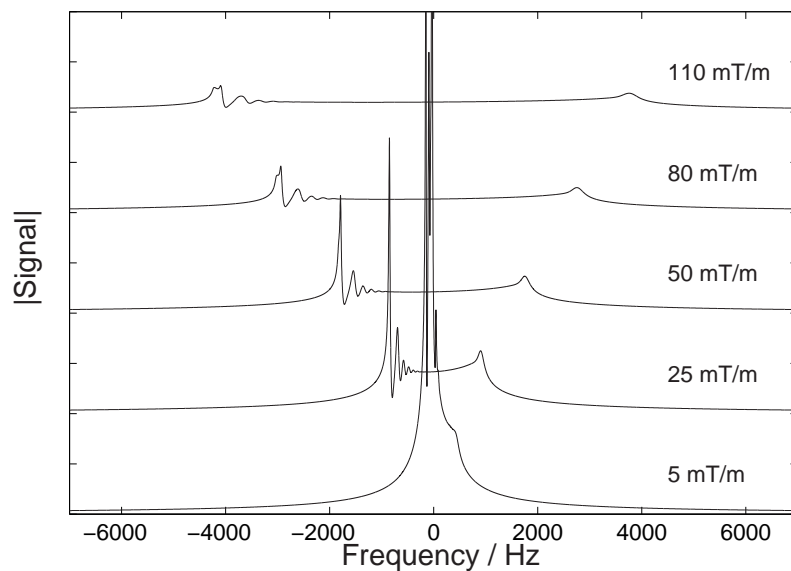


Figure 5.11: Simulated Spectra: a re-creation of Fig. 5.10. Inputs to the model are: $\mu M_0 = +3$; $D_{\perp} = 10^{-5}\text{m}^2\text{s}^{-1}$; $\omega_{M_0} = -178\text{Hz}$, G_1 as shown next to each curve. G_2 is chosen for each curve, in the range -5 to $+10\text{T/m}^2$. D_{\perp} has been enhanced by a factor of about ~ 5 over Fig. 5.7, for computational reasons.

We have succeeded in recreating the general shape of the spectrum when the gradients used as inputs to the model are carefully chosen, and there are peaks in about the right places. The peaks are more numerous, and spaced slightly further apart than the experimental spectra of Fig. 5.10.

5.4 Discussion

We have re-analysed data from NMR experiments performed in 1999, mostly looking at spectra, noting the presence of a long-lived magneto-dynamic modes for small tipping angles, revealing themselves as sharp peaks in the spectrum. Looking at inversion-recovery experiments we discover that the phenomenon depends on the magnetisation, and that the equilibrium spectrum does not show peaks growing with decreasing temperature, inferring that the Leggett-Rice effect is not directly responsible for the modes. The demagnetising field (dipolar field) is deduced to be responsible, because the peaks diminish when the field inhomogeneity is increased (as seen in the section 4.3.2, Fig. 4.7 and Fig. 4.8).

We compared our linearised model with the spectroscopic data. The match between model and experiment was not good enough to use least-squares fitting. The broad features of the spectra were reproduced: the overall line-shape both at equilibrium and reduced magnetisation; the approximate positions of the sharp peaks; the dependence of the spectra with varying magnetisation; the variation with field inhomogeneity.

No attempt has been made to fit simulation to spin-echo data, because the echoes are highly distorted, and there is insufficient computational power to model the effects of both boundaries with realistic spin-transport coefficients. Non-linear effects due to both the demagnetising field and spin-rotation are neglected by the model; for large-angle data (both FIDs and spin-echoes) the linear approximation is not valid.

The model does not match the data better because of the limited basis set, and the difficulty in accurately determining the magnetic-field variation. If more data were available, then perhaps better fits could be achieved. Non-linear effects are present (see Fig. 5.1) but are neglected in the analysis. It is possible, but difficult, to extend the model to account for weak, non-linear behaviour (finite-angle corrections).

CHAPTER 6

CONCLUDING REMARKS

A model of spin-dynamics of polarised Fermi-liquid helium-3 and its mixture with helium-4 is developed in chapter 2, with boundary condition suitable for a cylinder (axis parallel to the applied magnetic field). The effects of magnetic field gradients of first or second order can be simulated. The model converts the linearised equation of motion for transverse magnetisation to a matrix form. Numerical solution is either by decomposition into eigenmodes of the matrix, or by an operator-exponentiation technique. The solutions are turned into FIDs, NMR spectra and spin-echo simulations. Knowledge of the properties of the equation of motion, as in Appendix A, is found to be essential for studying spin-echoes. We find that the algebra used is analogous to the algebra used in quantum mechanics, but it is complex-symmetric not Hermitian. This difference can cause numerical problems relating to normalisation and orthogonality of eigenvectors.

The simulated amplitude and phase of spin-echoes are found to deviate significantly from the predictions of Leggett for conditions similar to those in the experiments of Nottingham (2000). The presence of the boundaries (cell walls) results in deviations from the exponential-time-cubed decay of the spin-echo amplitude. Also, the boundaries cause a saturation of the observed spin-rotation parameter, Fig. 2.13, akin to the effects of true saturation of transverse spin-transport. The same effect is likely to be present in several other published experiments: for example, Ager *et al*[28] and Akimoto *et al*[47]. The simulations also show that echoes arrive either in advance or delayed when a second-order field gradient is present. Therefore, to determine the true spin-transport coefficients from experiment, the data should be

compared with a detailed model.

In chapter 3, the linear model is compared directly to experiments in Nottingham: the assumptions of the model are tested. The assumptions made about mean free path effects, spin-lattice magnetic relaxation, suitability of the boundary condition, the demagnetising field, magnetic field gradients and thermal equilibrium are all found to be acceptable, such that the model can be compared to the experiments. The effects of the filling channel can be neglected for the experiments analysed, as can non-linear effects (as seen by comparison with the non-linear simulations of Dmitriev). The assumption that NMR pulses can be idealised (especially π -pulses in spin-echoes) is not valid: the model is appended to account for soft pulses.

The results of the simulation are then compared to experimental data acquired in the year 2000. Spectroscopic data permits determination of the magnetic field gradients, and estimates of the parameters which should be used as inputs to the model. Spin-echoes are then analysed using least-squares fitting by comparison with the simulations. The result is a value of both of the spin-transport coefficients D_{\perp} and μM_0 for each temperature for which a series of spin-echo experiments was performed: see Fig. 3.12 and Fig. 3.13. The uncertainties are based on the uncertainty in the magnetic-field gradients. The temperature variation of the spin-transport parameters has the expected $1/(T^2 + T_a^2)$ form with a characteristic temperature-scale $T_a = 6 \pm 1\text{mK}$.

The demagnetising field is not negligible for the pure ^3He experiments of 1999 (in Nottingham). The model is extended in chapter 4 to include the demagnetising field in a linear approximation. The equation of motion is again represented in matrix form, then solved; the resulting matrix is shown to be in agreement with the perturbative work of Krotkov *et al*[79].

The NMR-spectra from the simulation exhibit spectral clustering (a few, sharp peaks dominate the spectrum) when the demagnetising field is large, which is characteristic of demagnetising-field dominated spin-dynamics: see Fig. 4.5 and Fig. 4.6. When the field gradient is increased, the spectrum shows behaviour more typical of the Leggett-Rice effect. Non-perturbative effects are observed: peaks in the spectrum shift, split and appear when the relative strengths of the demagnetising field and the applied field inhomogeneity are varied. The demagnetising field is shown to almost mimic the appearance of a second-order field gradient, which would cause problems in NMR shimming. Also, spin-echoes experiments are strongly affected by the demagnetising field: strong demagnetising field reduces the echo-amplitude and distorts the echo, and causes echo-phase changes even when the spin-rotation effect is not present.

The final chapter, chapter 5, shows spectroscopic data from experiments in pure ^3He (Nottingham, 1999), where the demagnetising field is not negligible. Long-lived magneto-dynamic modes are observed as sharp peaks in the spectra. Recovery experiments show that the modes depend on the magnetisation, through both the demagnetising field and the Leggett-Rice spin-rotation effect. Little temperature variation is detected. The peaks decrease significantly when the applied magnetic field gradient is increased, which is characteristic of the demagnetising field rather than spin-rotation. The comparison of the extended model with experiments in pure ^3He is also shown: for example, see Fig. 5.3. For reasons of computational workload, least-squares fitting is not possible. Approximations are made in the simulation (enhancement of diffusion, suppression of spin-rotation) to allow comparison of model with data. The results show good qualitative agreement: numbers of peaks, relative positions and amplitudes, overall line-shape. However, quantitative agreement is poor due to the unrealistic spin-transport coefficients.

To sum up: we have developed a linear model of spin-dynamics in the presence of spin-diffusion, spin-rotation, the demagnetising field and finite boundaries; the model has been compared to experimental data and found to be accurate; transport parameters as functions of temperature have been derived for 6.2% ^3He - ^4He in 11.3T, wherein the anisotropy temperature is $6 \pm 1\text{mK}$.

Unanswered Questions and Future Work

The model could be extended to include non-linear effects, by allowing the amplitudes of eigenmodes to vary with time, and solving the resulting coupled differential equations. I expect that within five years, computers will be fast enough and cheap enough to allow direct comparison between the model (including demagnetising field) and the ^3He experiments, but until then the current model has been pushed to its limits. Changes to the boundary condition, suitable for a sphere or a cylinder perpendicular to the field, could be made, which would allow for comparison and fitting of other experiments.

Further experiments should be performed. Most notably, Ragan and Mullin[86] have suggested a two-pulse NMR experiment which could directly observe spin-transport anisotropy. The current understanding of spin-transport in ^3He in aerogel (a very open, fractal, glass structure which introduces disorder) has many gaps: see, for examples Refs. [87] and [35, 88, 89]. In particular, it is not known whether or not spin-waves exist in ^3He in aerogel.

The most interesting result of this thesis is the observation of saturation of spin-

transport parameters as temperature drops towards absolute zero, in 6.2% ^3He - ^4He mixture: a finite anisotropy temperature. However, the numerical result is not in agreement with other experiments, nor is it in full agreement with theory. There is no way of resolving the issue unless the same analysis (a model including boundaries) is applied to the other published experiments. Experiments at very low concentrations have low Fermi temperatures, so high-temperature effects are apparent; experiments with high concentrations have high Fermi temperatures, but low-concentration assumptions are invalid. The comparison of theory and experiments is unfeasible without significant extensions of the theories, to finite concentrations and temperatures which are a significant fraction of the Fermi temperature.

Publications

The following papers relating to this thesis have been published:

Ref. [59]:

O. Buu, R. Nyman, R.M. Bowley, and J.R. Owers-Bradley

Leggett-Rice effect in a finite geometry.

Phys. Rev. B, **65**, 134512, (2002).

Ref. [53]:

O. Buu, D. Clubb, R. Nyman, J.R. Owers-Bradley, and R. König

Transverse Spin Diffusion in ^3He - ^4He mixtures: Part I

J. Low. Temp. Phys., **128**, 123–142, (2002)

Ref. [54]

O. Buu, R. Nyman, D. Clubb, R.M. Bowley, J.R. Owers-Bradley, and G. Eska

Transverse Spin Diffusion in ^3He - ^4He mixtures: Part II

J. Low. Temp. Phys., **128**, 143–162, (2002).

Ref. [90]

R. Nyman, O. Buu, D. Clubb, J. Owers-Bradley, and R.M. Bowley

A Realistic Model of Spin-Transport indilute ^3He in ^4He in a Finite Geometry

Physica B, **329–333**, 183–184, (2003).

Two further papers are in preparation, relating to the linear model of demagnetising field (chapter 4), and the analysis of pure ^3He data using the model (chapter 5).

APPENDIX A

PROPERTIES OF THE LINEAR EQUATION OF MOTION

The similarity between Eqn. (2.8) and the Schrödinger equation was noted on page 29. This becomes especially clear if we define a *pseudo-hamiltonian* operator which is $-i\frac{\partial}{\partial t}$. The Schrödinger equation is Hermitian, which has important consequences. The definition of hermiticity is:

$$\int_V f \hat{H} g \, d^3\mathbf{r} = \int_V g \hat{H}^* f \, d^3\mathbf{r} \quad (\text{A.1})$$

where f and g are any two well-behaved functions in a volume V , which satisfy a sensible boundary condition at the closed surface S which bounds V .

The Hamiltonian for the Schrödinger equation is

$$\hat{H} = -\frac{\hbar^2}{2m}\nabla^2 + V(\mathbf{r}) \quad (\text{A.2})$$

It is trivial to show that the potential term is hermitian, but the kinetic term, containing second order partial derivatives, is less simple. We must apply Green's theorem, as follows:

$$\int_V f \nabla^2 g \, d^3\mathbf{r} = \int_S f \nabla g \cdot d\mathbf{S} - \int_V (\nabla f) \cdot (\nabla g) \, d^3\mathbf{r} \quad (\text{A.3})$$

We reverse the order of functions (g before f) and repeat; then if the boundary conditions mean that the surface integral is zero, then ∇^2 must be hermitian. For quantum mechanics in a infinite-depth potential well the functions f and g are

required to be zero at the surface; or in free-space the functions go to zero at infinity, which is a suitable bounding surface; so:

$$\begin{aligned} \int_V f \nabla^2 g \, d^3 \mathbf{r} &= - \int_V (\nabla f) \cdot (\nabla g) \, d^3 \mathbf{r} \\ &= \int_V g \nabla^2 f \, d^3 \mathbf{r} \end{aligned} \quad (\text{A.4})$$

Since ∇^2 is real (it is equal to its complex conjugate), it is also Hermitian. Since its pre-factor in the Schrödinger equation is real ($-\hbar^2/2m$), the kinetic term in the Hamiltonian is Hermitian.

Now, we define a pseudo-hamiltonian for the linearised Leggett-Rice equation, Eqn. (2.8) in the same way.

$$\hat{H} = -i \frac{\partial}{\partial t} = +\gamma G(\mathbf{r}) - \frac{iD_{\perp}}{1+i\mu M_0} \nabla^2 \quad (\text{A.5})$$

Clearly the $\gamma G(\mathbf{r})$ part, the potential, is Hermitian, but what about the kinetic term? We need to know the boundary condition, which is that the gradients of the functions must be zero at the bounding surface (or at infinity), meaning no spin-current into the walls of an experimental cell (see Eqn. (2.9)). Thus, the surface integral in Eqn. (A.3) is still zero. The pre-factor is not real, so

$$\int_V f \left(\frac{iD_{\perp}}{1+i\mu M_0} \nabla^2 \right) g \, d^3 \mathbf{r} = \left(\frac{iD_{\perp}}{1+i\mu M_0} \right) \int_V f \nabla^2 g \, d^3 \mathbf{r} \quad (\text{A.6a})$$

is not equal to

$$\int_V g \left(\frac{iD_{\perp}}{1+i\mu M_0} \nabla^2 \right)^* f \, d^3 \mathbf{r} = \left(\frac{iD_{\perp}}{1+i\mu M_0} \right)^* \int_V f \nabla^2 g \, d^3 \mathbf{r} \quad (\text{A.6b})$$

Therefore, the pseudo-hamiltonian is not Hermitian, except in the limit $\mu M_0 \gg 1$

Instead, we define another property, *complex symmetry*, which reverses the order of functions, as in Eqn. (A.1), but takes no complex conjugate. It is clear that our operator, Eqn. (A.5) will have this property: the pseudo-hamiltonian will be complex symmetric.

This property is called complex symmetry because, if a matrix representation is made of this operator, the elements must be symmetric (the matrix is equal to its own transpose); and in general the elements are complex because the effective spin-diffusion coefficient is complex. The proof is simple: define a matrix element H_{mn} , using a basis set f_m and f_n :

$$\int_V f_m \hat{H} f_n \, d^3 \mathbf{r} = \int_V f_n \hat{H} f_m \, d^3 \mathbf{r} \quad \therefore \quad H_{mn} = H_{nm} \quad (\text{A.7})$$

and it must be equal to H_{mn} , which is both the definition of the elements of a symmetric matrix, and of a symmetric operator.

With the Schrödinger equation, it is simple to show that the eigenvalues are real, and that non-degenerate eigenfunctions are orthogonal: write the eigenvalue equation $H\psi_m = E_m\psi_m$, pre-multiply by ψ_n^* and integrate, repeat the same with reversed indices and subtract one from the other. If we repeat this with our pseudo-hamiltonian, applying Eqn. (A.7) without the complex conjugate, we find:

$$\hat{H}\Psi_m = \omega_m\Psi_m \quad (\text{A.8})$$

$$\therefore (\omega_m - \omega_n) \int_V \Psi_m \Psi_n d^3\mathbf{r} = 0 \quad (\text{A.9})$$

which tells us that eigenfunctions of non-degenerate eigenvalues are orthogonal. The eigenvalues are in general complex.

It seems we should normalise our eigenfunctions by setting

$$\int_V \Psi_m \Psi_n d^3\mathbf{r} = 1 \quad (\text{A.10})$$

which is unlike quantum-mechanical stationary states, for which one includes a complex conjugate.

The eigenfunction method (section 2.2.3) requires that the eigenfunctions of the pseudo-hamiltonian operator form a complete, orthogonal set. We try to write an arbitrary function of space, $F(\zeta, \rho)$ as a sum over eigenfunctions

$$F(\zeta, \rho) = \sum_{\text{all } n,l} a_n \Psi_{nl}(\zeta, \rho) \quad (\text{A.11})$$

where the coefficients are given by

$$a_n = \iint \rho' d\rho' d\zeta' F(\zeta', \rho') \Psi_{nl}(\zeta', \rho') \quad (\text{A.12})$$

It becomes clear, if we write $\delta(\zeta - \zeta')\delta(\rho - \rho') = F$, that the eigenfunctions form a complete set:

$$\delta(\zeta - \zeta')\delta(\rho - \rho') = \sum_{\text{all } n,l} \Psi_{nl}(\zeta, \rho)\Psi_{nl}(\zeta', \rho') \quad (\text{A.13})$$

One can arbitrarily re-write the equation of motion multiplied by $\pm i$, without changing the properties, because all the analysis in this appendix involves linear algebra.

APPENDIX B

NMR SIGNAL ANALYSIS

We process the raw NMR signals to know which features are real, and which are experimental artifacts. The data comes as two channels, x and y , in phase and in quadrature with the reference oscillator. Both channels are treated as a single complex quantity $S_+ = S_x + iS_y$. Analysis of spin-echo experiments is in general simpler than analysis of FIDs and spectra.

In the experiments analysed in this thesis, the signal was preceded by a short background sample. The background signal is subtracted from both channels for the rest of the signal, and is mostly a function of the receiver-amplifier. It is common to consider the first few points of an NMR signal as *dead-time*, with the signal from the magnetisation hidden by the direct signal from the first pulse; although often no dead-time is taken, especially for spectroscopic data in chapter 5.

FIDs and Spectra

One sometimes wants phase and amplitude normalisation, which can be achieved one of two ways: dividing by the initial signal amplitude, or by the integral of the signal over frequency. Defining the beginning of the true signal is slightly arbitrary. The signal includes noise, which makes the integrals unreliable.

Unfiltered mains noise was a significant contribution to the signal. Our solution is to Fourier transform the signal, then multiply by a filter function: unity minus a sum over Lorentzians at 50Hz and harmonics (between -150 and +150 Hz), of widths 3 to 7Hz. We also reconstructed the data within the Lorentzians, using a cubic fit

to the data close by. Broad spectrum noise can be smoothed, by multiplying the real-time signal (after baseline subtraction, before filtering) by an exponential decay, which is equivalent to convolving the spectrum with a Lorentzian.

In this manner we have systematically removed most of the irrelevant features from the spectra, so it is easier to see what is really there. Also, signals can be integrated with much greater accuracy. Since the integral of the signal should be proportional to the magnetisation, more accurate measurements of the magnetisation can be made.

Conventionally, one shows the absorption spectrum (the real part of the spectrum, which should be positive only) or the dispersion spectrum (imaginary part, both positive and negative). However, we have problems separating the two, perhaps because of the mains noise, perhaps due the combination of to finite duration pulses and field inhomogeneities (see chapter 3 or Nyman *et al*[90]). As a consequence, even in filtered, reconstructed spectra of chapter 5 only the absolute values of the spectrum are shown. There is an exception for figure Fig. 3.8, showing the absorption spectrum.

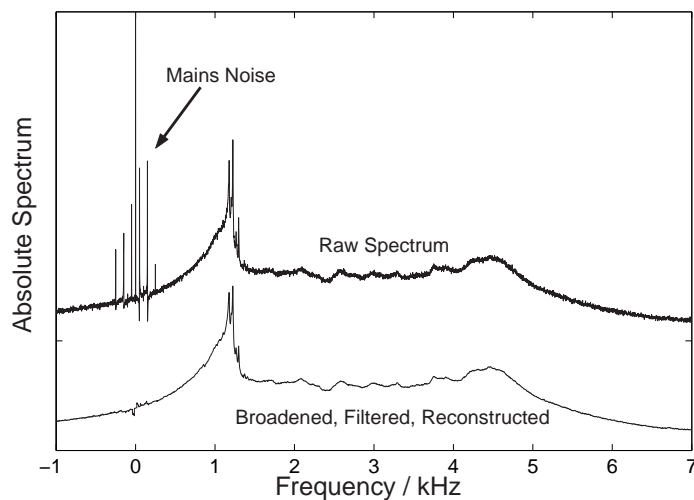


Figure B.1: Example of Data Filtering and Reconstruction: An NMR spectrum (Fourier transform of FID signal) of pure ^3He , before and after filtering and polynomial reconstruction; temperature about 5mK and applied gradient of roughly 50mT/m. Broadening by 15s^{-1} before filtering and polynomial reconstruction. The broadening removes broad-spectrum noise, and the filtering and reconstruction removes mains noise.

Spin-Echoes

Most of the analysis of spin-echoes in chapter 3 was performed by David Clubb and Olivier Buu. They used a short dead-time (about five data points), and normalised amplitude and phase by the initial FID signal after the dead-time. The π -pulse time and echo time, amplitude and phase were easily found after this. No filtering or other post-processing was required.

APPENDIX C

MATRIX REPRESENTATION OF DEMAGNETISING FIELD OPERATORS

In this appendix, a matrix form is derived for the terms in the linearised equation of motion which are proportional to the demagnetising field strength (proportional to ω_M), of chapter 4. The difficult terms are $\hat{n}_{zz}[1]$ and $\hat{n}_{zz}[m_-]$, and the expansion of the function $|\mathbf{r} - \mathbf{r}'|^{-1}$. The work herein should be attributed to Roger Bowley and Olivier Buu, not myself, and will be submitted as part of a longer article to the *Journal of Low Temperature Physics*.

Matrix Diagonalisation

To evaluate elements of the matrix we need to evaluate $n_{zz}[\Psi]$ which involves the function $|\mathbf{r} - \mathbf{r}'|^{-1}$. One representation of it in cylindrical coordinates is [91]

$$\begin{aligned} \frac{1}{|\mathbf{r} - \mathbf{r}'|} &= \sum_{\nu=-\infty}^{\infty} e^{i\nu(\phi-\phi')} \int_0^{\infty} e^{-k_1|z-z'|} J_{\nu}(k_1\rho) J_{\nu}(k_1\rho') dk_1 \\ &= \frac{1}{R} \sum_{\nu=-\infty}^{\infty} e^{i\nu(\phi-\phi')} \int_0^{\infty} e^{-\alpha k|\zeta-\zeta'|} J_{\nu}(k\rho) J_{\nu}(k\rho') dk.. \end{aligned} \quad (\text{C.1})$$

where we have converted to reduced variables, ζ and ρ .

Dynamic Term

The term $-\hat{n}_{zz}[m_+]$ is called the dynamic term. It is

$$\begin{aligned}\hat{n}_{zz}^{\text{dyn}} &= \hat{n}_{zz}[\Psi_{n,l}] = -\frac{1}{4\pi\alpha} \frac{\partial^2}{\partial\zeta^2} \int_0^{2\pi} d\phi' \int_0^1 \rho' d\rho' \int_{-1}^1 d\zeta' \Psi_{n,l}(\rho', \zeta') \\ &\times \sum_{\nu=-\infty}^{\infty} e^{i\nu(\phi-\phi')} \int_0^{\infty} e^{-\alpha k|\zeta-\zeta'|} J_{\nu}(k\rho) J_{\nu}(k\rho') dk.\end{aligned}$$

Since the basis function is taken to be independent of ϕ , integration over ϕ' gives just the $\nu = 0$ term.

$$\begin{aligned}\hat{n}_{zz}[\Psi_m] &= -\frac{1}{4\pi\alpha} \int_0^{2\pi} d\phi' \int_0^1 \rho' d\rho' \int_{-1}^1 d\zeta' \Psi_m(\rho', \zeta') \\ &\times \frac{\partial^2}{\partial\zeta^2} \int_0^{\infty} e^{-\alpha k|\zeta-\zeta'|} J_0(k\rho) J_0(k\rho') dk.\end{aligned}$$

Now

$$\frac{\partial^2(e^{-\alpha k|\zeta-\zeta'|})}{\partial\zeta^2} = -2\alpha k \delta(\zeta - \zeta') + \alpha^2 k^2 e^{-\alpha k|\zeta-\zeta'|}$$

so that

$$\hat{n}_{zz}[\Psi_m] = (\hat{n}_{zz}[\Psi_m])_1 + (\hat{n}_{zz}[\Psi_m])_2$$

where

$$\begin{aligned}(\hat{n}_{zz}[\Psi_m])_1 &= \frac{1}{2\alpha} \int_0^1 \rho' d\rho' \int_{-1}^1 d\zeta' \Psi_m(\rho', \zeta') \delta(\zeta - \zeta') \\ &\times \int_0^{\infty} 2\alpha k J_0(k\rho) J_0(k\rho') dk; \\ (\hat{n}_{zz}[\Psi_m])_2 &= -\frac{1}{2\alpha} \int_0^1 \rho' d\rho' \int_{-1}^1 d\zeta' \Psi_m(\rho', \zeta') \\ &\times \int_0^{\infty} \alpha^2 k^2 e^{-\alpha k|\zeta-\zeta'|} J_0(k\rho) J_0(k\rho') dk.\end{aligned}$$

The matrix element of $(\hat{n}_{zz}[\Psi_m])_1$ with Ψ'_m is

$$\begin{aligned}\int \Psi_{m'} (\hat{n}_{zz}[\Psi_m(\zeta, \rho)])_1 d^3r &= \Theta_{n'} \Theta_n \Xi_{l'} \Xi_l \int_0^1 J_0(\kappa_{l'} \rho) \rho d\rho \int_0^1 \rho' d\rho' J_0(\kappa_l \rho') \\ &\times \int_{-1}^1 d\zeta \cos(k_{n'}(\zeta + 1)) \cos(k_n(\zeta + 1)) \\ &\times \int_0^{\infty} k J_0(k\rho) J_0(k\rho') dk\end{aligned}$$

The integral

$$\int_{-1}^1 d\zeta \cos(k_{n'}(\zeta + 1)) \cos(k_n(\zeta + 1)) = 0$$

if $n \neq n'$ and is unity otherwise. Now $\int_0^\infty k J_n(k\rho) J_n(k\rho') = \frac{1}{\rho} \delta(\rho' - \rho)$ so that

$$\int \Psi_{m'} (\hat{n}_{zz} [\Psi_m(\zeta, \rho)])_1 d^3r = \Xi_{l'} \Xi_l \int_0^1 J_0(\kappa_{l'} \rho) J_0(\kappa_l \rho) \rho d\rho.$$

But[92]

$$\int_0^1 J_0(\kappa_{l'} \rho) J_0(\kappa_l \rho) \rho d\rho = 0$$

unless $\kappa_{l'} = \kappa_l$. It follows that

$$\int \Psi_{m'} (\hat{n}_{zz} [\Psi_m(\zeta, \rho)])_1 d^3\mathbf{r} = \delta_{n,n'} \delta_{l,l'}.$$

The matrix element of $(\hat{n}_{zz}[\Psi_m])_2$ with $\Psi_{m'}$ is

$$\begin{aligned} (n_{zz2}^{\text{dyn}})_{m'm} &= \int \Psi_{m'} (\hat{n}_{zz} [\Psi_m(\zeta, \rho)])_2 d^3\mathbf{r} \\ &= -\frac{\Theta_n \Xi_l \Theta_{n'} \Xi_{l'}}{2\alpha} \int_0^1 J_0(\kappa_{l'} \rho) \rho d\rho \int_0^1 J_0(\kappa_l \rho') \rho' d\rho' \\ &\quad \times \int_0^\infty \alpha^2 k^2 J_0(k\rho) J_0(k\rho') dk \int_{-1}^1 \cos(k_{n'}(\zeta + 1)) d\zeta \\ &\quad \times \int_{-1}^1 \cos(k_n(\zeta' + 1)) e^{-\alpha k |\zeta - \zeta'|} d\zeta'. \end{aligned}$$

To simplify the expression we use the following integral

$$e^{-\alpha k |\zeta - \zeta'|} = \frac{1}{\pi} \int_{-\infty}^\infty \frac{k}{k_z^2 + k^2} e^{i\alpha k_z (\zeta - \zeta')} dz \quad (\text{C.2})$$

and define

$$\begin{aligned} d_n(k_z) &= \int_{-1}^1 \cos(k_n(\zeta + 1)) e^{ik_z \zeta} d\zeta \\ &= e^{ik_n} \left[\frac{\sin(k_z + k_n)}{(k_z + k_n)} + e^{-2ik_n} \frac{\sin(k_z - k_n)}{(k_z - k_n)} \right]. \end{aligned}$$

(For later use we define $D_n = \Theta_n d_n$.) Then the integral

$$\begin{aligned} I &= \int_{-1}^1 \cos(k_{n'}(\zeta + 1)) d\zeta \int_{-1}^1 \cos(k_n(\zeta' + 1)) e^{-\alpha k |\zeta - \zeta'|} d\zeta' \\ &= \frac{1}{\pi} \int_{-\infty}^\infty \frac{k}{k_z^2 + k^2} d_{n'}(\alpha k_z) d_n^*(\alpha k_z) dk_z \end{aligned}$$

Note that

$$\begin{aligned} d_{n'}(\alpha k_z) d_n^*(\alpha k_z) &= i^{(n'-n)} \left[\frac{\sin(\alpha k_z + n'\pi/2)}{(\alpha k_z + n'\pi/2)} + (-)^n \frac{\sin(\alpha k_z - n'\pi/2)}{(\alpha k_z - n'\pi/2)} \right] \\ &\quad \times \left[\frac{\sin(\alpha k_z + n\pi/2)}{(\alpha k_z + n\pi/2)} + (-)^n \frac{\sin(\alpha k_z - n\pi/2)}{(\alpha k_z - n\pi/2)} \right] \end{aligned}$$

If both n and n' are even integers, $d_{n'}(\alpha k_z)$ is real and even in k_z so that $d_{n'}(\alpha k_z)d_n^*(\alpha k_z)$ is even in k_z . If both n and n' are odd integers, $d_{n'}(\alpha k_z)$ is odd in k_z but $d_{n'}(\alpha k_z)d_n^*(\alpha k_z)$ is even in k_z . In contrast, if n is even and n' is odd then $d_{n'}(\alpha k_z)d_n^*(\alpha k_z)$ is odd in k_z and the integral over k_z is identically zero.

Finally

$$\begin{aligned} (n_{zz2}^{\text{dyn}})_{m',m} &= (n_{zz2}^{\text{dyn}})_{n'l',nl} \\ &= -\frac{\Theta_n \Xi_l \Theta_{n'} \Xi_{l'}}{2\pi} \int_0^\infty \alpha k^2 dk \int_{-\infty}^\infty \frac{k}{k_z^2 + k^2} d_{n'}(\alpha k_z) d_n^*(\alpha k_z) dk_z \\ &\quad \times \int_0^1 J_0(\kappa_l \rho) J_0(k \rho) \rho d\rho \int_0^1 J_0(k \rho') J_0(\kappa_l \rho') \rho' d\rho'. \end{aligned}$$

Gradshteyn and Ryzhik[92] in their eqn 5.54.1 give

$$\int_0^1 J_0(\kappa_l \rho) J_0(k \rho) \rho d\rho = \frac{k J_0(\kappa_l) J_1(k) - \kappa_l J_0(k) J_1(\kappa_l)}{k^2 - \kappa_l^2} = C_l(k).$$

Using this formula we obtain

$$\begin{aligned} (n_{zz2}^{\text{dyn}})_{n'l',nl} &= -\frac{\alpha \Theta_n \Xi_l \Theta_{n'} \Xi_{l'}}{2\pi} \int_{-\infty}^\infty d_{n'}(\alpha z) d_n^*(\alpha z) dz \int_0^\infty \frac{k^3 C_l'(k) C_l(k)}{k_z^2 + k^2} dk \\ &= -\frac{\alpha \Xi_l \Xi_{l'}}{2\pi} \int_{-\infty}^\infty D_{n'}(\alpha k_z) D_n^*(\alpha k_z) dk_z \int_0^\infty \frac{k^3 C_l'(k) C_l(k)}{k_z^2 + k^2} dk. \end{aligned}$$

This is the general formula for this part of the dynamic term. Then

$$(n_{zz}^{\text{dyn}})_{n'l',nl} = \delta_{n,n'} \delta_{l,l'} + (n_{zz2}^{\text{dyn}})_{n'l',nl}.$$

Static Term

The term m_+ leads to a diagonal matrix with magnitude of unity. The important part of the static term is $-2\hat{n}_{zz}[1]m_+$. We write

$$\hat{n}_{zz}[1] = (\hat{n}_{zz}[1])_1 + (\hat{n}_{zz}[1])_2$$

with

$$(\hat{n}_{zz}[1])_1 = \frac{1}{2\alpha} \int_0^1 \rho' d\rho' \int_{-1}^1 d\zeta' \delta(\zeta - \zeta') \int_0^\infty 2\alpha k J_0(k\rho) J_0(k\rho') dk; \quad (\text{C.3})$$

$$(\hat{n}_{zz}[1])_2 = -\frac{1}{2\alpha} \int_0^1 \rho' d\rho' \int_{-1}^1 d\zeta' \int_0^\infty \alpha^2 k^2 e^{-\alpha k |\zeta - \zeta'|} J_0(k\rho) J_0(k\rho') dk. \quad (\text{C.4})$$

The matrix element of $(\hat{n}_{zz}[1])_1$ is

$$\begin{aligned} (n_{zz1}^{\text{stat}})_{m'm} &= \int \Psi_{M'}(\zeta, \rho) \Psi_M(\zeta, \rho) (\hat{n}_{zz}[1])_1 d^3r \\ &= \Theta_{n'} \Theta_n \Xi_{l'} \Xi_l \int_{-1}^1 d\zeta' \cos(k_{n'}(\zeta + 1)) \cos(k_n(\zeta + 1)) \\ &\quad \times \int_0^1 J_0(\kappa_{l'} \rho) J_0(\kappa_l \rho) \rho d\rho \int_0^1 \rho' d\rho' \int_0^\infty k J_0(k\rho) J_0(k\rho') dk \\ &= \delta_{n,n'} \delta_{l,l'}. \end{aligned}$$

using the identities given before. The matrix elements of $(\hat{n}_{zz}[1])_2$ are

$$\begin{aligned} (n_{zz2}^{\text{stat}})_{m'm} &= \int \Psi_{m'}(\zeta, \rho) \Psi_m(\zeta, \rho) (\hat{n}_{zz}[1])_2 d^3\mathbf{r} \\ &= -\frac{\Theta_n \Xi_l \Theta_{n'} \Xi_{l'}}{2\alpha} \int_0^1 J_0(\kappa_{l'} \rho) J_0(\kappa_l \rho) \rho d\rho \int_0^1 \rho' d\rho' \\ &\quad \times \int_0^\infty \alpha^2 k^2 J_0(k\rho) J_0(k\rho') dk \int_{-1}^1 d\zeta \int_{-1}^1 e^{-\alpha k |\zeta - \zeta'|} d\zeta' \\ &\quad \times \cos(k_{n'}(\zeta + 1)) \cos(k_n(\zeta + 1)). \end{aligned}$$

To simplify the expression we again use the integral given by eqn (C.2). Then

$$J = \frac{1}{\pi} \int_{-\infty}^\infty \frac{k}{k_z^2 + k^2} J_{n,n'}(k) dk_z$$

with

$$\begin{aligned} J_{n,n'}(k) &= \int_{-1}^1 \cos(k_{n'}(\zeta + 1)) \cos(k_n(\zeta + 1)) e^{i\alpha k_z \zeta} d\zeta \int_{-1}^1 e^{-\alpha k_z \zeta'} d\zeta' \\ &= \frac{1}{2} d_0(\alpha k_z) [d_{n+n'}(\alpha k_z) + d_{n-n'}(\alpha k_z)] \end{aligned}$$

Similarly we define

$$\begin{aligned} N_{l,l'}(k) &= \int_0^1 J_0(k\rho) J_0(\kappa_{l'} \rho) J_0(\kappa_l \rho) \rho d\rho \int_0^1 J_0(k\rho') \rho' d\rho' \\ &= \frac{J_1(k)}{k} \int_0^1 J_0(k\rho) J_0(\kappa_{l'} \rho) J_0(\kappa_l \rho) \rho d\rho. \end{aligned}$$

Then

$$(n_{zz2}^{\text{stat}})_{m'm} = -\frac{\Theta_n \Xi_l \Theta_{n'} \Xi_{l'} \alpha}{2\pi} \int_{-\infty}^\infty \frac{k}{k_z^2 + k^2} dk_z \int_0^\infty k^2 J_{n,n'}(k) N_{l,l'}(k) dk$$

and finally

$$(n_{zz}^{\text{stat}})_{m'm} = \delta_{n,n'} \delta_{l,l'} + (n_{zz2}^{\text{stat}})_{m'm}.$$

To summarize, the dipolar matrix is given by

$$\begin{aligned} (\hat{H}_d)_{m',m} &= \omega_M (\hat{h}_d)_{m',m} \\ &= \omega_M \left\{ -\delta_{n,n'} \delta_{l,l'} - (n_{zz2}^{\text{stat}})_{n'l',nl} - \frac{1}{2} (n_{zz2}^{\text{dyn}})_{n'l',nl} \right\} \\ &= \omega_M \left\{ \frac{1}{2} \delta_{n,n'} \delta_{l,l'} - (n_{zz}^{\text{stat}})_{n'l',nl} - \frac{1}{2} (n_{zz}^{\text{dyn}})_{n'l',nl} \right\}. \end{aligned} \quad (\text{C.5})$$

The total matrix which we have to evaluate is

$$\begin{aligned} H_{m',m} &= \omega_M (\hat{h}_d)_{m',m} - i \frac{\omega_D L^2}{(1 + i\mu M_0)} \int \Psi_{m'} \nabla^2 \Psi_m(\mathbf{r}) d^3\mathbf{r} \\ &\quad + \omega_G \int \frac{z}{L} \Psi_{m'}(\mathbf{r}) \Psi_m(\mathbf{r}) d^3\mathbf{r}. \end{aligned}$$

This matrix is diagonalized to find the eigenvalues and eigenfunctions.

THE BIBLIOGRAPHY

- [1] ER Dobbs. *Helium Three*. Oxford Science Publications, 2000. [2](#), [4](#), [5](#), [61](#)
- [2] Roger Bowley and Mariana Sanchez. *Introductory Statistical Mechanics*. Oxford Science Publications, 2nd edition, 1999. [2](#)
- [3] LD Landau. The Theory of a Fermi Liquid. *Sov. Phys. JETP*, **3**, 920–925, (1957). [4](#), [5](#)
- [4] D Pines and P Nozieres. *The Theory of Quantum Liquids: Volume I: Normal Fermi Liquids*. WA Benjamin, 1966. [4](#)
- [5] G Baym and C Pethick. *Landau Fermi-liquid theory - Concepts and Applications*. Wiley, 1991. [4](#), [6](#), [87](#)
- [6] LD Landau. Oscillations in a Fermi Liquid. *Sov. Phys. JETP*, **5**, 101–108, (1957). [5](#)
- [7] LD Landau. On The Theory of the Fermi Liquid. *Sov. Phys. JETP*, **8**, 70–74, (1959). [5](#)
- [8] C Lhuillier and F Laloë. Transport properties in a spin polarised gas, I. *J. de Physique*, **43**, 197–224, (1982). [6](#)
- [9] C Lhuillier and F Laloë. Transport properties in a spin polarised gas, II. *J. de Physique*, **43**, 225–241, (1982). [6](#)

- [10] WR Abel, RT Johnson, JC Wheatley, and W Zimmerman Jr. Thermal Conductivity of Pure ^3He and of Dilute Solutions of ^3He in ^4He at Low Temperatures. *Phys. Rev. Lett.*, **18**, 737–740, (1967). [6](#)
- [11] DC Carless, HE Hall, and JR Hook. Vibrating Wire Measurements in Liquid ^3He , I: The normal state. *J. Low. Temp. Phys.*, **50**, 583–603, (1983). [6](#), [64](#)
- [12] R König and F Pobell. Fermi Liquid behaviour of the viscosity of ^3He - ^4He mixtures. *J. Low. Temp. Phys.*, **97**, 287–310, (1994). [7](#), [64](#), [87](#)
- [13] JCH Zeegers, A Th AM de Waele, and HM Gijsman. Viscosity of Saturated ^3He - ^4He mixtures below 200mK. *J. Low. Temp. Phys.*, **84**, 37–47, (1991). [7](#), [64](#), [87](#)
- [14] DI Bradley and R Oswald. Viscosity of the ^3He - ^4He dilute phase in the mixing chamber of a dilution refrigerator. *J. Low Temp. Phys.*, **80**, 89, (1990). [7](#), [87](#)
- [15] JR Owers-Bradley, PC Main, RJ Church, TMM Hampson, G McHale, and RM Bowley. Viscosity of a Spin-Polarized ^3He - ^4He solution. *Phys. Rev. Lett.*, **61**, 1619–1622, (1988). [6](#)
- [16] WJ Mullin and JW Jeon. Spin Diffusion in Dilute and Polarized ^3He - ^4He Solutions. *J. Low. Temp. Phys.*, **88**, 433–482, (1992). [8](#), [9](#), [62](#), [88](#)
- [17] D Hone. Self-Diffusion in Liquid Helium-3. *Phys. Rev.*, **121**, 669–673, (1961). [8](#)
- [18] AC Anderson, DO Edwards, WR Roach, RE Scrwinski, and JC Wheatley. Thermal and Magnetic properties of dilute solutions of ^3He in ^4He at Low Temperatures. *Phys. Rev. Lett.*, **17**, 367–372, (1966). [8](#)
- [19] AE Meyerovich. Degeneracy effects in the spin dynamics of spin-polarised Fermi gases. *Phys. Lett. A*, **107**, 177, (1985). [9](#), [11](#), [61](#), [62](#)
- [20] AE Meyerovich and KA Musaelian. Anomalous Spin Dynamics and Relaxation in Fermi Liquids. *Phys. Rev. Lett.*, **72**, 1710–1713, (1994). [10](#), [11](#), [61](#), [62](#)
- [21] JW Jeon and WJ Mullin. Transverse Spin-Diffusion in Polarized Fermi Gases. *Phys. Rev. Lett.*, **62**, 2691–2694, (1989). [10](#), [11](#), [20](#), [61](#), [62](#), [88](#)
- [22] DI Golosov and AE Ruckenstein. Low Temperature diffusion in spin polarized Fermi Gas. *Phys. Rev. Lett.*, **74**, 1613–1616, (1995). [11](#)

- [23] AE Meyerovich and KA Musaelian. *J. Low Temp. Phys.*, **89**, 781, (1992). [11](#)
- [24] IA Fomin. Transverse Spin-Dynamics of a Spin-polarised Fermi Liquid. *JETP Lett.*, **65**, 749, (1997). [11](#), [61](#)
- [25] AJ Leggett and MJ Rice. Spin Echoes in Liquid ^3He and Mixtures: A predicted New Effect [and *Erratum*]. *PRL*, **20** [21], 586–589 [506], (1968). [12](#), [21](#), [68](#), [72](#)
- [26] AJ Leggett. Spin Diffusion and Spin Echoes in Liquid He-3 at Low-T. *J. Phys. C*, **3**, 448–459, (1970). [12](#), [13](#), [21](#), [25](#), [27](#), [47](#), [51](#), [63](#), [67](#), [68](#)
- [27] H Ishimoto, H Fukuyama, T Fukuda, T Tazaki, and S Ogawa. Spin Waves in ^3He - ^4He solutions. *Phys. Rev. B*, **38**, 6422–6431, (1988). [12](#), [63](#), [68](#), [88](#)
- [28] JH Ager, A Child, R König, JR Owers-Bradley, and RM Bowley. Longitudinal and Transverse Spin Diffusion in ^3He - ^4He mixtures in a Strong Magnetic Field. *J. Low. Temp. Phys.*, **99**, 683, (1995). [12](#), [22](#), [23](#), [61](#), [63](#), [87](#), [124](#)
- [29] VP Silin. Oscillations of a Fermi-liquid in a Magnetic Field. *Sov. Phys JETP*, **6**, 945–50, (1958). [12](#), [20](#)
- [30] Maurice Goldman. *Quantum Description of High-Resolution NMR in Liquids*. Oxford Science Publications, 1995. [13](#)
- [31] A Abragam. *The Principles of Nuclear Magnetism*. Oxford University Press, 1961 and after. [13](#)
- [32] F Bloch. Nuclear Induction. *Phys. Rev.*, **70**, 460–474, (1946). [16](#)
- [33] HC Torrey. Bloch equation with Diffusion Terms. *Phys. Rev.*, **104**, 563–565, (1956). [16](#), [17](#), [51](#)
- [34] AS Borovik-Romoanov, Yu M Bun'kov, VV Dmitriev, Yu M Mukharskii, and K Flachbart. Experimental study of separation of magnetization of precession in ^3He - B into two magnetic domains. *Sov. Phys. JETP*, **61**, 1199–1206, (1985). [19](#), [76](#)
- [35] VV Dmitriev, IV Kosarev, N Mulders, VV Zavjalov, and D Ye Zmeev. Homogeneous spin precession in superfluid ^3He confined to aerogel. *Physica B*, **329–333**, 324–326, (2003). [19](#), [126](#)
- [36] DD Osheroff and MC Cross. Magnetostatic Modes in Highly Polarised Solid He-3. *Phys. Rev. Lett.*, **59**, 94–97, (1987). [19](#)

- [37] D Candela, N Masuhara, DS Sherrill, and DO Edwards. Collisionless spin-waves in Normal and Superfluid He-3. *J. Low. Temp. Phys.*, **63**, 369, (1986). [19](#), [29](#), [44](#), [62](#), [63](#), [69](#), [80](#), [119](#)
- [38] P-J Nacher, G Tastevin, B Villard, N Piegay, F Marion, and K Sauer. NMR Instabilities in Spin-Polarised Liquids: ^3He , ^3He - ^4He mixtures and ^{129}Xe . *J. Low. Temp. Phys.*, **121**, 743–748, (2000). [19](#)
- [39] D Candela, H Akimoto, RM Bowley, O Buu, D Clubb, and JR Owers-Bradley. Spin Diffusion Anisotropy in Liquid ^3He . *J. Low. Temp. Phys.*, **121**, 767–772, (2000). [19](#), [22](#), [23](#), [24](#), [62](#), [110](#), [113](#), [114](#), [115](#), [117](#), [119](#), [121](#)
- [40] JR Owers-Bradley, O Buu, CJM McGloin, RM Bowley, and R König. Non-linear effects from the dipolar demagnetising field in ^3He at very high magnetic field. *Physica B*, **284–288**, 190–191, (2000). [19](#), [111](#), [119](#)
- [41] JR Owers-Bradley, H Chocolacs, RM Mueller, Ch Buchal, M Kubota, and F Pobell. Spin Waves in Liquid ^3He - ^4He mixtures. *Phys. Rev. Lett.*, **51**, 2120–2123, (1983). [20](#), [63](#)
- [42] A Roni and G Vermeulen. Experimental Evidence against zero-temperature damping in ^3He . *Physica B*, **280**, 87–88, (2000). [20](#), [80](#)
- [43] G Vermeulen and A Roni. Zero Temperature spin wave damping in spin-polarised ^3He : Does it exist? *Phys. Rev. Lett.*, **86**, 248–251, (2001). [20](#), [25](#), [62](#), [63](#), [80](#), [88](#)
- [44] LR Corruccini, DD Osheroff, DM Lee, and RC Richardson. Spin Diffusion in Liquid ^3He : The Effect of Leggett and Rice. *Phys. Rev. Lett.*, **27**, 650–653, (1971). [22](#)
- [45] L-J Wei, N Kalechofsky, and D Candela. Observation of Field-Induced Spin-Current Relaxation in a Fermi liquid. *Phys. Rev. Lett.*, **71**, 879, (1993). [22](#), [61](#)
- [46] H Akimoto, JS Xia, ED Adams, D Candela, WJ Mullin, and NS Sullivan. Spin-Transport in Very Dilute ^3He - ^4He at Very High B/T. *J. Low. Temp. Phys.*, **126**, 109–114, (2002). [22](#), [25](#), [62](#), [63](#)
- [47] H Akimoto, D Candela, JS Xia, WJ Mullin, ED Adams, and NS Sullivan. New Evidence for Zero-Temperature Relaxation in a Spin-Polarized Fermi Liquid. *Phys. Rev. Lett.*, **90**, 105301, (2003). [22](#), [23](#), [62](#), [63](#), [124](#)

- [48] JR Owers-Bradley, RM Bowley, O Buu, D Clubb, and G Vermeulen. Spin-Wave Modes and Spin-Diffusion Anisotropy in a ^3He - ^4He Mixture at High B/T. *J. Low. Temp. Phys.*, **121**, 779–784, (2000). [24](#), [30](#), [62](#), [63](#), [66](#), [67](#)
- [49] AIM Rae. *Quantum Mechanics*. IOP Publishing, 2002. [29](#), [33](#)
- [50] BI Bleaney and B Bleaney. *Electricity and Magnetism*. Oxford University Press, 2002. [30](#)
- [51] VV Dmitriev, VV Moroz, AS Visotskiy, and SR Zakazov. Experiments in coherently precessing spin state in ^3He - ^4He solution. *Physica B*, **210**, 366–372, (1995). [30](#), [45](#), [76](#)
- [52] RJ Ragan. Spin-Rotation effects in Bounded Spin-Diffusion. *J. Low. Temp. Phys.*, **98**, 489, (1995). [30](#)
- [53] O Buu, D Clubb, R Nyman, JR Owers-Bradley, and R König. Transverse Spin Diffusion in ^3He - ^4He mixtures: Part I. *J. Low. Temp. Phys.*, **128**, 123–142, (2002). [30](#), [44](#), [62](#), [63](#), [65](#), [66](#), [70](#), [71](#), [79](#), [80](#), [87](#), [88](#), [114](#), [116](#), [127](#)
- [54] O Buu, R Nyman, D Clubb, RM Bowley, JR Owers-Bradley, and G Eska. Transverse Spin Diffusion in ^3He - ^4He mixtures: Part II. *J. Low. Temp. Phys.*, **128**, 143–162, (2002). [30](#), [62](#), [63](#), [66](#), [69](#), [71](#), [79](#), [81](#), [94](#), [116](#), [127](#)
- [55] M Abramowitz and IA Stegun. *Handbook of Mathematical Functions*. Dover Publications, 1964. [32](#), [58](#), [59](#), [96](#)
- [56] WH Press, BP Flannery, SA Teukolsky, and WT Vetterling. *Numerical Recipes*. Cambridge University Press, 1987. [34](#)
- [57] Mathworks. MATLAB documentation. <http://www.mathworks.com/>. [34](#), [79](#)
- [58] SD Stoller, W Happer, and FJ Dyson. Transverse spin relaxation in inhomogeneous magnetic fields. *Phys. Rev. A*, **44**, 7459–7477, (1991). [37](#), [38](#), [56](#)
- [59] O Buu, R Nyman, RM Bowley, and JR Owers-Bradley. Leggett-Rice effect in a finite geometry. *Phys. Rev. B*, **65**, 134512, (2002). [37](#), [38](#), [54](#), [114](#), [127](#)
- [60] Y-Q Song, BM Goodson, B Sheridan, TM de Swiet, and A Pines. Effects of diffusion on Magnetic Resonance Imaging of Laser-Polarized Xenon Gas. *J. Chem. Phys.*, **108**, 6233–6239, (1998). [41](#), [116](#)

- [61] D Candela, DR McAllaster, and L-J Wei. Transverse spin diffusion and spin-rotation in very dilute and spin-polarized ^3He - ^4He mixtures. *Phys. Rev. B*, **44**, 7510, (1991). [44](#), [59](#), [60](#), [62](#), [63](#), [80](#)
- [62] P Le Doussal and PN Sen. Decay of nuclear magnetization by Diffusion in a Parabolic Magnetic Field: An exactly solvable model. *Phys. Rev. B*, **46**, 3456–3485, (1992). [54](#)
- [63] GD Cates, SR Schaefer, and W Happer. Relaxation of Spins due to field inhomogeneities in gaseous samples at low magnetic fields and pressures. *Phys. Rev. A*, **37**, 2877, (1988). [58](#)
- [64] A Roni. *Ondes de Spin Dans l' ^3He Polarise*. PhD thesis, CRTBT Grenoble, 1999. Available from <http://www-crtbt.polycnrs-gre.fr/he3pol/dilution/spinwaves.html> . [58](#), [59](#)
- [65] KC Hasson, GD Cates, K Lerman, P Bogorad, and W Happer. Spin Relaxation due to magnetic field inhomogeneities: Quartic Dependence and diffusion constant measurements. *Phys. Rev. A*, **41**, 3672, (1990). [59](#)
- [66] D Clubb. *Spin Dynamics of ^3He and ^3He - ^4He Mixtures*. PhD thesis, University of Nottingham, 2003. Available from <http://etheses.nottingham.ac.uk/archive/00000007/> . [64](#), [66](#), [67](#)
- [67] F Pobell. *Matter and Methods at Low Temperature*. Springer, 1996. [64](#), [66](#)
- [68] W Ruesink, JP Harrison, and A Sachrajda. The Vibrating Wire Viscometer as a Magnetic Field-Independent ^3He Thermometer. *J. Low. Temp. Phys.*, **70**, 393–411, (1988). [64](#)
- [69] AS van Steenbergen, SAJ Wiegers, PE Wolf, JAAJ Perenboom, and JC Maan. Nuclear magnetic relaxation in liquid ^3He and ^3He - ^4He mixtures. *Phys. Rev. B*, **58**, 925–935, (1998). [69](#), [115](#)
- [70] RJ Ragan and DM Schwarz. Castaing Instabilities in Longitudinal Spin-Diffusion Experiments. *J. Low. Temp. Phys.*, **109**, 775–799, (1997). [70](#), [76](#)
- [71] RJ Ragan and RW Weber. Castaing Instabilities in Spin-Echo experiments. *J. Low. Temp. Phys.*, **118**, 167–188, (2000). [70](#), [76](#)
- [72] B Castaing. Polarized ^3He . *Physica B*, **126**, 212–216, (1984). [70](#), [76](#)

- [73] R Ragan, K Grunwald, and C Glenz. Temperature Increase of Highly-Polarized Fermi-liquids in Spin-Echo experiments. *J. Low. Temp. Phys.*, **126**, 163–168, (2002). [71](#), [87](#)
- [74] IA Fomin. Separation of magnetization precession into two magnetic domains. Theory. *Sov. Phys. JETP*, **61**, 1207–1213, (1985). [76](#)
- [75] AS Bedford, RM Bowley, JR Owers-Bradley, and D Wightman. Multiple spin-echoes in spin-polarised Fermi liquids. *J. Low. Temp. Phys.*, **85**, 389, (1991). [76](#)
- [76] D Einzel, G Eska, Y Hirayoshi, T Kopp, and P Wolfe. Multiple Spin-Echoes in Normal Fermi-liquid. *Phys. Rev. Lett.*, **53**, 2312–2315, (1984). [76](#)
- [77] G Deville, M Bernier, and JM Delrieux. NMR Multiple Echoes observed in solid ^3He . *Phys. Rev. B*, **19**, 5666–5689, (1979). [76](#)
- [78] K-U Taubenreuther, E Nazaretski, L Hristakos, H Götz, and G Eska. Spin echoes and diffusion in normal-fluid ^3He . *Physica B*, **284–288**, 188–189, (2000). [76](#)
- [79] PL Krotkov, VP Mineev, and GA Vermeulen. Effects of Dipolar Field in spin-dynamics of a Fermi liquid. *Phys. Rev. B*, **65**, 054301, (2002). [89](#), [92](#), [95](#), [104](#), [111](#), [119](#), [125](#)
- [80] LR Walker. Magnetostatic Modes in Ferromagnetic Resonance. *Phys. Rev.*, **105**, 390–399, (1957). [89](#)
- [81] RI Joseph and E Schlomann. Theory of Magnetostatic Modes in a Long and Axially Magnetized Cylinder. *J. App. Phys.*, **32**, 1001–1005, (1961). [89](#), [102](#)
- [82] E Schlomann and RI Joseph. Instability of Spin Waves and Magnetostatic Modes in a Microwave Magnetic Field Applied Parallel to the dc Field. *J. App. Phys.*, **32**, 1006–1014, (1961). [89](#), [102](#)
- [83] P-J Nacher, N Piegay, F Marion, and G Tastevin. NMR Instabilities in Highly Magnetised Liquid Helium Solutions. *J. Low. Temp. Phys.*, **126**, 145–150, (2002). [89](#)
- [84] P-J Nacher, F Marion, B Villard, and G Tastevin. NMR Dynamics with Large Dipolar Interactions in Liquid Helium-3 films. *J. Low. Temp. Phys.*, **126**, 85–90, (2002). [89](#)

-
- [85] J Jeener. Dynamical Effects of the Dipolar Field Inhomogeneities in High-Resolution NMR: Spectral Clustering and Instabilities. *Phys. Rev. Lett.*, **82**, 1772–1775, (1999). [89](#), [97](#)
- [86] RJ Ragan and WJ Mullin. Anisotropic Spin Diffusion and MSEs in ^3He - ^4He solutions. *J. Low. Temp. Phys.*, **102**, 461–475, (1996). [126](#)
- [87] D Candela and N Kalechofsky. Nuclear Magnetism of Normal ^3He and ^3He - ^4He mixtures in aerogel. *J. Low. Temp. Phys.*, **113**, 351, (1998). [126](#)
- [88] VV Dmitriev, IV Kosarev, N Mulders, VV Zavjalov, and D Ye Zmeev. Pulsed NMR experiments in superfluid ^3He confined in aerogel. *Physica B*, **329–333**, 296–298, (2003). [126](#)
- [89] VV Dmitriev, IV Kosarev, N Mulders, VV Zavjalov, and D Ye Zmeev. Measurements of longitudinal and transverse magnetic relaxation in superfluid ^3He confined to aerogel. *Physica B*, **329–333**, 322–323, (2003). [126](#)
- [90] R Nyman, O Buu, D Clubb, J Owers-Bradley, and R Bowley. A Realistic Model of Spin-Transport in dilute ^3He in ^4He in a Finite Geometry. *Physica B*, **329–333**, 183–184, (2003). [127](#), [132](#)
- [91] JD Jackson. *Classical Electrodynamics*. Wiley, 3rd edition, 1999. [134](#)
- [92] IS Gradshteyn and IM Rhysik. *Table of integrals, series, and products*. Academic Press. [136](#), [137](#)